APPLICATIONS AND METHODS OF INCORPORATING ACOUSTIC PARTICLES TO ENHANCE FOCUSED ULTRASOUND THRAPY OUTCOMES

By

Aparna Singh

Dissertation
Submitted to the Faculty of the
Graduate School of Vanderbilt University in
partial fulfillment of the requirements
for the degree of

DOCTOR OF PHILOSOPHY

In

Biomedical Engineering

May 31, 2022

Nashville, Tennessee

Approved:

Charles F Caskey, Ph.D.

Li Min Chen, Ph.D.

Brett C Byram, Ph.D.

Sandeep Arora , MBBS.

William A Grissom, Ph.D.

This thesis is dedicated to the most loving parents and sister, who have constantly instilled in me the importance and value of a good education.

ACKNOWLEDGMENTS

There are many people, personally and professionally, who I would like to thank for directly and indirectly contributing towards my thesis. I would like to start by thanking my supervisor Dr. Charles Caskey at Vanderbilt University for supporting me and guiding me throughout my PhD career. His expertise and knowledge helped me navigate graduate school with the least amount of resistance. Throughout these five years, I have had a lot of fun working with him. As a mentor, he has given me the independence to explore projects of my interest but has also helped every time I have failed. It was in these scenarios that I realized what my strengths are as a scientist, and for that I will be always thankful to Dr. Caskey. I would also like to thank Dr. Caskey for challenging me and pushing me because those situations have made me a better scientist. Also, this thesis would not have been possible without the input from my committee members Dr. Byram, Dr. Arora, Dr. Grissom and Dr. Chen. Your input and suggestions have been valuable. I was very lucky to collaborate with few of my committee members and it has been a very learning experience.

I would like to thank Caskey lab members: Michelle, Tom, Tony, Jiro, Adrienne, Malachy, and Andy. I have had an opportunity to work with most of the lab members at some point in my graduate school and their support and help throughout my PhD has shaped me to be a better scientist. Personally, I would like to thank Michelle for being there for me and listening to me during our coffee chat hours. I would also like to thank Jiro whose expertise in microbubble imaging and injections have made my thesis possible. Finally, Tom and Tony have been a great technical help throughout my graduate school, and I will always be very thankful to them for that. I would like to extend thanks to the Grissom lab members Charlotte and Huiwen for numerous coffee happy hours and Thai food nights. They have been the highlight of my graduate school.

Personally, I would like to start by thanking my mom and dad. Their unwavering support, love, and confidence in me since my childhood has helped me power through my toughest days. To my grandparents, thanks for showering me our family with unconditional love. Grandpa, you have set an excellent example of how to be successful in your life after storming through a rough childhood. Your kids and grandkids are extremely lucky to call you family and can only hope to be as inspiring and successful as you. I was also extremely lucky to have met and remember my conversations with my great-grandparents. To my great-grandparents, thanks for always caring for our family and thanks for always showing how to live selflessly and righteously.

To my sister and my brother-in-law, thanks for being my parents away from home and thanks for taking care of me as I navigated my life in the United States. Your support and love mean everything to me. To my niece, you have been the joy of my life since the day you were born and seeing you every day, even virtually, just melts all the stress away. To my husband, Prateek, you have been my biggest strength throughout these 5 years. Thanks for being there for me for every step of the way, even when it meant being there in a long-distance relationship and marriage.

TABLE OF CONTENTS

Page

LIST OF TABLES

LIST OF FIGURES

CHAPTER 1: Introduction

1.1 Synopsis

The overarching goal of this thesis is to develop focused ultrasound (FUS) therapy and imaging methods to enhance the application, guidance, and monitoring of FUS therapies that use acoustically active particles. FUS is a noninvasive method to focus energy into the body that is being explored for a variety of healthcare applications that are either FDA-approved or undergoing clinical trials. Thermal ablation with FUS is being used to treat bone metastasis [1], essential tremor [2], Parkinson's disease [3], and prostate cancer [4]. Outside of these FDA approved applications, FUS is extensively used to deliver drugs after opening blood-brain barrier (BBB), both in humans and in animal model in research setting [5]–[7]. Literature also notes clinical trials that use FUS for treatment of breast cancer [8]–[10]. A challenge common to all applications of FUS is the process of guiding and monitoring therapy while avoiding off-target effects. This thesis develops ultrasound-based approaches to improve this process.

One of the main challenges with focused ultrasound therapy is focusing energy into the body while avoiding off-target effects, such as unintended tissue heating [10]. Such off-target heating has been reported in literature for FUS ablation clinical trials where in clinical trials of breast cancer treatment, off-target effects such as skin burns were reported [11], [12], due to long treatment duration (>30 mins) at over 1000W/cm^2. In clinical trial of thalamotomies [13], new skull lesions appeared three months after FUS treatment due to off-target heat deposition. Such off-target heating is undesirable and can add to patients' recovery time. By combining pressure sensitive acoustically active particles, such as phase shift nanodroplets (PSNDs) with FUS, we can reduce off-target heating by increasing acoustic absorption only at the focus and sparing tissues in that are in the FUS beam path but not at the FUS focus [14], [15]. In this thesis, I combine PSNDs with multiple focus ablation patterns to increase ablation efficiency and ablation volume while maintaining only a 3.5°C temperature rise at surface. At the same pressure and energy, the surface heating was comparable, and no ablation was seen in scenarios where PSNDs were not employed.

Another fundamental challenge of focused ultrasound treatment is that of targeting and monitoring, which is typically performed under MRI guidance. MRI is the gold standard for image guidance with FUS due to its ability to provide anatomical guidance and direct monitoring of temperature in real-time. Because MRI can be costly and limit accessibility, methods to target and monitor FUS treatments outside of the MR environment are desirable [16], [17]. By incorporating ultrasound imaging (or more generally the reception of ultrasound signals), we can create image guidance and monitoring methods that complement and enhance FUS therapies. In this thesis, I developed methods where I registered ultrasound imaging transducer and focused ultrasound transducer to open blood-brain

barrier (BBB). To open BBB, I use the same acoustically active particles, microbubbles (MBs), to transcranially image rat brain vasculature and open BBB wherein the transcranial image of rat brain vasculature was used to guide FUS therapy. I also used the same imaging transducer to passively record acoustic activity during FUS procedures to monitor any tissue related damages.

The methods discussed in this thesis are overall aimed to enhance focused ultrasound therapy outcomes at the focus, while reducing off-target tissue heating. Methods discussed in this thesis combine acoustically active particles to bridge the gap between focused ultrasound and imaging ultrasound such that ultrasound imaging can be used for targeting focused ultrasound and can be used for delineating effects of change in blood flow due to external stimulations. The objectives of the methods discussed in this thesis are covered in later chapters and are as follows:

Chapter 2: In chapter 2, I go into details about methods that have been developed to enhance ablation and make ultrasound guided focused ultrasound experiment in *in-vivo* possible. I talk about methods that helped in registering focused ultrasound transducer with imaging transducer and methods that were used to monitor acoustic emissions generated during FUS treatment.

Chapter 3: Improving the Heating Efficiency of High Intensity Focused Ultrasound Ablation Through the Use of Phase Change Nanodroplets and Multi-focus Sonication. We developed methods to incorporate phase shift nanodroplets (PSNDs), which are acoustically active particles, that only enhance heating only in the focal regions all the while sparing pre-focal regions. We also combined PSNDs with multiple foci FUS ablation patterns that increased ablation volume at the focus but did not result in ablation pre-focally.

Chapter 4: Using Passively Detected Acoustic Signals to Characterize Ultrasound Gated Nanoparticles. We developed methods where we characterized the responses of acoustically active nanoparticles using passive detection of receive signals on imaging ultrasound elements. We used ultrasound gated nanoparticles that release drugs upon FUS sonication. Additionally, we used ultrasound imaging transducer to record cavitation activity to monitor FUS procedures. Hence, we developed an all-ultrasound system that could sonicate ultrasound gated particles and record emissions which could indicative of any harmful FUS activity.

Chapter 5: Combining power Doppler ultrasound imaging and fast frame rate passive acoustic mapping algorithm.

We used microbubbles (MBs), an acoustically active particle, for both ultrasound imaging and FUS to image and open BBB using ultrasound guidance. Methods developed in this chapter could map and monitor cavitation activity during steered FUS sonication of MBs flowing in a cellulose tube in presence and absence of skull. Additionally, we could target brain regions within 1.1mm accuracy using ultrasound imaging to open blood brain barrier by pairing MBs with FUS in rats. Overall, developments in this chapter allowed us to use ultrasound images, rather than MRI images, to safely open blood brain barrier. Passive acoustic map and cavitation monitoring was used to inform us of any vasculature damage in brain.

Treatments	Invasive ☹/ Non-invasive ☺	Off-target effects: Minimal ☺ Substantial ☹
Surgery	☹	☺
Chemotherapy	😐	☹
Hormonal therapy	☺	☹
Radiation therapy	😐	☹
Biological therapy	☺	☹

Figure 1.1: Different modalities that are currently used for treatment of cancer are either invasive or have substantial off target effects.

Chapter 6: Use power Doppler ultrasound imaging to map blood flow activity in the rodent brain at varied stimulatory frequencies. We combined MBs with ultrasound imaging to develop methods that could measure changes in blood flow in response to external stimulation. Methods developed in this chapter could potentially be combined with FUS neuromodulation procedures to develop an all-ultrasound method to perform and study the effects of neuromodulation.

1.2 Significance

Current treatment of soft tissue diseases such as breast cancer or liver cancer often involve invasive procedures such as surgery or ionizing procedures such as radiotherapy (Fig 1.1). In a recent review [18], authors evaluated the risk of surgical site infection after breast cancer surgery. The researchers found that about 13.07% of patients had surgical site infection after breast cancer surgery. A second study evaluated the risks of radiation and found that radiation dosage can impact the heart and cause secondary malignancies in lungs [19]. Recent advancements in FUS

treatments have made it an attractive option as it is completely non-invasive and non-ionizing and can target deep tissues precisely, like the red focal spot in Fig 1.2 [20]. FUS can be applied to either cause destruction of tissues and vessels via thermal deposition of energy (e.g. tissue necrosis or thermal ablation) or can be used non-destructively to modulate neurons and deliver drugs [11], [21]–[23]. When focused ultrasound is used for eliciting destructive effects in tissues, it is often termed as high intensity focused ultrasound (HIFU). HIFU has been FDA approved for treatment of uterine fibroids [24] and pain management for bone metastasis [25] and has been used in clinical trials for treating liver cancer [8], [26], [27], and breast cancer [9].

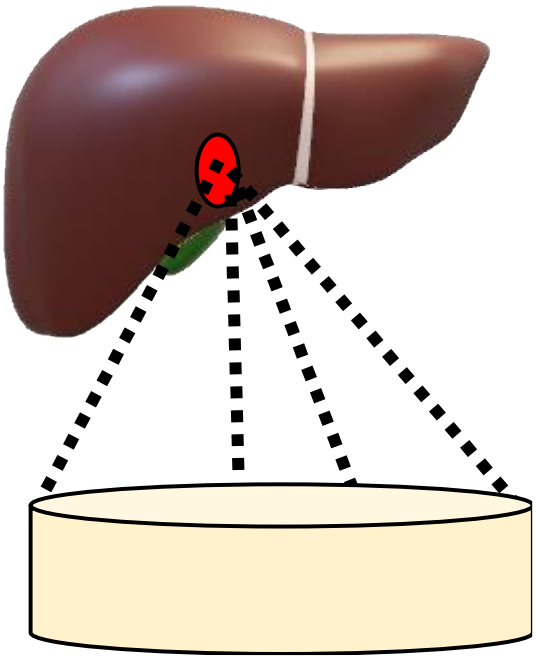

Figure 1.2. Non-invasive targeting via FUS. Focused ultrasound can non-invasively target soft tissues such as liver and can cause ablation by converging non-ionizing ultrasound waves at the desired regions.

FUS has also been implemented to ablate brain tissues to provide symptom relief in essential tremor patients [28]. The standard treatment options for treating essential tremor are radiofrequency lesioning, deep brain stimulation, and gamma knife surgery [29]. In radiofrequency lesioning, a probe is inserted into the brain to burn neurons in the desired area which makes this procedure very invasive. Similarly, deep brain stimulation entails inserting one or more electrodes in the brain making it a highly invasive procedure. Gamma knife radiation involves using ionizing radiation transcranially to generate a permanent lesion in the brain. Analogous to soft tissue ablation treatments, brain ablation treatments are marred with ionizing and invasive procedures and FUS can be implemented to avoid these invasive procedures.

An important aspect of successful FUS treatment is avoiding pre-focal tissue damage, which usually occurs during HIFU therapies where tissue in the beam path may experience secondary degree burns [11] or can induce skull heating [30], [31]. Another key to successful FUS treatment is accurate targeting, which is provided usually by MRI. Collectively, off-target heating, and MRI targeting fundamentally limits a wide-scale adoption of FUS. Hence, improvements in methods to reduce heating of the tissue in beam path while making FUS more portable are

Study	Size	Complication	Time(min)	HIFU params
Gianfelice (2003)	0.1-8.8cm^3	Skin burn (2)	35-133	80-271 W
Khiat(2006)	0.1-11.2cm^3	-	-	-
Furusawa(2006)	0.5-2.5cm^3	Skin burn(1)	76-131	-
Wu(2006)	3.1cm	Skin burn (4)	45-150	5000 – 15000 W/cm^2
Merckel(2016)	2 cm	Pain of score 4-5 (2)	12-75	50-100W

Table 1.1: Clinical trials of breast cancer. Various clinical trials have used HIFU for ablating breast cancer but using high powers for over 2 hours have resulted in pre-focal complications such as skin burns and pain.

needed. The objective of this work is to overcome these limitations and perform successful FUS treatments without causing any unintended heating at an off-target location by using an all-ultrasound guided system that can target and monitor FUS treatments.

1.2.1 FDA-approved FUS applications

Currently in the United States, FUS is FDA approved for uterine fibroid treatment and essential tremor treatment. Uterine fibroid is one of the most common benign tumors in women of childbearing age. The first clinical trial of MRI guided FUS (MRgFUS) treatment of uterine fibroid treatment ablated a small volume of fibroid and used MR thermometry to evaluate the temperature rise which was followed by surgery and then histological evaluation of the damaged tissue [32]. The study showed a good correlation between thermally coagulated tissue volume and the non-enhanced tissue volume in post-treatment contrast enhanced scan. In studies conducted after this initial study[33], treatment were completed without removing the fibroid and showed that the treatment can be performed on an out-patient basis. Patients observed symptomatic relief and results were significantly better in fibroids that received larger coagulated tissue volume[33]. Eventually, HIFU treatment of uterine fibroid was FDA approved in 2004. Following the approval, a retrospective study [34]comparing uterine-sparing surgery and ultrasound-guided high intensity focused ultrasound (USgFUS) ablation of fibroids in 245 women from 2007 to 2015 found that 95.9% of patients undergoing USgFUS saw symptomatic relief compared to 89.1% of patients undergoing uterine-sparing surgery. USgFUS group saw statistically significant symptom relief and lower

recurrence rate ($p<0.05$) than uterine-sparing surgery, confirming long-term clinical outcomes of USgFUS may be better than surgery.

Focused ultrasound also received an FDA approval in 2016 for treatment of essential tremor, a disorder of thalamus resulting in an involuntary and rhythmic shaking. FUS allows accurate and spatially controlled energy deposition in the ventral intermediate nucleus of the thalamus for ET treatment. The first line of treatment for ET is pharmacotherapy but approximately 50% of people with ET experience recurrent tremor and cannot control tremor with medication, or have medication induced side-effect [35]. Patients with recurrent or uncontrollable tremor decide to undergo invasive procedures such as deep brain stimulation [36] or ionizing Gamma Knife (GK) radiosurgery [37]. The adverse effects induced by DBS during implantation [38] or by radiation due to GK can be mitigated by combining technical advantages of MRI and FUS where MRI can non-invasively guide non-ionizing. FUS treatment and give real-time feedback. Studies have shown that MR guided FUS thalamotomy was effective for ET treatment [28], [39], [40], especially when medications failed to work [41]. Patients saw an improvement in mean hand-tremor score by 55% at 6 months and the improved was durable at 1 year (53%) and at 2 years (56%) [39]. In one recent study [41], authors evaluated improvement in tremor in clinical outcomes of MRgFUS thalamotomies at 1 year post-treatment. Researchers found that up to 73.6% of patients had minimal or no disability due to tremor after MRgFUS thalamotomy and improvement sustained throughout the 12-month follow-up.

1.2.2 Next generation uses of FUS: moving beyond ablation

In research, the implementation of FUS spans beyond ablation and can be combined with different acoustically sensitive and thermal sensitive particles to deliver drugs to tumor regions in soft tissues and to open BBB. The sections below discuss some capabilities of FUS in combination with MBs and nanoparticles for treatment of cancer and brain malignancies.

1.2.2.1 Ultrasound-targeted microbubble destruction (UTMD) for cancer therapies

Aside from soft tissue ablation and thalamotomy, FUS can contribute towards treating malignancies of brain and soft tissues without requiring ablation by combining FUS with MBs wherein it destroys MBs for the purposes of targeted drug delivery. The advantage of this method is that it can cause delivery of drugs encapsulated in MBs and thereby release locally upon FUS application. By releasing the drugs locally, it improves the safety margin of drugs with many side effects. In literature, there are several examples of UTMD. For instance, ultrasound

targeted delivery of miR-133a-MBs was able to cause tumor regression in breast cancer treatment *in-vivo* [42]. In other pre-clinical settings, UTMD has been investigated for liver tumors in an orthotopic animal model by locally releasing the drug after ultrasound application. A study by Kang et al. [43] loaded MBs with docetaxel (Dox-MBs) and showed that UTMD with Dox-MBs inhibited growth of liver tumors. Additionally, it decreased proliferation and promoted apoptosis. When compared with the untreated control group, the mean survival time in group that was administered Dox-MBs+ultrasound increased from 23.6 to 36.8 days. In another study [44] that used Dox-MBs in rat liver cancer model, researchers compared plasma Dox concentration, drug levels in myocardium and tumor, and tumor growth in groups that were administered Dox-MBs+ultrasound vs group that was administered free Dox. The group that was administered Dox-MBs+ultrasound showed low drug levels in myocardium, high drug levels in tumor and inhibited tumor growth compared to group that was delivered just free Dox, supporting local delivery of drugs. In a third study, researchers showed that Doxorubicin can be delivered to a treatment site after sonication of Doxorubicin-liposome containing MBs in an *in-vitro* setting [45]. Seeing the effects of unfocused ultrasound on tumor regression, FUS community was quick to evaluate effects of UTMD+FUS in animal models where in one study, researchers compared tumor growth inhibition rates in a mice glioma model. Mice were either treated with radiotherapy (RT), UTMD elicited by FUS sonication after MBs injection or no treatment at all. UTMD and RT groups saw significant reduction tumor growth rates when compared with control [46] . In a separate study [47], researchers designed liposomal nanoparticles, called membrane fusogenic liposomes (MFLs) which are biocompatible with enhanced permeability and retention effect (EPR) effect that can be tailored to fit desired characteristics. With such liposomes, drug dosage can be tailored to prevent any major side effects. In their study, researchers used combination of FUS with MFLs containing Dox and evaluated its efficacy in treating cancer in a xenograft mouse model. The researchers compared the effects of MFLs in treatment groups where mice were treated with no FUS, FUS+MBs, and Dox-MFLs+MBs+FUS. The group that was treated with Dox-MFLs+MBs+FUS had significant inhibition of tumor growth and delivered Dox to the tumor site efficiently without any side effects. Thus, their research show that MFLs can fuse within the cell membrane and can deliver Dox intracellularly.

1.2.2.2 Ultrasound sensitive nanoparticles for cancer treatment

While UTMD is an attractive therapy option, it is fundamentally limiting due to short circulations times in the blood which affects accumulation and retention of MBs in the tumor. Tumor microenvironment usually secretes vascular endothelial growth factor and the cells encompassing the tumor microenvironment have wider and

abnormal intercellular junctions than normal vessels. Such abnormal organization and structures within the tumor vasculature give rise to tortuous and leaky vessels as opposed to heterogeneous vessels in normal tissues. Having leaky vasculature and heterogeneous vessels fundamentally limits retention of microbubbles due to short circulation time. In response to these limitations, researchers have developed nanoparticles that can release drugs after being sonicated at threshold pressure which can circulate for hours. One such example is a stimuli-responsive particles that are nanometer in size and have longer circulation time for enhanced extravasation and retention in the leaky vasculature of the tumor thereby improving the EPR effect. In the last decade, such drug-loaded nano-scaled microbubble precursors have been fabricated and shown to effectively accumulate in tumor and can convert into MBs *in situ* after FUS sonication and MBs under FUS behave non-linearly thereby enhancing FUS therapy outcomes [48]. In one such study [49] where paclitaxel encapsulated in nanodroplets was injected and sonicated via FUS in mice bearing ovarian carcinoma tumors, the sonicated tumor saw effective regression and in one mouse the tumor resolved after four treatments. Similar sensitization to the tumor was seen in a pancreatic tumor model in mice. These studies paved path for additional nanoparticles and liposomes that could be sensitive to ultrasound.

Another example of liposome is thermally sensitive liposomes which are nanometer in size and release drugs upon FUS application. In one study [50], researchers developed one such temperature-sensitive liposomes with enhanced stability in circulation. The liposome consisted of Dox and only released Dox when FUS was applied to the liposome during a hyperthermia treatment. The efficacy of this liposome was tested in a synegeneic murine breast cancer model wherein the tumor was sonicated 5 min prior to administration of this liposome and 20 mins post administration. A single dose of these liposomes in conjunction with FUS suppressed tumor growth. Furthermore, when researchers treated mice twice per week over a 28 day period, they could no longer detect tumor cells and tumor intersititium. Tumor could not be detected 8 months post treatment. Systemic toxicity markers such as cardiac hypertrophy, weight loss, hair loss, and leukopenia were not present post 28 day. In later work [51], researchers from a different institution were able to harness the advantages of two photon microscopy (2PM) to image the release of DOX from such thermosensitive liposomes (LTSL-DOX). Researchers were successful in combining 2PM with FUS and hyperthermia to image the release of LTSL-DOX in real time by using 30s FUS+hyperthermia bursts to 42^{o}C. Being able to visualize drug release in real-time will help in translating the efficacy of these liposomes clinically.

1.2.2.3 Ultrasound sensitive particles for brain application

Many malignancies of the brain remain challenging to treat due to the blood brain barrier (BBB). BBB presents as a hindrance because it prevents therapeutic molecules from entering the brain and delays treatment of diseases such brain tumor [7], Parkinson's disease [52] and Alzheimer's [53]. FUS, in clinical trials, has been used to open blood brain barrier [5] to deliver chemotherapeutics [6] and has been used for treating essential tremor in patients with Parkinson's disease [54]. Acoustically active particles have also benefited the neuromodulation community. Acoustically active particles, such as microbubbles (MBs), in combination with FUS can stimulate desired regions in brain more effectively and require less pressures to open BBB to allow drugs in, which would have otherwise been impenetrable [23], [55]. FUS mediated BBB opening in conjunctions with MBs has enabled researchers to deliver neurturin for treatment of Parkinson's disease in an *in-vivo* setting [56], study neuromodulatory effects *in-vivo* after delivering GABA after BBB opening [23], and study BOLD effects in rats following BBB opening [57]. BBB opening has been especially monumental for treating glioblastoma and in last decade has seen an immense rise in chemotherapeutic drug delivery to glioblastoma after BBB opening. For instance, in one study, a 400 kHz focused ultrasound transducer was used to disrupt BBB in glioma cells implanted Sprague-Dawley rats. After BBB opening, researchers delivered chemotherapeutic agent, used to treat brain tumors, to glioblastomas. After analyzing tumor progression via MRI, researchers found that BBB significantly enhanced the uptake of BCNU, the chemotherapeutic agent, by the tumor without any hemorrhaging. Chemotherapeutic administration after BBB opening improved animal survival rates among the animals that underwent the treatment vs the control [58]. In another very recent study [59], researchers investigated the effects of BBB opening and etoposide administration after BBB opening in a murine glioma model in mice. After confirming safe and successful BBB opening with FUS, the researchers injected etoposide and found that combined treatment of FUS+BBB opening + etoposide decreased tumor size by 45%. Furthermore, it prolonged median overall survival rate by 6% in groups that underwent the treatment. In June of 2021, first patient was treated for glioblastoma with FUS.

Another class of acoustically active particles, called ultrasound gated nanoparticles (NPs), have recently gained prominence. The fabrication of nanoparticles is done such that it can cross blood brain barrier without needing to open blood brain barrier. This is suitable for FUS applications of neuromodulation such as stimulation or inhibition of certain parts of the brain whose function maybe compromised due to BBB opening [23]. These nanoparticles are loaded with drugs such as propofol and pentobarbital and only release these drugs when sonicated at a threshold pressure. In one study, researchers sonicated these nanoparticles in an *in-vivo* setting and released

pentobarbital to deliver local anesthesia [60]. In another study, sonication of these nanoparticles released propofol which was effective in silencing seizures in rats and delivered anesthesia upon FUS sonication of nanoparticles [22], [60]. After delivering propofol, researchers confirmed no BBB opening and performed T2* imaging to show no vascular damage induced due to FUS.

1.3 Overarching challenges for FUS therapy

1.3.1 Challenges with FUS ablation

When focused ultrasound propagates through the tissue, there is a loss of energy in the beam due to attenuation caused by scattering and absorption of sound in the tissue. The absorption of ultrasound energy into the tissue can cause local tissue temperature rise but requires over 1000 W/cm^2 of energy to selectively destruct normal kidney and tumors [61], [62]. Many studies showed the feasibility of coagulating majority of the tumor tissue [10], [63]–[65]. In one study [66], researchers showed that they could coagulate 97±4% of microscopic tumors with minimal side effects. However, only 54% of the patients were able to achieve complete necrosis. In a randomized trial of HIFU for patients with breast cancer, scientists showed that breast cancer cells underwent coagulative necrosis [11]. However, it came at a cost of skin toxicity in the form of skin burns (17%), local pain or discomfort (67%) , and tenderness (17%). Hence, in order to achieve ablation, longer treatment times are needed which can carry risk of greater adverse effects (table 1.1) [67].

To overcome the issue of long treatment time, microbubbles can be used. Microbubbles are micron sized spherical cavities that are filled with gas with phospholipids as a coating layer to stabilize the microbubbles for medical purposes [68]. Microbubbles enhance acoustic absorption and as a result need lower powers to elicit the same ablation effects. In one study [67], *ex-vivo* tissues were treated with and without microbubbles at varying HIFU focal intensities. Researchers observed that at HIFU intensity of 2316 W/cm^2, the lesion volume saw a twofold increase in presence of microbubbles when compared to in absence of microbubbles. The peak temperature reached during microbubble assisted HIFU was 16^{o}C. In another study, when goat livers were ablated with HIFU in presence and absence of microbubbles, the ablated volume measured at the end of HIFU pulses more than doubled in presence of microbubbles than in absence (33.5±12.4 mm^3/s vs 14.5±4.2 mm^3/s) [69]. In a similar study, when rabbit livers were sonicated with HIFU for 60s at ISPTA of 400W/cm^2 with either Levovist microbubbles or saline, researchers observed larger HIFU induced lesion in animals given Levovist than saline (371±104 mm^3 vs 166±71 mm^3). Moreover, the temperature rise 60s after the exposure was greater in presence of microbubbles than in saline

(20.3±3.5°C vs 13.2±3.8°C). Hence, these literature studies show that microbubbles can be used to enhance HIFU ablation outcomes. However, high concentrations of MBs can attenuate acoustic penetration into deeper tissues. Finally, they are too large to extravasate into vascular space and remain localized within the blood vessels [70], [71] and have a short circulation half-life [72].

For ablative procedures in brain such as thalamotomies, presence of the skull is an opportunity of excessive heat deposition as both reflection and attenuation coefficients of the skull surface are high. In response to these limitations, researchers designed a large hemispherical array for a human head which surrounded the top of the head and distributed energy over a large area of the skull surface [31]. To test the efficacy of their transducer in producing lesions, they first inserted a gel layer simulating the skin underneath the skull and in second iteration of the experiment, they used thigh muscle from a sacrificed New Zealand white rabbit. The study confirmed that this hemispherical array could focus through the human skull by creating three lesions through the skull in rabbit tissue. The rabbit skull tissue was heated for 8s, 10s, and 12s. The lesions created were found to be reproducible but the changes in skull surface temperature ranged from 12.4°C to 18.6°C. Adding human body temperature to changes in temperature, one can quickly reach temperatures that can cause thermal damage [73]. The researchers suggested that active cooling method can mitigate such rises in temperature at the skull. Taking these suggestions [74], researchers at another institution set to perform transcranial MRgFUS using ExAblate FUS system in *ex-vivo* human skulls filled with tissue mimicking phantom material. They heated the phantom for 120s during sonication and used active cooling at the scalp while performing FUS treatment. In their setup researchers used a hemispheric array operating at 220kHz and performed multiple sonications while collecting MR thermometry data. The highest peak temperature of 10.2±1°C was reached when researchers sonicated at 4 locations. This was a significant improvement from prior studies where the temperatures elevated to up to 18.6°C in only 12s. In another pre-clinical study in primates [75], the researchers underscored the importance of cooling the skin by having degassed water circulate between array and the surface of the skin. After cooling the skin to approximately 12°C, the skull surface temperature was reduced to 16-18 °C and led to a maximum increase of 12°C during sonication. Thus, the skull temperature rose to only 25°C. However, researchers still observed some overheating at the brain surface and postmortem evaluation revealed several spots of thermally coagulated tissues outer brain surface which were not the target tissues.

After ExAblate received FDA approval for treating essential tremor, they implemented active cooling techniques and performed successful treatments in patients [29], [75], [76]. In one human study [13], however, researchers found that in 7/30 patients, multiple new skull lesions were present 3 months post treatment. These patients with

skull lesions were treated with 25.8kJ of energy whereas patients with no skull lesions were treated with 15.5 kJ. Such off-target skull heating, due to high energy deposition required to cause ablation, still presents challenges and can add to patients' recovery time.

1.3.2 Image guidance challenges with HIFU ablation

Accurate targeting of desired regions is one of the most important aspects for successful FUS delivery. Until the early 1990s, visualization and targeting of the FUS target tissue and FUS induced lesions happened only via ultrasound guidance [77]. By the late 1990s, however, MR guidance of FUS treatment was demonstrated by some groups [78]. Because MRI provides excellent tissue contrast, this makes it a preferred option for tumor detection [79] . It also offers two other benefits: temperature monitoring and tissue coagulation detection. In a retrospective study, researchers found that the first study to show the advantages of MRI-guided FUS happened in University of Arizona where an MRI compatible focused ultrasound was manufactured in-house [80] . These studies progressed to animal experiments and were first reported at the International Conference in Hyperthermic Oncology in 1992 and later was published in a paper [81] in 1993. Soon after this paper, many animal experiments were under way and a first commercial MRIgFUS, Exablate 2000, was FDA approved for uterine fibroid treatment and first treatment was performed in 2001 [76]. For breast cancer ablation applications. MRIgFUS was first used for the treatment of breast fibroadenoma [82]. It was shown in this study that benign tumors can be treated safely and effectively, and the effects of the treatment can be visualized using MRIgFUS [82], thereby expanding the application of MRIgFUS for breast cancer treatment. With addition of MRI guidance, precise focusing of focused ultrasound could be achieved non-invasively. Soon after a clinical prototype array guided by MRI was developed by InSightec and its feasibility was tested in in-vivo rabbit brain through *ex-vivo* human skulls [83]. Additional non-human primate experiments were conducted to test skull heating and other features of this MRgFUS system [75]. Furthermore, this system was tested in three brain tumor patients that saw sharp focusing with an acceptable brain surface temperature [84] . Commercial systems continue to use MRI for targeting for essential tremor applications and are being used to target and open BBB using FUS in animals[23], [85]–[87] and in humans in fig 1.4 [5] to treat amyotrophic lateral sclerosis and Alzheimer's Disease non-invasively [53]. Thus, MRI's capability of providing excellent tissue contrast and temperature monitoring continue to make it a preferred option for guiding and visualizing FUS targets. In next section below, some common methods that visualize FUS focus and monitor FUS treatment using MRI will be covered in detail.

1.3.2.1 MR thermometry

FUS thermal therapies can either be low-temperature hyperthermia where temperatures in the range from 43ºC-45ºC are applied for tens of minutes to kill cancer cells or it can be high temperature thermal ablation in the range of 50ºC-80ºC which can result in tissue necrosis. MRI can provide real time temperature mapping in order to give users more control over the treatment outcome. The regions with the highest temperature change comprises of the FUS focus. These temperature maps can, then, be used to quantify tissue damage based on the Arrhenius-damage integral which quantifies damage using temperature and time and reports it as an equivalent heating time at 43ºC. In order to create an accurate temperature map, users must be aware of MR parameters that are sensitive to temperature such as the proton resonance frequency (PRF), the diffusion coefficient (D), T_1 and T_2 relaxation times, magnetization transfer, and proton density. Discussing dependencies of all MR parameters is out of scope of this thesis but describing PRF method of creating temperature map is prudent considering it is part of chapter 3 of thesis. Hindman in 1966 observed that the PRF was sensitive to temperatures [88]. The local magnetic field B_{loc} determines the resonance frequency of a nucleus in a molecule. The magnetic field (B_0) at the nucleus can be written as

$$B_{loc} = B_0 - B_{0S} = (1 - s)B_0 \dots (1.1)$$

where s is the shielding or screening constant and is dependent on the chemical environment. Due to the presence of nuclear shielding, the resonance frequency becomes

$$\omega = \gamma B_0(1 - s) \dots (1.2)$$

In above equation, γ is the gyromagnetic ration. As the temperature increases, hydrogen bond in water stretch, bend, and break [88]. This results in more electron screening and thus a lower local magnetic field B_{loc} as inferred from equation 1.1 and lower PRF. The average electron screening constant is temperature dependent such that

$$s_T(T) = \alpha T \dots (1.3)$$

where the relationship between electron screening constant and temperature varies linearly by α, which is the PRF change coefficient. This value of -1.03±0.002 x 10^{-8}/ ºC covers temperatures ranging from -15^{0}C to 100^{0}C [88]. The change in resonance frequency can be used to create temperature maps by employing gradient-recalled echo imaging sequence [89]. The change in resonance frequency leads, which is temperature dependent, changes the phase of the image and by measuring the phase difference between a baseline image and hyperthermia image, a change in temperature can be calculated using equation 1.4 as follows:

$$\Delta T = \frac{\varphi(T) - \varphi(T_0)}{\gamma \alpha B_o TE} \ldots (1.4)$$

In equation 4, $\varphi(T)$ is phase of current image (or image after FUS turned on), $\varphi(T_0)$ is the phase of baseline image (or image before FUS turned on), and TE is the echo time. TE can be improved such that phase contrast-to-noise ratio is increased resulting in greater temperature accuracy [90].

1.3.2.2 MR acoustic radiation force imaging (MR ARFI)

MR ARFI can localize FUS focus by measuring the displacement that occurs in tissue in response to FUS. Analogous to soft tissue applications such as cancer, localizing the focus for FUS brain applications such as neuromodulation is also of utmost importance. In the past, MR thermometry has been used to localize the focus for ablative procedures but these procedures were marred with off-target heating in the near and far field of the transducer [13], [91]. Thus, using temperature rises to localize FUS beam in the brain may not be desirable. MR ARFI, however, can localize acoustic focus by measuring displacement in response to short ultrasound excitation. In MR-ARFI, motion encoding gradients can be used to encode tissue displacement by, again, using the phase of MR image [92]. Since the acoustic radiation force is proportional to the acoustic intensity of ultrasound beam [93],

$$F_{rad} \propto \frac{a I_{sppa}}{c} \ldots (1.5)$$

where a is the absorption of the medium, I is the spatial peak average intensity of the ultrasound pulse, and c is the speed of the sound in medium, monitoring displacement via MR-ARFI can provide a non-invasive tool with two uses of localizing the FUS focus and calibrating the beam intensity. In order to calculate the displacement, high strength motion encoding gradients (MEG) are used which are applied in the same direction as the displacement. Since the tissue is displaced in the same direction as that of MEG, it will undergo a different magnetic field compared to rest of the tissue position. This will result in a different phase in the area undergoing displacement when compared to non-displaced areas. The resulting phase maps can be converted to displacement using equation 1.6 as follows [93]:

$$\Delta x = \frac{\Delta \phi}{2 \gamma G d} \ldots (1.6)$$

where Δx is the total displacements, $\Delta \phi$ is change in the phases, *G* is the known MEG strength, and *d* is the MEG

duration. MR ARFI displacements have been used in small animal *in-vivo* studies [94], *ex-vivo* human cadavers [94] and in non-human primates [93]. Overall, MR-ARFI is an attractive tool to localize the FUS focus for brain applications as it can use small FUS bursts to localize the focus without the deleterious effects of skull heating which is otherwise present in ablative therapies of brain such as thalamotomies.

While MRI is non-invasive, non-ionizing, and preferred option for FUS guidance, it can quickly become very expensive where one MRgFUS procedure can cost upwards of $20,000 [95], [96] and will limit the number of people who would want to undergo MRgFUS procedures. Imaging solutions that can provide cost effective targeting can make FUS more accessible and portable.

1.4 Proposed solutions to overarching challenges with FUS

By pairing FUS with acoustically active particles and by combining it with ultrasound imaging, an all-ultrasound system can be created. Such an all-ultrasound system can enhance ablation and remove the barrier for accessibility by increasing the chances of FUS adoption. In sections below, I talk specifically about how acoustically active particles in combination with FUS and ultrasound imaging can improve FUS adoption.

1.4.1 FUS procedures in conjunction with acoustically active particles can improve ablation efficiency and mitigate off-target heating

Locoregional therapy is the process of directly treating the tissue with the goal of improving prognosis. For soft tissues diseases such as liver and breast cancers, surgery is the most common locoregional therapy. In cases where surgery is not recommended, locoregional ablative therapies are effective to prolong life and manage pain. Many such locoregional therapies for liver cancer, specifically hepatocellular carcinoma, include radiofrequency ablation or transcatheter arterial chemoembolization [97]–[101]. For breast cancer treatment, ablative options such as cryoablation [102], radiofrequency ablation [103], [104], and microwave ablation [105] have been explored. Although these methods are effective, they are invasive. HIFU is a non-invasive ablation option that can focus waves of high pressure at the desired regions to ablate tissues non-invasively. As covered in previous sections, FUS has

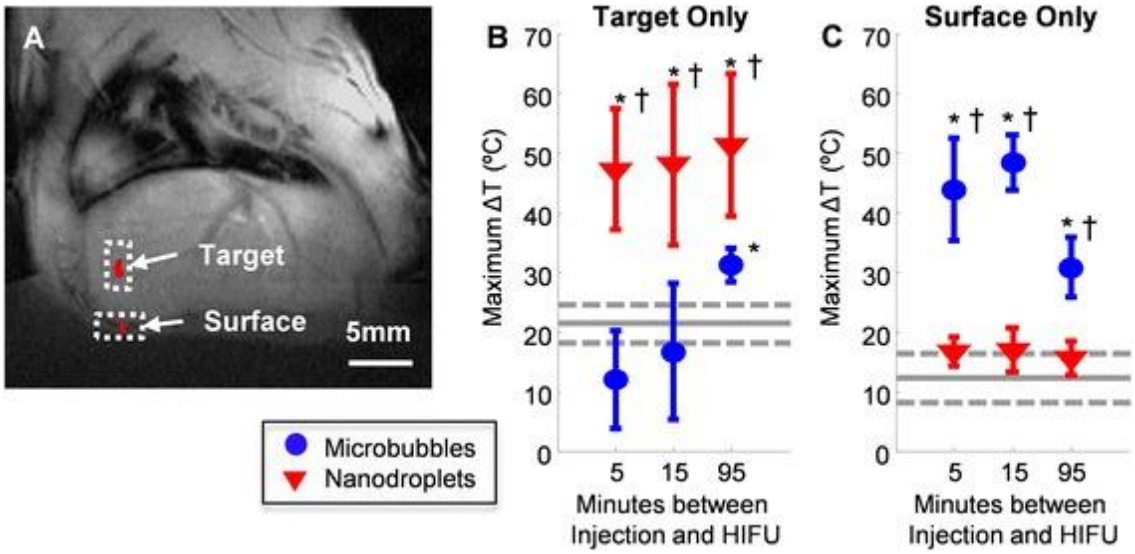

Figure 1.3: PSNDs cause more focal heating and less surface heating. Moyer et al [75] showed that by using phase shift nanodroplets, heating at the surface can be minimized whereas heating at the target location can be maximized thereby reducing any off-target heating.

been shown to cause substantial ablative outcomes at high pressures and energies which have resulted in off-target effects such as skin burns and skull injuries [11], [12]. When paired with acoustically active particles, FUS can be employed at relatively lower pressures as it would need less pressures and energies to cause desired effects and consequently result in reduced pre-focal effects [106], [107]. However, if we combine HIFU with acoustically active particles such as microbubbles, we can accelerate heating and improve heating rate and efficiency. However, uses of microbubbles in a clinical setting presents challenges. MBs tend to induce off-target heating, primarily in the near field [14] because they amplify heating regardless of their location. Additionally, high concentrations of MBs can attenuate acoustic penetration into deeper tissues. Finally, they are too large to extravasate into vascular space and remain localized within the blood vessels [70], [71] and have a short circulation half-life [72].

Phase-shift nanodroplets (PSNDs) can serve as a better ablative agent. PSNDs are nanometer-sized liquid particles that can be intravenously injected. They undergo a phase shift from liquid to gas and can convert in MBs when sonicated above a threshold pressure [108]. After the conversion, MBs can be exploited to accelerate heat. Because PSNDs only convert in regions where pressure thresholds are met, they amplify heating only in the focal region and limit pre-focal heating as shown in Fig 1.3. Precise focal ablation using phase-shift nanodroplets [109] have proven to mitigate many off-target heating in tissue mimicking phantom and in rat liver [110]. In one study,

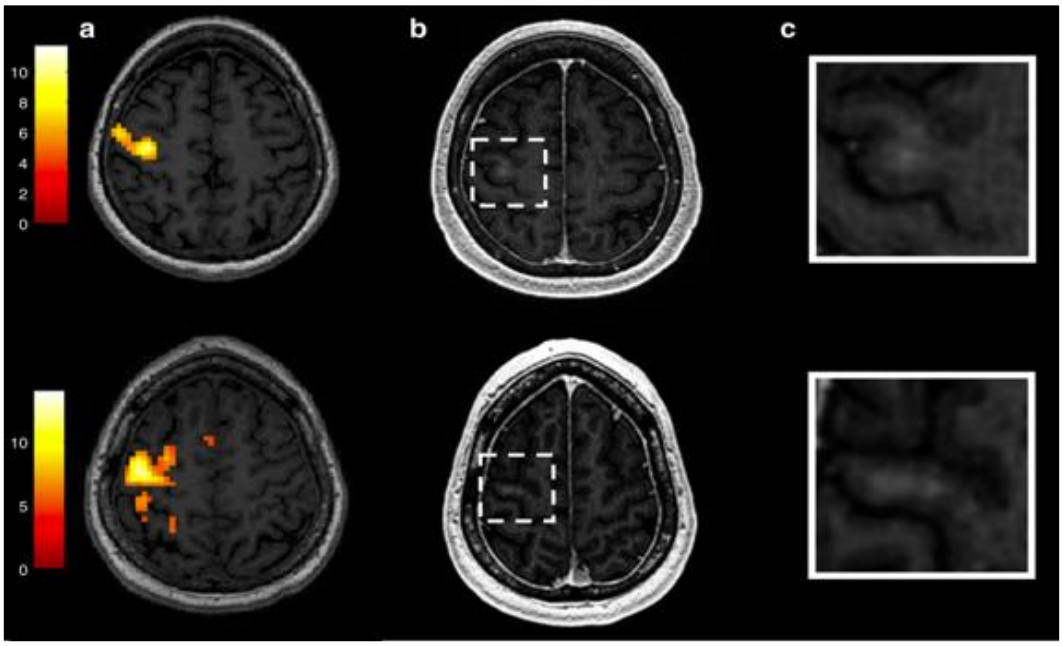

Figure 1.4: BBB opening in clinical trial using MRgFUS. Abaraho et al [5] used functional MRI to localize hand motor region in humans and opened blood brain barrier in 2 ALS patients above in the hand motor regions.

researchers observed a temperature rise of 130% and an ablation volume 30 times greater with PSNDs vs without PSNDs in the rat liver [111]. Moreover, the circulation time of PSNDs is substantially longer than that of microbubbles [106]. This provides enhanced permeability and retention of PSNDs in heterogeneous and leaky vasculature of tumors. While PSNDs can mitigate off-target heating, its potential to improve ablation efficiency needs further testing. In chapter 3 of my thesis, I present a study that combined PSNDs with multi-focal ablation patterns to improve ablation efficiency and mitigate off-target heating.

1.4.2 FUS in conjunction with MBs can opening blood brain barrier at lower pressures

The tight junctions between endothelial cells on the vessels in the brain form the blood brain barrier (BBB) which help maintain brain homeostasis. While BBB prevents the entry of potentially harmful substances, it also limits intracerebral delivery of almost all pharmaceuticals developed to treat various neurological diseases. Several promising strategies have been proposed that harness active transport systems but these techniques have limited carrying capacity and required to be tailor made [112], [113]. Opening of BBB can facilitate drug transportation. Among several ways to deliver drug across BBB [114], one of the most popular ways is to use FUS in conjunction with microbubbles. FUS when combined with microbubbles, can open BBB in a transient, non-invasive and safe

manner [5], [23], [56], [86], [114]–[116]. The feasibility of using microbubbles to open BBB was shown in 2001 where researchers show that pressures of less than 1MPa can safely open BBB in rabbits without damage after administration of MBs but in absence of MBs, it can take upwards of 4MPa to open BBB [55] . Yet another study showed the feasibility of opening BBB with microbubbles where researchers showed significant quantitative differences in retention of Gadolinium at 60 and 90 mins in pigs treated with ultrasound + MBs compared with ultrasound alone to open BBB [117]. Since then, BBB opening has been performed by various groups to deliver drugs for Alzheimer's and Parkinson's disease [56], to study immune responses of glioblastoma after BBB opening [118], to deliver chemotherapy drugs [6], and to study somatosensory responses after BBB opening [87]. These animals studies paved path for blood brain barrier opening in humans [5] to treat Alzheimer's Disease non-invasively with focused ultrasound [53]. In chapter 5, I present my work on combining FUS with MBs to open BBB.

1.4.3 FUS in conjunction with nanoparticles can allow for drug delivery without opening the blood brain barrier in small animals

One of the primary ways of delivering drugs via FUS is facilitated by FUS induced BBB opening. However, drug delivery can also be achieved by sonicating nanoparticles that release drugs upon FUS interaction. The released drugs can then cross blood brain barrier. In prior studies, researchers showed the feasibility of releasing propofol from an ultrasound gated nanoparticles at MI>1 [22], [119]. They also showed that the release of propofol from these particles could silence the seizures in an acute seizure rat model [22], [119]. In yet another study, researchers released Pentobarbital after phase shifting Pentobarbital loaded nanodroplets upon FUS sonication [60]. The pentobarbital release acted as an anesthetic which were detected through behavioral changes and contralateral motor deficits. In chapter 4, I present my study that examines acoustic responses when propofol particles are sonicated.

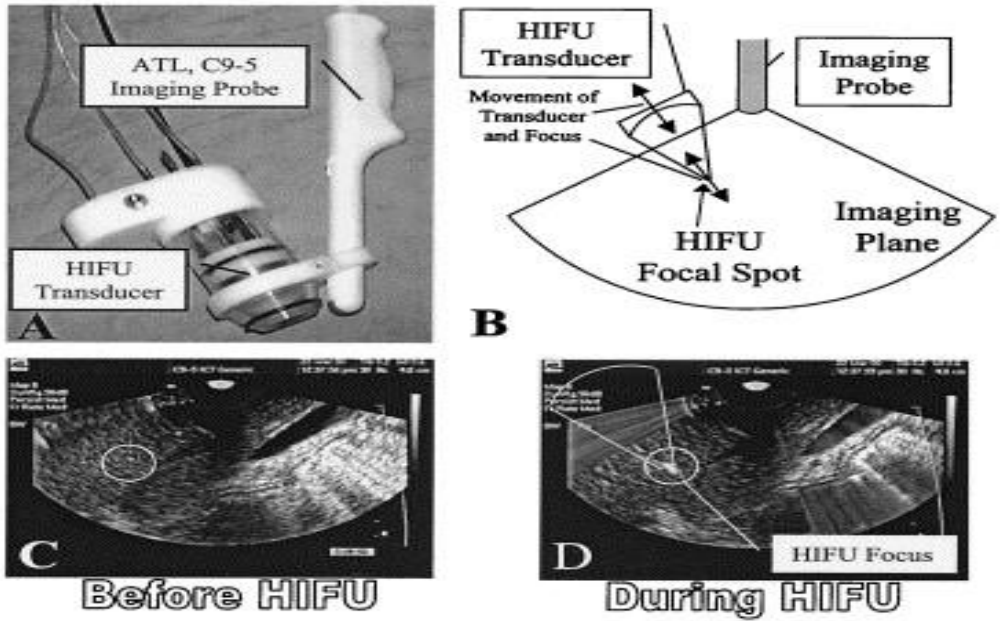

Figure 1.5: Ablating soft tissues using USgFUS. The focus of the FUS transducer is in the plane of imaging transducer. Reprinted from Real-time visualization of high-intensity focused ultrasound treatment using ultrasound imaging, 27, Shahram Vaezy, Xuegong Shi, Roy W Martin, Emil Chi, Peter I Nelson, Michael R Bailey, Lawrence A Crum, 33-42., Copyright (2001), with permission from Elsevier

1.4.4 Targeting and visualizing therapy using ultrasound

1.4.4.1 Ultrasound uses to monitor temperature change

Ultrasound can be used in FUS procedures to monitor temperature changes. Ultrasound thermography [120]–[122] and back scatter energy[123], [124] can monitor temperature rise in tissues due to FUS absorption at both therapeutic and sub-therapeutic levels. These methods work well for only moderate changes in temperature and fail at high temperatures. High frame rate imaging demonstrated that there are significant decorrelations in the echo data from the focus location at high temperatures due to the transient events which are consistent with vaporization of liquid into gas [125], [126]. Detection of these transient events can be a reliable indicator of thermal lesion formation for exposure durations > 100ms.

1.4.4.2 Ultrasound imaging can also help with pretreatment planning.

Pretreatment planning for hyperthermia caused due to FUS, traditionally, entailed using acoustic and thermal simulation. Recently, an image-based algorithm has been proposed where refocusing of FUS array is done in the presence of strong scattering targets. Ultrasound images of the target regions included Plexiglas to simulate the ribs to define rib locations in HIFU path. After experimental validation of the algorithm, authors showed that the focusing gain at the target can be improved while minimizing the exposure to the ribs [127]–[129]. In yet another

study [130], researchers used manual segmentation algorithms to identify tissue types based on known anatomy. The segmentation algorithm modelled the temperature evolution and thermal dose accumulation during HIFU treatment. Ultrasound images, additionally, can be essential to finding the focus of the FUS transducer. Research literature notes several applications of ultrasound guided FUS (USgFUS) procedures, such as in Fig 1.5, that provide image guidance and monitoring of FUS procedures in soft tissues. For example, one of the most common USgFUS procedures involve the use of B-Mode imaging to visualize and treat hepatocellular carcinoma [27].

1.4.4.3 Ultrasound can be used to map acoustic signals originating during FUS induced microbubbles assisted BBB opening.

Therapeutic ultrasound, as mentioned in above sections, is a promising tool for non-invasive surgery/ablation of tumor or drug delivery in brain via neuromodulation or blood brain barrier opening. The underlying mechanisms of ablation and neuromodulation are either thermal which arise from viscous absorption of therapeutic pulse or mechanical which arise from sustained or unstable oscillations of microbubbles giving rise to stable or inertial cavitation. While stable cavitation by itself can cause certain bioeffects such as reversible opening of blood brain barrier, inertial cavitation can cause harmful bioeffects such as hemorrhaging of the vessels. In tumor ablation, damaging of the vessels is desirable. However, for brain applications, hemorrhaging can introduce complications and is an undesirable outcome of FUS treatment. Thus, it is crucial to monitor and map the extent of treatment for brain applications. Current treatment monitoring tools include B-Mode ultrasound and magnetic resonance imaging (MRI). B-Mode ultrasound, although cost effective, will give no information about inertial cavitation. MRI is very costly and can only inform us of thermal changes. Passive acoustic mapping (PAM) is an all-ultrasound method that can enable mapping sources that generate non-linear acoustic emissions[131]. PAM is sensitive to monitoring both stable and inertial cavitation and can spatially locate the sources of acoustic emissions. It is now increasingly being adopted to monitor safe opening of BBB in animals [132], [133]. In chapter 5, I use PAM to monitor tissue damage during FUS mediated BBB opening procedure.

1.4.4.4 Ultrasound imaging for brain applications

When it comes to brain applications, such as BBB opening, visualizations of treatment zones via B-Mode is not feasible due to attenuation of ultrasound waves in the presence of the skull [134]. Ultrasound imaging to guide FUS for brain applications have been used so far only in animal models where to accurately place the FUS focus in

the desired regions of the brain, some researchers have used a cross grid on the mouse skin of the skull which is visible in B-Mode image of the imaging transducer co-axially aligned to a single element FUS transducer [116]. The procedure was successful, with targeting accuracy within 2mm. In another study[135], researchers targeted hippocampus within 0.5mm of the actual FUS focus with a single-element FUS transducer to open BBB in mice by using a similar cross-grid system with anatomical landmarks as guidance. Researchers, however, noted that sutures were not visible for all kinds of mice. Use of ultrasound imaging to guide FUS focus in brain has not been demonstrated in human applications yet. However, transcranial Doppler (TCD) ultrasonography is in practice since the 1980s. TCD is a non-invasive method to assess critical conditions including vasospasm in subarachnoid hemorrhage, traumatic brain injury, acute ischemic stroke, and brain stem death [136]. It also helps in investigating the cerebrovascular systems. TCD uses low-frequency (≤ 2MHz) transducer and measures cerebral blood flow velocity through insonating the basal cerebral arteries through relative thin bone windows on the scalp. TCD can be combined with color flow and power Doppler in clinical systems to give more information about intracranial arteries, specifically their diameter, velocity, and relationship with adjacent structures [136]. However, the blood flow information is restricted to big main vessels. In the last decade, power Doppler imaging has evolved tremendously with continued efforts in making it transcranial. Power Doppler is different from color Doppler as it only provides an intensity image of the vessels with no information about velocity or flow direction of blood in vessel. The physics behind power Doppler and color Doppler is presented in methods section.

One of the first efforts on improving sensitivity using power Doppler was published in 2010 where a combination of high frame rate imaging with microbubbles at 15MHz coupled with singular value decomposition (SVD) filtering revealed smaller vasculature in craniotomized rat [137]. The sensitivity improved for up to 25 times when compared to conventional methods [137]. Not only were researchers able to improve sensitivity, but they were also able to create velocity maps in very small vessels, which was not possible with conventional ultrasound imaging algorithms. This research paved the path for functional ultrasound imaging where researchers used high frame rate imaging at 15 MHz and coupled it with MBs to map activation of barrel cortex in craniotomized rats when rats' whiskers were stimulated [138]. Additional experiments in rats were then performed where their hindpaw was stimulated and activation was seen in sensory motor cortex regions of the rat brain [139]. This study was different from the prior one wherein the activations were also seen transcranially. This showed the robustness of functional ultrasound technique even in the presence of highly attenuating object such as skull. The technology improved to image 3D functional ultrasound in mice and rats [140]–[142] to give a wholesome information about

regions undergoing activations in response to various stimulations. Finally, feasibility of transcranial functional ultrasound through a neonatal brain was recently reported using a 6MHz probe [143], [144]. While SVD filtering method presents an excellent clutter rejection method, images created after SVD filtering were still limited by diffraction limit imposed to us by the ultrasound imaging transducer. This may present problems when trying to image at lower frequencies through the thicker skulls of humans. In order to overcome diffraction limit, researchers developed ultrasound localization microscopy (ULM) [145]. The acquisition for ultralocalization microscopy worked similarly as acquisitions for functional ultrasound but the treatment of data was different where in ULM researchers used SVD filtered image to track MBs from one frame to next frame. After tracking, localization methods such as radial symmetry or weighted average method is used to localize the MBs with sub-wavelength precision, thereby overcoming issues of diffraction limit [146]. In chapter 5, I use power Doppler imaging to guide my FUS transducer to open BBB and in chapter 6, I use power Doppler imaging to study functional response to external stimulation in rats. Using power Doppler images, I also create super resolution images of craniotomized rat brain.

1.5 Innovation

Focused ultrasound is a very attractive technology that causes ablation in soft tissues and cause blood brain barrier opening and local delivery of anesthesia in brain non-invasively while being non-ionizing. FUS allows targeting spatially precise areas in soft tissues and in the brain with millimeter scale focal area. To effectively use FUS, it is important to mitigate the off-target effects that occur due to needing excessive pressures to cause a clinically relevant outcome. Additionally, it is important to aim the FUS transducer accurately

The goal of this work is to overcome off-target heating during FUS ablation procedures and combine it with ultrasound imaging to make the FUS treatment more affordable. We achieved this by combining PSNDs with multi-focal ablation patterns to increase ablation efficiency and volume which can overall benefit breast cancer treatment option. We also developed methods to combine FUS transducer and imaging transducer to create an all-ultrasound method that can target and receive passive signals which could be indicative of tissue damage. We achieved this by using passive receive signals to monitor and characterize echoes that were produced when ultrasound gated nanoparticles released propofol upon FUS application.

We developed additional methods that combined power Doppler ultrasound imaging and fast frame rate passive acoustic mapping algorithm to accurately target brain regions and map and monitor cavitation activity during steered FUS sonication of MBs in an *in-vitro* and *in-vivo* setting to open BBB. We, finally, used power Doppler ultrasound imaging to map blood flow activity in the rodent brain at varied stimulatory frequencies. This gave us information

about how blood flow in the rodent brain changed in response to external stimulation and could potentially be combined with FUS transducer to study effects of neuromodulation at high spatio-temporal resolution.

1.6 Chapter breakdown

Chapter 1 goes into details of applications of microbubbles (MBs) and nanoparticles (NPs) in FUS. It also talks about current imaging methods that are used for targeting desired regions in the brain.

Chapter 2 goes into detail about relevant prior research and developmental work that has been integral for my thesis and later chapters.

Chapter 3 appears in its entirety as: A. Singh, A. G. Nyankima, M. A. Phipps, V. Chaplin, P. A. Dayton, and C. F. Caskey, "Improving the heating efficiency of high intensity focused ultrasound ablation through the use of phase change nanodroplets and multifocus sonication," *Phys. Med. Biol.*, May 2020. It presents my original work that combined multi-focal HIFU with PSNDs in tissue like static phantoms to aid in greater volumetric ablation.

Chapter 4 appears in its entirety as: A. Singh *et al.*, "Using Passively Detected Acoustic Signals to Characterize Ultrasound Gated Nanoparticles," in *2021 IEEE International Ultrasonics Symposium (IUS)*, 2021, pp. 1–4. It presents my original works where I use passive receive signals to characterize phase change of nanoparticles from liquid to gas.

Chapter 5 presents my work where I developed spectral value decomposition method (SVD) for applications of steering our FUS transducer sonicating at a desired location in the cellulose tube with MBs flowing. It also presents further developments on passive acoustic mapping where the echoes generated via MBs upon FUS sonication was passively recorded using 128 element imaging transducers. The passively recorded signal was beamformed to reconstruct passive acoustic map which informed us of regions undergoing cavitation effects under FUS application. I applied developments from chapter 5 in an *in-vivo* setting to open BBB and point registered power Doppler image with MRI BBB opened image to overlay BBB opened area over the PAM maps and used registered data to calculate targeting error vector. The manuscript resulting from this chapter is under review at Scientific Reports.

Chapter 6 describes a second use of power Doppler imaging in measuring blood flow changes in rat brain in response to external stimuli in rat. The manuscript resulting from this chapter is under preparation for submission.

Chapter 7 covers my conclusions of all my results and propose future directions of my projects.

CHAPTER 2: Ultrasound physics and its interaction with tissues and particles

FUS, in absence of acoustically active particles need high pressures and powers to cause clinically effective outcome [55]. In doing so, it can introduce pre-focal heating and skin heating [11]. One way to mitigate this is to use acoustically active particles that can enhance acoustic absorption only at the focus at low powers [107]. Combining acoustically active particles with desired pressure fields, we can enhance ablation efficiency. With this in mind, I start this chapter by delving into ultrasound acoustic physics for therapies. Solving the equation of pressure wave in frequency domain using Green's theorem, Lord Rayleigh and Arnold Sommerfeld derived Rayleigh-Sommerfeld pressure equation that can predict pressure field in the desired region provided we know the surface velocity near the boundary of the transducer. With the correct pressure field, the ultrasound would converge at the desired region with the highest pressure at the focus of the ultrasound. Rayleigh-Sommerfeld equation has been used throughout this dissertation to create desired beam patterns by changing the phase and amplitude of the elements of the transducer [147].

While predicting correct pressure fields is vital, targeting pressure fields at a desired region such that ultrasound is focused on that region is also of utmost important. In this chapter we present methods wherein we used ultrasound power Doppler image [139], reconstructed from ultrasound imaging array registered to our FUS transducer, to steer our FUS transducer at desired regions. Collectively, these methods can target and perform FUS procedures using an all-ultrasound system.

While accurate imaging and targeting is one of the biggest challenges in fabricating an all ultrasound system, it is also important to develop methods that can monitor echoes that arise from FUS interaction with acoustically active particles as these echoes may contain information about tissue damage [132], [148]–[153]. When FUS interacts with acoustically active particles such as MBs, it can result in contraction and expansion of MBs. When MBs can maintain its size during contraction and expansion, it produces stable cavitation and promotes transient activities such as BBB opening [154], [155]. Stable cavitation echoes contain harmonics and ultra-harmonics of fundamental FUS frequency [149], [150], [156]. However, at high pressures, MBs can violently collapse and destroy vessels they are in, and result in inertial cavitation signal which is usually indicative of permanent tissue damage [132], [157]–[159]. Inertial cavitation echoes contain wideband signal, which are frequencies other than harmonics and ultra-harmonics. Destruction of tissue maybe an ideal outcome for soft tissue cancer ablation therapies, but it can lead to damage of

the nervous system if these echoes are not monitored. In this thesis we present passive acoustic mapping as a method that can create spatial maps of regions undergoing cavitation during FUS procedures using passive receive signals recorded in an imaging transducer acquired at high frame rate during FUS procedures [116], [131], [148], [160]–[162].

2.1 Fundamental physics of FUS

FUS was first shown to be an effective treatment modality in 1950s when Fry et al. showed that FUS caused damage to tissues *in-vivo* via thermal ablation [163]. Following an initial report on FUS's influence on tissues by Fry et al, researchers quickly adopted FUS for thermal therapies starting in the 1980s [77]. FUS works by converging acoustic waves to a desired region with. Acoustic waves in ultrasound are generated by vibrations from piezoelectric transducer which is coupled to the skin via gel or water and can be derived by combining differential equations that describe conservation of momentum, conservation of mass, and the relationship between pressures and density as follows:

$$\frac{\partial u}{\partial t} = -\frac{1}{\rho_0}\frac{\partial p}{\partial x} \dots \quad (2.1)$$

$$\frac{\partial \rho}{\partial t} = -\rho_0 \frac{\partial u}{\partial x} \dots \quad (2.2)$$

$$p = c_0^2 \rho \dots \quad (2.3)$$

where u is the particle velocity, p is pressure, ρ is the density, ρ_0 is the ambient density, and c_0 is the speed of sound.

All three equations can be combined to yield wave equation in a homogeneous as follows:

$$\nabla^2 p - \frac{1}{c_0^2}\frac{\partial^2 p}{\partial t^2} = 0 \ \dots \ (2.4)$$

A one-dimensional solution to equation 4 can be written as follows:

$$p(x,t) = p_0 \sin(\omega t - kx) \dots \quad (2.5)$$

where ω is the angular frequency, k is the wavenumber, and p_0 is the ambient pressure.

The pressure waves in equation 5 undergo alternating phases of compression and rarefaction as they propagate through a medium. In the case of compression, molecules are forced together which results in the increase of the density of the medium. In the case of rarefaction, molecules are spaced apart to allow for expansion, thereby causing

a reduction in density of the medium.

2.2 Creating desired pressure field patterns

Acoustic waves in ultrasound are usually generated by vibrations from piezoelectric transducer which is coupled to the skin via gel or water. At low pressures the relationship between pressure in the medium is linearly proportional to the voltage that drives piezo elements. It, however, becomes increasingly non-linear as the pressure is high. Wave equation in a homogeneous medium can be modelled by:

$$\nabla^2 p - \frac{1}{c_0^2}\frac{\partial^2 p}{\partial t^2} = 0 \ldots \quad (2.6)$$

Taking Fourier transform of time domain pressure wave equation 2.6 will yield Helmholtz equation for $P(x, \omega)$ as :

$$\nabla^2 P - \frac{\omega^2}{c_0^2} P = 0 \ldots \quad (2.7)$$

Calculation of pressure disturbance P at any observation in space can be solved by applying green's theorem which states that if $P(x, \omega)$ and $G(x, \omega)$are any two disturbances in volume V then:

$$\iiint (P\nabla^2 G - \mathrm{G}\nabla^2 P)\, dV = \iint \left(P\frac{\partial G}{\partial n} - G\frac{\partial P}{\partial n}\right) ds \ldots \quad (2.8)$$

Within the volume, the disturbance G satisfies the Helmholtz equation and equation 2.8 will reduce to:

$$\iint \left(P\frac{\partial G}{\partial n} - G\frac{\partial P}{\partial n}\right) ds = 0 \quad \ldots \quad (2.9)$$

Applying appropriate Kirchoff boundary conditions and Sommerfeld radiation conditions,

$$P(x, \omega) = \frac{1}{4\pi}\iint_{S1} \left(\frac{\partial P}{\partial n} G - P\frac{\partial G}{\partial n}\right) ds \ \ldots \quad (2.10)$$

In order to solve equation 2.10, an appropriate Green's function needs to be determined. Lord Rayleigh and Arnold Sommerfeld developed a method to solve and proposed the following green's function:

$$G(x, \omega) = \frac{\exp\,(jkr_{01})}{r_{01}} - \frac{\exp(jk\widetilde{r_{01}})}{\widetilde{r_{01}}} \ \ldots \quad (2.11)$$

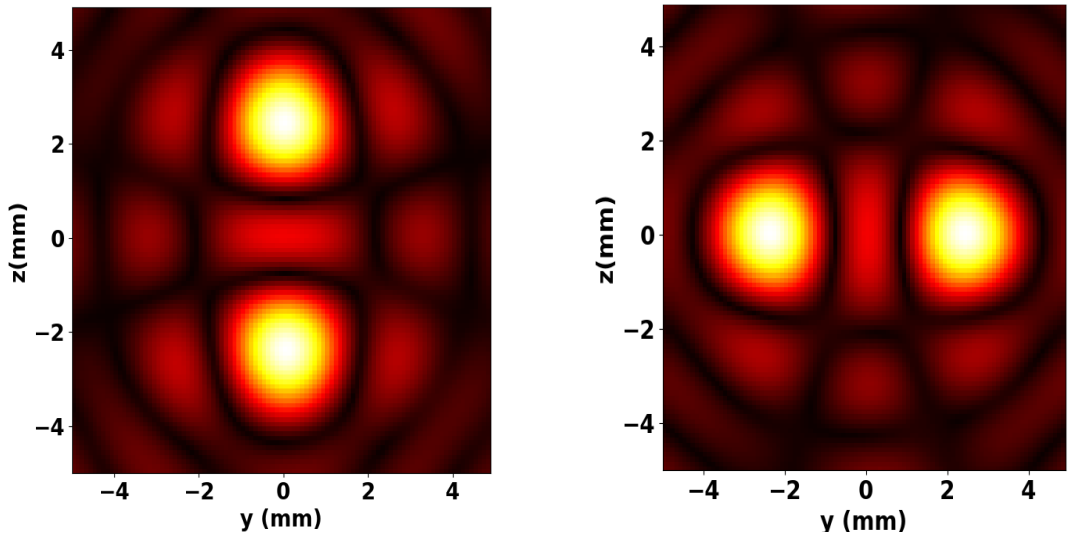

Figure 2.1: Creation of desired pressure beam pattern. Desired pressure fields that can be created using equation 12. Equation 12 can be used to set amplitude and phases of a phased array to create multi-focus pressure fields.

This enabled them to solve equation 5 and come up with acoustic pressure inside the boundary as:

$$P(x,\omega) = j\frac{\rho\omega}{2\pi}\iint \frac{\exp j\omega\, r_{01}}{r_{01}}\boldsymbol{u}(x',\omega).\hat{\boldsymbol{n}}dA' \quad \ldots \quad (2.12)$$

where the integral was taken over the surface boundary. $\boldsymbol{u}(x',\omega)$ represents the surface velocity of the vibrating transducer at the boundary and $\boldsymbol{n}$ is the surface normal vector. Equation 2.12 is called as Rayleigh-Sommerfeld equation, and this formed the basis of my experimental design in chapters ahead.

In time domain, complex pressure at a point in acoustic field yields the following Rayleigh-Sommerfeld equation[164]:

$$p(r) = \frac{j\rho ck}{2\pi}\int_{S'} u(r')\frac{e^{(-jk|r-r'|)}}{|r-r'|}dS' \ldots (2.13)$$

where $j = \sqrt{-1}$, ρ is the density, c is the speed of sound, k is the wavenumber, S' is the surface of the source, u is the normal velocity of the source surface, and r and r' are the observation and source points, respectively.

If a phased array transducer that has N number of elements, pressure at M control points at position $r = r_m$ where $m = 1,2, \ldots M$ can be written as

$$p(r_m) = \frac{j\rho ck}{2\pi}\sum_{n=1}^{N} u_n \int_{S'} \frac{e^{(-jk|r_m - r_n{}'|)}}{|r_m - r_n{}'|} dS' \ldots (2.14)$$

If we let

$$H(m,n) = \frac{j\rho ck}{2\pi}\sum_{n=1}^{N} \int_{S'} \frac{e^{(-jk|r_m - r_n{}'|)}}{|r_m - r_n{}'|} dS' \ldots (2.15)$$

then we can represent equation 2.13 in matrix form where:

$$Hu = p \ldots (2.14)$$

where $u = [u_1, u_2, \ldots u_N]^t$ and $p = [p(r_1), p(r_2), \ldots p(r_M)]^t$

One can use equation 2.14 can help solve for amplitude and phase of *N* transducer elements that can generate desired pressure at *M* control points. When *M*<*N*, *H* has full rank and minimum-norm solution of the matrix in equation 2.14 can be solved by:

$$\hat{u} = H^{*t}(HH^{*t})^{-1}p \ldots (2.15)$$

where H^{*t} is the conjugate transpose of *H*.

Combining equation 2.14 and 2.15, we can solve for $\hat{u}$, which determines amplitude and phases of the transducer to form a particular pressure field in Fig 2.1. This is especially important for creating accurate pressure fields to sonicate at the desired regions for neuromodulation or to enhance ablation.

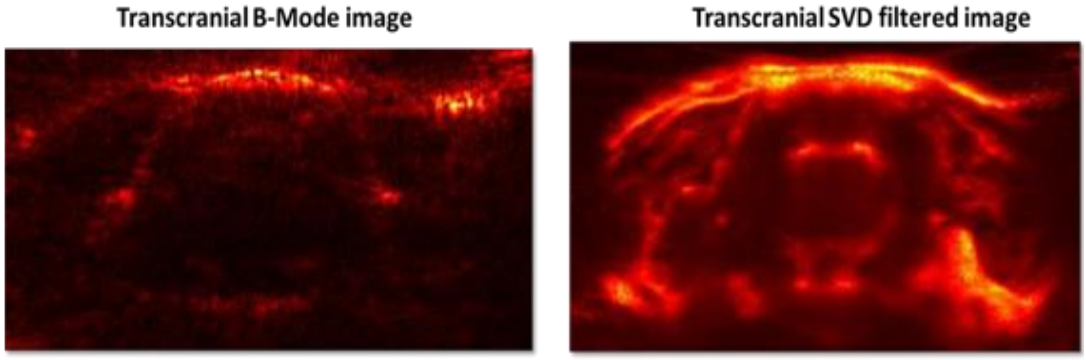

Figure 2.2: SVD filtering can reveal vasculature via transcranial ultrasound imaging at 9MHz: Transcranial B-Mode image of the rat brain reveals the outline of the skull. There is not much signal from inside the brain. SVD filtering can reveal vasculature inside the brain and can help with ultrasound image guidance for FUS applications.

2.3 Creating an all-ultrasound system for imaging and targeting

2.3.1 Principles of power Doppler imaging and ultralocalization microscopy

When ultrasound passes through a blood vessel, a small part of the energy is backscattered by red blood cells. Ultrasound probe can record these echoes. Using the principles of Doppler Ultrasound imaging, one can detect the motion of these RBC's by repeatedly pulsing ultrasound and studying the temporal variations of the successive backscattered signals. These signals would otherwise not be present in a B-Mode image. Signal at pixel position (x, y) can be denoted as $z(x, y, t_i)$, where $i = 1 \dots N$ are the successive pulse emissions, y is the depth axis, and x is the axis along the probe array. Here complex signal z is obtained after IQ demodulation and beamforming steps [134], [138].

After the acquisition:

- signal matrix $z(x, y, t_i)$ is reshaped into a 2-D matrix $z(x * y, t)$.
- Matrix $z(x * y, t)$ is decomposed into its singular values. Its singular values, and left and right singular vectors are obtained after decomposition.
- [U,S,V]=svd(z);
- Highest singular values, which represent slow moving tissue signals, are set to zeros such that signals only from moving tissues or RBCs are left.
- Cutoff=10;

- S_new(1:cutoff)=0;
- A new matrix is the formed using new singular values.
- z_f=U*S_new*V;
- z_f=reshape(z_new,[length(x),length(y),length(t)]);

This z_f matrix is now a SVD filtered matrix such that it only contains information from moving RBC in figure 2.2. The filtered signal (which consists of signal from blood and noise) is denoted as $z_f(x, y, t_i)$. Parameters that are commonly extracted and displayed from the filtered signal is: the axial blood velocity at each pixel or the mean intensity of the Doppler signal at each pixel. The former creates a color Doppler image, and the latter creates power Doppler image.

2.3.1.1 Color Doppler

While the mean intensity image shows smaller blood vessels, it gives no information about blood flow velocity and direction. In order to accurately calculate blood flow velocity, we need to employ color Doppler. Color Doppler works on the Doppler principle [165] which exploits the difference between the frequency of reflected ultrasound and transmitted ultrasound. This difference is directly proportional to the velocity of reflecting interface that is relative to the ultrasound receiver and is a result of Doppler effect. The Doppler equation, which describes this relationship can be written as follows:

$$\Delta F = (F_R - F_T) = [(2F_T \times v)/c]\, cos\theta \ldots (2.16)$$

where ΔF is the Doppler frequency shift, $F_R$is the frequency of sound that is reflected from a target, F_T is the frequency of sound that is transmitted from the ultrasound transducer, v is velocity of target moving away from or towards the transducer, c is speed of sound in the medium, and θ is the angle between the axis of flow and incident ultrasound beam. The velocities are color coded such that flow that travels away from transducer, which has a negative Doppler shift, is depicted in blue whereas the flow traveling towards the transducer is depicted in red.

2.3.1.2 Power Doppler

Power doppler mode was created after color doppler mode in order to better detect small blood vessels. The reason why power doppler is chosen over color doppler is because color doppler is sensitive to aliasing and noise whereas estimation of signal intensity is more robust to noise and relatively insensitive to aliasing. Hence, power doppler is more suited for various applications, in particular to identify small vessels. Power Doppler, although gives no information about blood velocity, it does give information about the blood volume within the pixel [134], [138], [142]. The goal of this aim is to follow the hemodynamics in very small cerebral vessels, which can be done via

Doppler imaging. The mean intensity I displayed in the power Doppler mode can be calculated as:

$$I(x,y) = \frac{1}{N}\sum_{i=1}^{N} |z_f(x,y,t_i)|^2 \quad \ldots (2.17)$$

In order to increase sensitivity of the estimation of I, we must increase N and/or reduce the effect of the noise on $z_f(x,y,t_i)$. The μDoppler sequence designed by Mace et al is aimed at increasing the sensitivity.

2.3.2 Ultrasound Localization Microscopy

After obtaining power Doppler images, specifically after injecting MBs, we can reconstruct the tracks where MBs were present to an ultrasound localized image which has better resolution that ultrasound imaging transducer's resolution. Images obtained after creating tracks overcomes the diffraction limit posed onto them by ultrasound imaging transducer. To create a successful super resolution image, two most important steps should be carried out. The first is localizing MBs in every power Doppler image. One of the most popular ways to localize image is to use weighted average algorithm [146]. Let us assume that after applying an SVD filter to an image, we have an image of microbubble that is composed of a grid of [N_z,N_x] pixels. To get the position of the centroid of the MB, we interpolate to upsample image of the grid by a resolution factor, res. Following upsampling, the grid is now of the size [res * N_z, res * N_x]. The interpolated intensity I_{sr} can now be expressed as:

$$I_{sr}(i,j) = \sum_{(k_i,k_j)\in Zq} I_k \emptyset_{int}(i-k_i, j-k_j) \ldots (2.17)$$

where *(i,j)* belongs to interpolated space Z_{sr} and *(k_i,k_j)* belongs to original space Zq. The function $\emptyset_{int}$ is called as a synthesis function which satisfies interpolation properties. If we have centered our subset space Z_k on a maximum known value I_k at z_{ck}, the centroid of microbubble *(z_c,x_c)* in the interpolated image can be presented as:

$$z_c = z_{ck} + \frac{\sum_{i=-|\frac{f_z}{2}|}^{|\frac{f_z}{2}|}\sum_{j=-|\frac{f_x}{2}|}^{|\frac{f_x}{2}|} I(i,j)w_z(i,j)}{\sum_{i=-|\frac{f_z}{2}|}^{|\frac{f_z}{2}|}\sum_{j=-|\frac{f_x}{2}|}^{|\frac{f_x}{2}|} I(i,j)} \ldots (2.18)$$

$$x_c = x_{ck} + \frac{\sum_{i=-|\frac{f_z}{2}|}^{|\frac{f_z}{2}|}\sum_{j=-|\frac{f_x}{2}|}^{|\frac{f_x}{2}|} I(i,j)w_x(i,j)}{\sum_{i=-|\frac{f_z}{2}|}^{|\frac{f_z}{2}|}\sum_{j=-|\frac{f_x}{2}|}^{|\frac{f_x}{2}|} I(i,j)} \ldots (2.19)$$

with $w_z(i,j) = i;\ w_x(i,j) = j$ representing weights applied, f_z and f_x = Full width half max of the intensity profile in *z* and *x* direction respectively. The values (z_{ck}, x_{ck}) = {I(z,x)>I(I,j),∀ (I,j)}.

Now that we have localized MBs, it is important to track them from one frame to another. To track these MBs, we implemented Kuhn-Mukres algorithm [146] where for each particle, we computed the squared distance to all of the particles in the next frame. We were, then, able to find the optimal pairing of particles from one frame to another by minimizing the total squared distance.

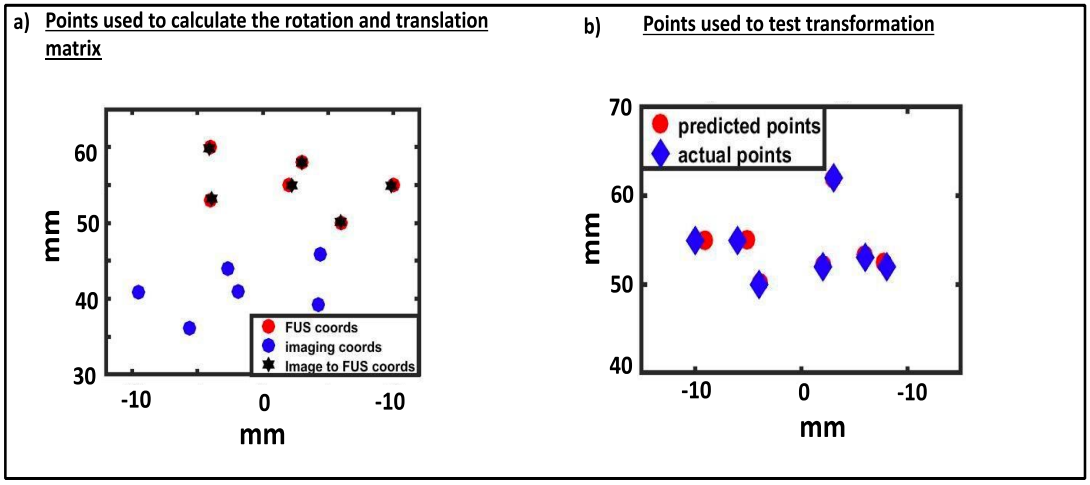

Figure 2.3: Registering imaging transducer to FUS transducer. a) Imaging coordinates in blue circles were registered to FUS coordinates in red circle. These points were used to solve for equation 1 to yield R (rotation matrix) and t (translation matrix). The FRE was 0.18mm. The R and t values obtained were applied to blue circular points to yield black star points. The values of R and t were used to then transform other imaging coordinates into FUS coordinates. c) Another 7 non-fiducial imaging points were then registered to FUS coordinates. The TRE for this registration was 0.59 $\pm$ 0.26mm.

2.3.3 Registering imaging transducer with FUS transducer

Registering imaging transducer with FUS transducer can enable steering FUS transducer with the help of imaging transducer. Imaging transducer-based coordinate system in Fig 2.3a can be registered to FUS based coordinate system using a point-based registration between two set of points in imaging transducer space ($\mathbf{x_i}$ for i = 1 to N) and FUS transducer space ($\mathbf{y_i}$ = 1 to N). A translation matrix $\boldsymbol{t}$, and a rotation matrix $\boldsymbol{R}$ are needed to align points in imaging space with corresponding points in FUS space [166]. Since there are existing errors in these measured location, application of rotation and translation matrix will lead to points that may not be perfectly aligned . In order to find $\boldsymbol{t}$ and $\boldsymbol{R}$, we must minimize the root mean square distance between these set of points. This distance, referred to as fiducial registration error (FRE) can be calculated as:

$$FRE^2 = \frac{1}{N}\sum_{i=1}^{N} |R\boldsymbol{x_i} + \boldsymbol{t} - \boldsymbol{y_i}|^2 \quad \ldots \quad (2.20)$$

The optimal translation can be found by:

$$\mathbf{t} = \bar{\boldsymbol{y}} - R\bar{\boldsymbol{x}} \quad \ldots \quad (2.21)$$

where the bar represents a mean from I = 1 to N. To find the most optimal rotation matrix, number of algorithms have been developed. In addition to FRE, one other error is of interest to us. This error is called target registration error, and this measures the error between registering two non-fiducial points in two spaces in Fig 2.3b. The smaller the TRE, the more accurate our registration was. TREs for *in-vivo* studies are usually within 3mm.

2.4 Monitoring echoes using passive acoustic mapping

Passive Acoustic Mapping was proposed by Gyongy in 2010 [160] to monitor bubble activity that can arise during HIFU therapy. By doing this, one can record passive acoustic signals originating from focus in a pre-defined region and create an intensity map. This helps in mapping acoustic activity that is generated by recording pressure fields generated by High Intensity Focused Ultrasound transducer. In order to acquire signals correctly, source strength must be calculated correctly. Newton's second law of motion states that the net force on a volume equals to acceleration times mass of the particles. This can provide us with an expression for the pressure fields relative to the particle velocity in the medium. If we neglect viscous stress, the linearized equation of momentum is expressed as:

$$\rho_0 \frac{\partial \boldsymbol{u}}{\partial t} = -\nabla p \quad \ldots \quad (2.22)$$

where ρ_0 is the density of the medium, $\boldsymbol{u}$ is the vector velocity field and p is the pressure field. Velocity consists of rotational and an irrotational part. Since the rotational part is independent of time, the velocity field is completely characterized by its irrotational part. This irrotational part is called 'velocity potential' Ø. Hence:

$$\boldsymbol{u} = \nabla \emptyset \quad \ldots \quad (2.23)$$

We can combine equations 2.22 and 2.23 to deduce an expression of induced excess pressure and the velocity potential:

$$p - p_0 = -\rho_0 \frac{\partial \emptyset}{\partial t} \quad \ldots \ (2.24)$$

A simple source that oscillates, the velocity potential is expressed as Ø = Ø(r, t) where r is the distance from the interested simple source and t is the time variable. Velocity potential is related to rate of volume flow $m(t)$ from the center of the source through:

$$\emptyset = -\frac{m(t)}{4\pi r} \ldots \quad (2.25)$$

If a sound wave has travelled a distance r, with a speed of sound c, the rate of volume outflow that has travelled the same distance as the sound can be written as:

$$\emptyset = -\frac{m\left(t - \frac{r}{c}\right)}{4\pi r} \ldots \quad (2.26)$$

Taking a derivative with respect to time will give:

$$\frac{\partial \emptyset}{\partial t} = -\frac{\dot{m}\left(t - \frac{r}{c}\right)}{4\pi r} \quad \ldots \ (2.27)$$

The rate of change of mass outflow for a simple source can be defined as

$$q = \rho_0 \dot{m}(t) \quad \ldots \ (2.28)$$

Combining equations 2.26, 2.27 and 2.28 gives us a relationship between source strength (rate of change of mass outflow from the source) and excess pressure as a result of source as strength:

$$p - p_0 = \frac{q\left(t - \frac{r}{c}\right)}{4\pi r} \quad \ldots \ (2.29)$$

Hence for source located at $\boldsymbol{r}$ with source strength q, resulting pressure at location $\boldsymbol{r}'$ at time t will be:

$$p(\boldsymbol{r}', t) = \frac{q\left(\boldsymbol{r}, t - \frac{|\boldsymbol{r} - \boldsymbol{r}'|}{c}\right)}{4\pi|\boldsymbol{r} - \boldsymbol{r}'|} \quad \ldots \qquad (2.30)$$

Equation 2.30 allows us to solve for the inverse problem of calculating source strength using pressure waves that are recorded by the sensors of ultrasound receive arrays in the presence of interfering signals. Equation 2.30 can be used to estimate source strength at positions of interest nu back-propagating signals received by the array to those position and coherently summing them. Hence, for position $\boldsymbol{r}$, source strength can be written as:

$$\tilde{q}(\boldsymbol{r}, t) = \frac{1}{N}\sum_{i=1}^{N} 4\pi|\boldsymbol{r_i} - \boldsymbol{r}|\tilde{p}\left(\boldsymbol{r_i}, t + \frac{|\boldsymbol{r_i} - \boldsymbol{r}|}{c}\right) \qquad (2.31)$$

where i is the index of element on the array, $\boldsymbol{r_i}$ is the location of the ith element of the array, $\tilde{p}$ is the pressure recorded on each elements of the array and c is the speed of sound in the medium. The steps to making correct

passive acoustic strength maps is as follows [167]:

Grid Definition – Defining the grid depends on the size of the HIFU focus. A 2-D area of interest is defined in front of the receive array and area is organized into different voxels. The choice of size of voxel depends on the size of resolution of the imaging array as well.

Recording the acoustic emissions – While performing HIFU treatment, acoustic emissions of linear and non-linear in nature are produced. The emissions can be recorded by receive elements of the receive transducer. The RF data available can then be used to create passive acoustic mapping.

Beamforming: Concept behind using beamforming uses signals recorded in the receive transducer and applying techniques to for image from it. Using equation 2.31, source strength at any location *r* can be constructed by back propagating the signal to location *r*. We can then coherently sum them for noise and interference rejection. Depending on the region of interest, we can delay the RF signal obtained on the receive transducer and time shift it accordingly. We can then sum signals over time and average it to reduce noise and suppress any interfering signals.

Estimating source energy – Source energy can be estimated using acoustic intensity. Source strength is directly related to acoustic intensity as follows:

$$I(\boldsymbol{r},t) = \frac{p^2(r,t)}{\rho_0 c} = \frac{q^2\left(\boldsymbol{r}', t - \frac{|\boldsymbol{r}-\boldsymbol{r}'|}{c}\right)}{(4\pi|r-r'|)^2\rho_0 c} \quad \ldots \quad (2.32)$$

where ρ_0 and c are the density and speed of sound of the medium respectively. Source energy, can then, be defined as:

$$\Psi(\boldsymbol{r}) = \int_{t_o}^{t_0+T} \frac{q^2\left(\boldsymbol{r}', t - \frac{|\boldsymbol{r}-\boldsymbol{r}'|}{\boldsymbol{c}}\right) dt}{4\pi\rho_0 c} \quad \ldots \quad (2.33)$$

2.4.1 Beamforming techniques for Passive Acoustic Mapping

Beamforming algorithms for image reconstruction are categorized into data-adaptive or non-adaptive algorithms based on how weights are applied to each element of receive transducer and how those weights are calculated. The choice of beamforming solely depends on the requirements of the system and there needs to be a compromise between spatial resolution and source energy estimation versus incurred computational cost and complexity of the algorithm. In section 2.4, I will discuss one non-adaptive algorithm (Time Exposure Acoustics)

and two data-adaptive algorithms (Capon Beamforming and Robust Capon Beamforming).

2.4.1.1 Time exposure Acoustics (TEA)

TEA was first introduced by Norton and Won [168] in 2003 as method to passively image underground scatterers created by ambient seismic noise. This method computes an intensity map in arbitrary units. It does so by calculating intensity of each pixel by using the following equation:

$$\bar{O}(r) = E\{|\sum_{i=1}^{N} \widehat{u_n}(r)|^2\} - E\{\sum_{i=1}^{N} |\widehat{u_n}(r)|^2\} \quad \dots \quad (2.34)$$

where $E\{\cdot\}$ denotes the statistical expectation operator, and $\widehat{u_n}(r)$ is defined as:

$$\widehat{u_n}(r) = 4\pi|r - r_n|\widehat{u_n}\left(r_n, \frac{|r - r_n|}{c}\right) \dots \quad (2.35)$$

$\widehat{u_n}(r_n, t)$ being the signal recorded by sensor placed at position r_n after being filtered. For PAM equation 21 can be written as [131], [160] :

$$I(\boldsymbol{r}) = \frac{1}{T}\int_{t_0}^{t_0+T} [(\sum_i H_i(\boldsymbol{r}, t))^2 - \sum_i H_i(\boldsymbol{r}, t)^2]dt \dots \quad (2.36)$$

where $H_i(\boldsymbol{r}, t) = \alpha\big(d_i(\boldsymbol{r})\big)p_i\left(t + \frac{d_i(r)}{c}\right)$ with $d_i(\boldsymbol{r})$ denoting the distance between the distance between the i^{th}array to desired point r in the grid, $p_i(t)$ denoting the pressure signal detected by the i^{th} element of the array at time *t* and $\alpha\big(d_i(\boldsymbol{r})\big)$ denoting the spatial sensitivity term. The second term in equation 2.34 aims at removing DC bias from image intensity. It does so by subtracting the variance of the received signals. Gyongy and Coussious [160]did not use this term as it lowers the intensity at estimated location. Hence the intensity map expression for PAM using TEA is reduced to as follows:

$$I(\boldsymbol{r}) = \frac{1}{T}\int_{t_0}^{t_0+T} (\sum_i H_i(\boldsymbol{r}, t))^2 \, dt \quad \dots \quad (2.37)$$

In cartesian coordinates it can be written as:

$$I(\boldsymbol{r}) = \frac{1}{T}\int_{t_0}^{t_0+T} (\sum_i H_i(\boldsymbol{x}, t))^2 \, dt \quad \dots \quad (2.38)$$

which is proportional to equation 2.36 in cartesian coordinates:

$$\Psi(\boldsymbol{r}) = \int_{t_o}^{t_0+T} \frac{q^2(\boldsymbol{x}',t)}{4\pi\rho_0 c}\, dt \ldots \quad (2.39)$$

where

$$\tilde{q}(x,t) = \sum_{i=1}^{N} w_i 4\pi d_i(x)\tilde{p_i}\left(t + \frac{d_i(x)}{c}\right) \ldots \quad (2.40)$$

The distance between any voxel at position $(x, y, z)$and sensor i at (x_i, y_i and z_i) is represented by $d_i(x) =$

$\sqrt{(x-x_i)^2 + (y-y_i)^2 + (z-z_i)^2}$ ... (2.41)

For TEA-PAM weights are predefined and are assigned as 1 for all elements. This makes TEA-PAM a non-adaptive beamformer. Lack of any data-adaptive beamforming can lead to signal artifacts and inaccuracies. A more common artifact called as tail-artifact is seen when using TEA-PAM in Fig 2.2. This happens due to presence of multiple bubbles interacting with each other in the desired region. This results in false activity beyond the actual source.

2.4.1.2 Data – Adaptive Beamformers

TEA-PAM algorithm introduces artifacts and limits spatial accuracy. This warranted an investigation into beamformers that can be weighted optimally to give a spatially accurate beam maps. The two data adaptive beamformers that will be discussed are Capon Beamforming[169] and Robust Capon Beamforming [162].

2.4.1.2.1 Capon Beamformer (CB)

CB or Minimum Variance Distortion less Response (MVDR) Beamformer was first introduced in 1969 [169] and it seeks to adapt the weights w by minimizing the variance of the array output. This allows the signal-of-interest to remain undisturbed. The optimization problem can then be, described as follows for signals that are pre-steered and amplitude compensated: $\boldsymbol{D(x)p(x,t)}$**,** and the steering vector corresponding to the direction of arrival (DOA) of the signal of interest to be equal to the unity vector ($a_0 = 1$) due to pre-steering:

$min_w \boldsymbol{w}^T \boldsymbol{D(x)R_p(x)D(x)w}$ subject to $\boldsymbol{w}^T a_0 = 1$.

The rationale behind the formulation of the above optimization problem is as follows. Assuming the array output at any point of time is:

$$r(t) = s(t)a_0 + \sum_i s_i(t)a_i + v(t) \ldots (2.42)$$

where $s(t)$ is the signal-of-interest arriving from DOA a_0, $s_i(t)$ is the ith interfering signal arriving from DOA a_i, and $v(t)$ is the noise of the system.

The output of the beamformer is:

$$y(t) = \boldsymbol{w^T} r(t) \ldots (2.43)$$

The goal is to choose the weights so that the desired signal $s(t)$ is preserved and the interfering signals and noise are suppressed. In case of CB, one performance measure is the output signal-to-interference-plus-noise ratio (SINR):

$$\text{SINR} = \frac{E\{|w^T s(t)a_0|^2\}}{E\{|w^T(\sum s_i(t)a_i + v(t))|^2\}} = \frac{\sigma_s^2 |w^T a_0|^2}{E\{|w^T(\sum s_i(t)a_i + v(t))|^2\}} = \frac{\sigma_s^2 |w^T a_0|^2}{\boldsymbol{w^T R_{i+v} w}} \ldots (2.44)$$

where $\sigma_s^2 = E\{|s(t)|^2\}$ is the power of signal-of-interest, and $\boldsymbol{R_{i+v}}$ is the covariance matrix of the interfering signals plus noise vector.

The ultimate goal of the beamformer is to maximize SINR while preserving the signal in the region of interest i.e $w^T a_0 = 1$. To achieve this, denominator needs to be minimized. Since the minimization of the variance of the array output with respect to the interferences and noise is not possible, because signals and their origin is unknown, following minimization of the variance of the output of the beamformer is proposed:

$$min_w E\{|y(t)|^2\} = min_w \boldsymbol{w^T R w} = min_w(\sigma_s^2 |w^T a_0|^2 + \boldsymbol{w^T R_{i+v} w})$$

$$= min_w(\boldsymbol{w^T R_{i+v} w})$$

where $R = \int_{t_0}^{t_0+T} r(t) r(t)^T dt$ is the covariance matrix of the array output vector.

The solution to this constrained optimization problem is found analytically using the method of Lagrange multipliers [161]:

$$w_{CB} = \frac{D(x)^{-1} R(x)_p^{-1} D(x)^{-1} a_0}{a_0^T D(x)^{-1} R_p(x)^{-1} D(x)^{-1} a_0}$$

The PAM energy map based on CB is calculated as follows:

$$\Psi(x) = \frac{4\pi}{\rho_0 c} \frac{1}{a_o^T D(x)^{-1} R_p(x)^{-1} D(x)^{-1} a_0} \quad \ldots (2.45)$$

Since we can calculate weights based on data, the spatial resolution of PAM will be improved, allowing better localization of sources of acoustic activity. However, in order to achieve optimized calculation of w_{CB} , the nominal steering vector a_0 must be accurately estimated. But this value, in CB, is fixed. Even a small array sensitivity might cause divergence of actual steering vector a_0. Such misalignment can lead to significant degradation of the PAM-CB performance, which in some case is even worse than the non-adaptive beamformer TEA [161].

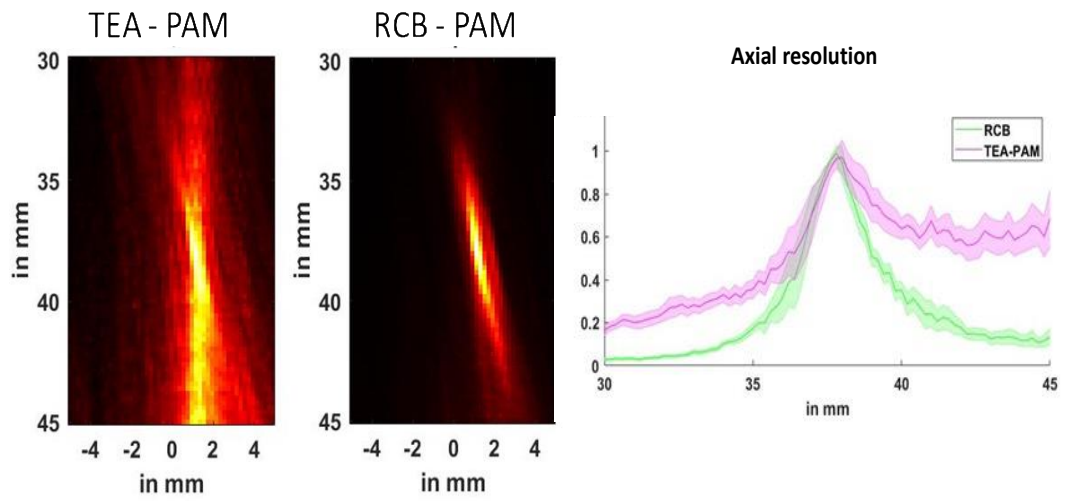

Figure 2.4: Comparison of TEA-PAM with RCB-PAM. TEA-PAM shows a tail-artifact after from 40-45mm. The data adaptive beamformers, RCB-PAM, can remove the "tail" artifact present in TEA-PAM and can help with improving axial resolution of the PAM.

2.4.1.2.2 Robust Capon Beamforming (RCB)

When ultrasound is used in clinical and experimental conditions, it is expected that array variabilities exist related to sensor's relative positions and gain. There may be varying speed of wave propagation in inhomogeneous media. Hence, adopting beamforming technique for PAM which can be flexible to such conditions is necessary. A natural extension of CB is Robust Capon Beamforming [161], [162]. It re-formulates the problem allowing the steering vector to vary within an ellipsoidal region and hence compensate for array imperfections.

Assuming a nominal steering vector $\bar{a} = 1$, we now need to estimate the actual steering vector a. This is the goal of our next optimization problem, which is formulated as:

$min_a \boldsymbol{a}^T(\boldsymbol{D}(\boldsymbol{x})\boldsymbol{R_p}(\boldsymbol{x})\boldsymbol{D}(\boldsymbol{x}))^{-1}\boldsymbol{a}$ **subject to** $||\boldsymbol{a}-\bar{\boldsymbol{a}}||^2 \leq \boldsymbol{\varepsilon}$

This constraint imposed here accounts for the region of uncertainty, where $\boldsymbol{a}$ can vary and $\boldsymbol{\varepsilon}$ is the parameter of uncertainty which allows the region to expand or shrink. The correct value for $\boldsymbol{\varepsilon}$ will depend on the experimental conditions and it usually involves a compromise between tolerance to steering vector mismatches and interference suppression capability.

To solve the steering vector of the signal-of-interest, we can use Lagrange multiplier methodology [162]:

$$\widehat{a_0} = \bar{a} - U(I + \lambda\Gamma)^{-1}U^*\bar{a}$$

Where the columns in **U** contain eigenvectors of $\boldsymbol{D}(\boldsymbol{x})\boldsymbol{R_p}(\boldsymbol{x})\boldsymbol{D}(\boldsymbol{x})$**,** the diagonal elements of Γ are the corresponding eigenvalues, and λ is the calculated Lagrange multiplier. The energy near the region of interest is calculated according to the following equation [170]:

$$\Psi(\mathrm{x}) = \frac{4\pi}{\rho_0 c}\frac{||\widehat{a_0}||^2}{N}\frac{1}{\bar{a}U\Gamma(\lambda^{-2}I + 2\lambda^{-1}\Gamma + \Gamma^2)^{-1}U^*\bar{a}} \quad \ldots (2.46)$$

RCB-PAM has been evaluated with microbubble imaging and it has significantly improved the localization of the recorded acoustic activity in Fig 2.4.

2.5 Summary

FUS, by itself, poses limitation that can prevent its widescale adoption. By incorporating acoustically active particles, we can enhance FUS therapy outcomes and make FUS more accessible. This chapter present methods which were used to create desired pressure field patterns to increase ablation efficiency in chapters 3 and to target precisely after registration in chapter 5. It is also important to accurately target FUS in the desired regions. Methods presented in this thesis use power Doppler imaging, which is capable of delineating brain vasculature, to target FUS transducer at a desired region in chapters 5 and 6. Finally, we present methods that can simultaneously record emissions generated from FUS interaction with acoustically active particles to inform us of regions undergoing cavitation in chapters 4 and 5. Overall, we present methods that can enhance FUS therapy outcomes all the while making it more accessible by combining FUS with acoustically active particles.

CHAPTER 3: Improving the Heating Efficiency of High Intensity Focused Ultrasound Ablation Through the Use of Phase Change Nanodroplets and Multi-focus Sonication[1]

3.1 Introduction:

Locoregional therapy, a process to directly treat a diseased region of the body, is performed with the goal of improving prognosis. While surgical removal is the most common locoregional procedure, there is a constant push to make these procedures less invasive, which helps reduce morbidity, cost, and the need for hospitalization [171] . There has been a significant innovation in the past decade to improve locoregional treatment of cancers of soft tissues, such as the liver and breast. Hepatocellular carcinoma (HCC) is one of the most common malignancies of the liver [172] [173], and although surgery is potentially curative treatment for HCC, it is contraindicated in cases where a single lesion <5cm in diameter exists or fewer than 3 lesions with diameters <3 cm [174]. In few cases where resection is not recommended and locoregional ablative therapies, such as radiofrequency ablation (RFA) or transcatheter arterial chemoembolization (TACE), are performed to prolong life and manage pain [97]–[101]. In the breast, researchers have explored alternative treatments like cryoablation [102] where they create an ice-ball near the tumor to engulf the tumor using argon based cryoprobe. Other ablation methods include radiofrequency ablation [104] and microwave ablation [105]. RFA and TACE, that are effective as a local ablative therapy, are invasive procedures, and an extracorporeal method that could achieve comparable outcomes would be desirable.

The work described in this chapter is part of first author publication: A. Singh, A. G. Nyankima, M. A. Phipps, V. Chaplin, P. A. Dayton, and C. F. Caskey, "Improving the heating efficiency of high intensity focused ultrasound ablation through the use of phase change nanodroplets and multifocus sonication," *Phys. Med. Biol.*, May 2020, doi: 10.1088/1361-6560/ab9559.

	Natural focus	2 foci	4 foci	5 mm diameter circle
Activation Power (in W)	100	200	200	100
Heating power (in W)	80	80	80	80
Total time of sonication (in s)	48	48	48	48
Total energy delivered (in J)	3840	3840	3840	3840
Number of observations	8	8	8	8

Table 3.1: Egg-white acrylamide phantoms with and without PSNDs were subjected to 4 different treatment options in the table above. There were in a total of 32 observations, 8 in each group where 4 observations in each group was carried out on phantoms with PSNDs and 4 observations were carried out on phantoms without PSNDs.

High Intensity Focused Ultrasound (HIFU) is being increasingly explored as an ablation option as it can focus sound waves of high pressures and intensity at an intended target to ablate non-invasively. In one clinical trial where researchers sought to treat liver and kidney tumors, [175], all liver tumors (100%) and a majority of kidney tumors (67%) were successfully ablated based on radiological or histological assessment after HIFU treatment. However, side effects in the form of skin toxicity and blisters in the region of ablation were observed. In a more recent hepatocellular carcinoma clinical trial by Zhang et al.,[176] researchers explored the efficacy of HIFU in causing necrosis while assessing its effects on adjacent blood vessels. The average tumor size in 39 patients (42 tumors in total) undergoing ablation was of 7.4±4.3 cm in its greatest dimension. At power levels of 160-250W at 0.8 MHz, the researchers were able to ablate 21/42 completed with rest more than 50% ablated. The side effects of the treatment included mild local pain and mild skin burn. One patient had skin blisters and another patient had skin burns and blisters. Similar results were in a primary and metastatic liver tumor trial by Leslie et al., [177] where researchers treated 31 patients with HIFU. 39% of patients suffered with superficial skin burns and one patient suffered with moderate skin burn. Similar outcomes are also seen when HIFU is used for breast cancer ablation in clinical trials [9], [11], [12], [66]. Some of these clinical trials reported an ablation volume of around $8cm^3$ at power levels between 80-271 W for 35-133 minutes but ablation came at a cost of off-target heating.

Hence, despite the promise of HIFU technology for non-surgical ablation, off-target heating remains a major concern. The ability to reduce off-target heating while maintaining HIFU's ability to provide non-invasive volumetric ablation would increase HIFU's adoption for soft tissue ablation procedures.

One approach to improving heating is to use acoustically active particles that can accelerate heating due to ultrasound absorption. Microbubbles is one such acoustically active particle than can increase volumetric ablation

[107] and subsequently decrease therapy duration[178]. Microbubble oscillations induce local heating through viscous losses in the surrounding medium [179], produce local shock waves, which can aid in tissue ablation and cause mechanical stress at cellular level. In literature, researchers have used Levovist, a clinically approved contrast agent, to accelerated heating, [180], [181]. In one study specifically [182], researchers reported nearly a double volumetric ablation in rabbit liver which was injected with 7mL of Levovist (371±104 mm^3) vs rabbit liver that was only injected with saline (166±71 mm^3). However, the use of microbubbles in a clinical setting to aid tumor ablation tend to induce off-target heating, primarily in the near field [107]. This is because microbubbles amplify thermal energy deposition regardless of their location. Moreover, not only do microbubbles have a short circulation half-life [72], high concentrations of microbubbles can attenuate acoustic penetration into deeper tissues. Furthermore, microbubbles are too large extravasate from the vascular space, and remain localized within blood vessels, [70], [71].

Prior data suggests that phase-shift nanodroplets (PSNDs) might serve as an improved alternative agent to microbubbles for enhancing HIFU thermal deposition. PSNDs, which are nanometer-sized liquid particles, can undergo phase shift and convert to microbubbles when sonicated above a threshold pressure. This threshold pressure can be tailored depending on the PSND composition [108]. Because PSNDs only convert to microbubbles in regions of the pressure field above a threshold, they amplify heat only in the focal region, thereby mitigating or reducing any off-target heating. Moyer et al. observed a temperature rise of 130% and an ablation volume 30 times greater with PSNDs vs without PSNDs in the rat liver [111] in response to HIFU treatment. Finally, the stability and circulation time of certain PSND formulations were found to be substantially longer than that of microbubbles [106]. PSNDs in combination with HIFU can overcome challenges of volumetric ablation efficiency posed on to use due to small focal region of HIFU's ellipsoidal focus which is on the order of 1-3mm. Clinical systems typically steer a single focus in a circular or spiral pattern to generate a larger focal volume with larger spirals resulting in increased overall heating efficiency[24], [183]. Another approach to improve heating is to use multi-focal heating pattern. Multi-focal heating patterns avoid high intensity levels that can develop due to high focal intensity levels when treating large tumors using 'point by point sonication' method. Ebbini et al [164] showed that by using multi-focus treatment approach, one can precisely control the intensity levels at each of the control points in the treatment volume. This is especially useful for mild hyperthermia setting where using multiple concurrent foci can provide the benefit of reducing acoustic pressure near the focal region and providing better control over treatment volume [184], [185]. In one study [184] researchers showed that multi-focus ablation resulted in a significant reduction

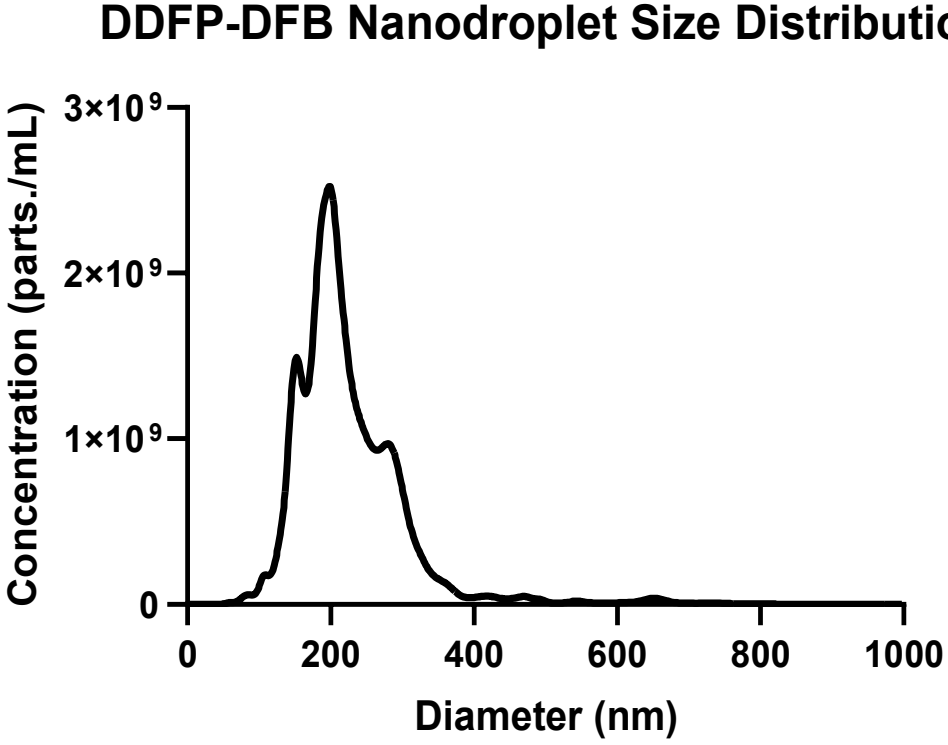

Figure 3.1: DDFP-DFB nanodroplet size distribution. Majority of nanodroplets were 200nm in diameter.

(67%) in peak acoustic pressures in simulation and hydrophone measurements as compared to single focus. While multi-focal heating provides better spatial coverage, it can lower overall energy efficiency of the region and can contribute to concentrate pre-focal heating. PSNDs pair well with multi-focal heating methods because they amplify thermal effects only in the focal region, keeping off-target regions safe. In this study, we explored how pairing beam focusing patterns with PSNDs increased volumetric ablation and improved ablation efficiency.

Our overall goal was to increase the volumetric ablation while reducing the total energy delivered. We examined thermal effects of PSNDs on the lesion size in phantoms during HIFU ablation using magnetic resonance (MR) thermometry in 7T MRI. Using the temperatures obtained via MR Thermometry, the values of volumetric ablation that reached CEM 240 at 43ºC, i.e the lethal thermal dose was calculated [24]. Lastly, values for ablation efficiency (mm^3/J) was calculated, and was compared across all the cases with and without PSNDs.

3.2 Materials and Methods

3.2.1 Lipid Solution

The procedure to create nanodroplets (PSNDs) was originally published in Moyer et al.[110] . Briefly, two lipids were combined in a 1:9 ratio (both from Avanti Polar Lipids, Alabaster, AL, USA) to create the shell of the PSNDs: 1, 2-distearoyl-sn-glycero-3-phosphoethanolamine-N-methoxy (polyethylene-glycol)-2000 (DSPE-PEG), and 1, 2-distearoyl-sn-glycero-3-phosphocholine (DSPC), respectively. Lipids were emulsified in an 1.0 mg/mL aqueous solution of 15% (w/v) propylene glycol, 5% (w/v) glycerol, and 80% (w/v) phosphate-buffered saline (PBS). Once prepared, the lipid solution was portioned into 1.5mL aliquots and stored in 3mL glass vials. Vials are sealed and stored at 4ºC.

3.2.2 Nanodroplet Protocol and Size Distribution

When ready for use, lipid solutions were removed from storage, and the headspace of the vial was replaced with desired perfluorocarbon (PFC) gas. In this study, a 1:1 mixture of dodecafluoropentane (DDFP, C_5F_{12}, boiling temperature= 28ºC), and decafluorobutane (DFB, C_4F_{10}, boiling temperature= -2ºC). The PFC mixture was obtained by filling a syringe with 60mL of DFB (Fluoromed, Round Rock, TX, USA), which was contained in a gas canister set to 6 psi. The syringe was placed in a -20ºC freezer, and the DFB was condensed to a liquid. Liquid DFB was mixed with 0.5mL of DDFP (Exfluor Research Corporation, Round Rock, TX, USA), and the liquid solution was vaporized back into a gas. The DDFP-DFB gas mixture was then connected to the lipid solution vials and filled the vacuumed headspace. The PFC containing lipid solution was shaken into a microbubble solution for 45 sec (VIALMIX® Shaker, Lantheus Medical Imaging, N. Billerica, MA, USA). The vials were placed in a -11ºC ethanol-water bath for 2 min, and then, 14 psi of nitrogen gas was pumped into the headspace to pressurize the microbubbles into PSNDs. The vials continued to be swirled in the cold bath for 30 sec, before the nitrogen line was removed, and vials were placed on dry ice for shipping. The vials of PSNDs were shipped overnight to Vanderbilt University on dry ice.

Size distributions of the PSNDs were collected using a NanoSight NS500 (Malvern Instruments, Westborough, MA, USA). A 2:998 dilution of the PSNDs was used to characterize the particles, by adding 2 µL of stock PSNDs to 998 µL of 20nm-filtered HPLC-grade water. In **Figure 3.1**, a total of 3 vials was measured to create the size distribution presented.

3.2.3 Tissue-mimicking phantoms

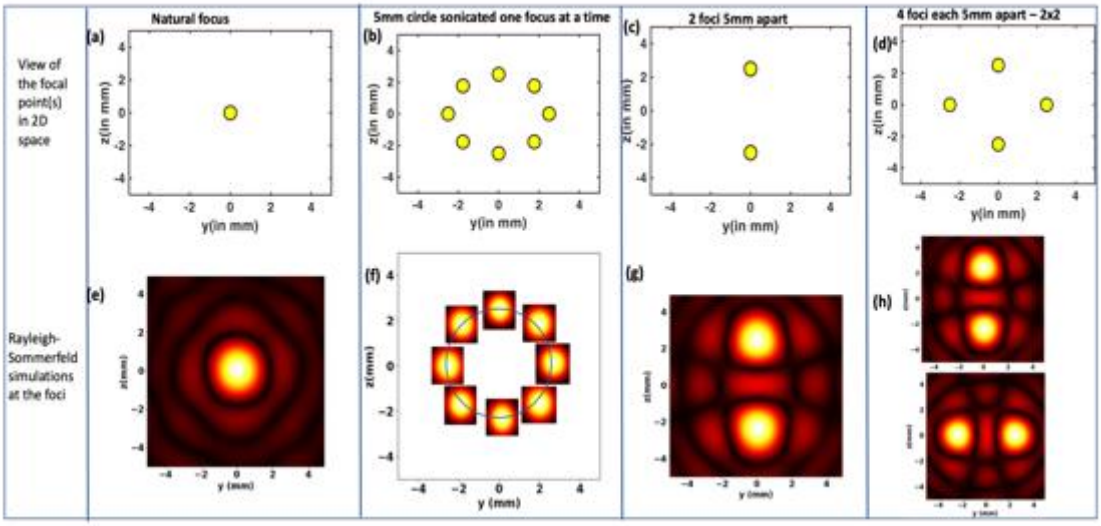

Figure 3.2: Different ablation patterns. The top row presents how the focal points look in 2D space. The bottom row presents the Rayleigh Sommerfeld pressure simulation at those foci. Following are the specific cases:(a) & (e) Case 1 where the activation and heating happened at the natural focus.(b) and (f) Case 2 where activation and ablation happened point wise on an 8-points 5mm diameter circle. Each of the 8 points were first activated and was followed by heating. (c) and (g) Case 3 where two points were activated at the same time and followed by heating. Heating at both points took place at the same time. (d) and (h) Case 4 where 4 foci was activated and heated. In this particular case 1st 2 foci were activated and then heated. Once activation and heating of 1st 2 foci was done, same happened to 2nd 2 foci.

The process to make acrylamide-albumin tissue mimicking phantoms have been described previously [186]. These phantoms were created from an 8:7:5 mixture of aqueous acrylamide (bis-acrylamide to acrylamide ratio of 1:29), liquid egg-white, and deionized water, respectively. When these phantoms are heated to 60˚C or above, the egg whites start to permanently denature and create an opaque lesion whereas at temperatures below 60˚C, they are nearly transparent. The acoustic properties of these phantoms are very close to that of the tissue and make it a very desirable *in-vitro* phantom. These phantoms are polymerized with nanodroplets at concentration 0.8ul/1ml of phantom material. The nanodroplets were dispersed to acrylamide solution before polymerization via the addition of 0.5% vol/vol of 10% ammonium persulfate and 0.2% vol/vol of tetramethylethylenediamine. This solution was then poured into a cylindrical mold of 40mL and was used within 24 hours of their polymerization.

3.2.4 High intensity Focused Ultrasound

HIFU was delivered using a randomized spherically focused, 128 elements, phased array driven at 650 kHz (Image-Guided Therapy, France) with the radius of curvature and opening diameter is 7.2 cm and 10.3 cm

respectively [187]. A continuous wave HIFU at an average power of 80W was applied to ablate phantoms. Pressures at each power level at natural focus until was calibrated via a needle hydroplane (ONDA HNA-0400, Sunnyvale, CA) in a degassed deionized water bath until 2.2W. These values were subsequently used for extrapolation for pressures at higher powers. Extrapolation of values using needle hydrophone showed a PNP of 4.2 MPa at desired powers. The experimental set up resembled Figure 3.3. Different cases of activation and heating are presented in Figure 3.2 and elaborated more in section below. An initial burst of 20 pulses, each with duration of 0.09s, were used for PSND activation. This was done to ensure that all particles in the region were activated prior to heating pulses. The power for initial burst varied as follows: a) for single focus, 1 burst was applied with 100W power; b) for 2 foci a single multi-focal burst was transmitted at 200 W; c) for 4 foci ablation two multifocal bursts at 200 W were applied to activate 4 foci, and d) for the 5-mm diameter circle, 8 bursts at 100 W were used to activate each of the 8 points. Based on our extrapolated hydrophone estimates, these bursts ensured that each focal point in single or multi-focal cases received a focal pressure and duration known to convert particles (PNP 4.2MPa - 4.4 MPa, PPP 4.5MPa-4.6MPa), confirmed by B-mode images (Figure 3.4). After the nanodroplets were converted, heating pulse at 80W was applied for a total of 48s.

3.2.5 Groups of phantoms for treatment

The prepared egg-white acrylamide phantoms were distributed in different groups. The groups consisted of phantoms that would undergo one of the following treatments presented in **Table 3.1**. A total of 32 experiments were done where a total energy of 3840 J was delivered in each case with an average power of 80 W. All phantoms were heated for 48 seconds with a near 100% duty cycle. Multiple foci, in figure 3.2, was generated using method described by Ebbini et al [147] using our 128 random phased array spherical cap[187] and is described in detail below. The top row in figure 3.2 show a 2D representation of multi-focus whereas bottom row represents the pressure map for those multi-focus points. The case 3.2 is similar to how single focus sweep sonications were done in prior studies [184].

3.2.6 Generation of Multiple foci

Single focus sonications were performed at the transducer's natural focus. In order to generate multiple foci, methods outlined in previous works have been implemented [147]. IN this section, derivation of above mentioned method is covered. The complex pressure at a point in acoustic field can be represented by:

$$p(r) = \frac{j\rho ck}{2\pi}\int_{S'} u(r')\frac{e^{(-jk|r-r'|)}}{|r-r'|}dS' \ldots (1)$$

where $j = \sqrt{-1}$, ρ is the density, c is the speed of sound, k is the wavenumber, S' is the surface of the source, u is the normal velocity of the source surface, and r and r' are the observation and source points, respectively.

If a phased array transducer that has N number of elements. Pressure at M control points at position $r = r_m$ where $m = 1,2, \ldots M$ can be written as

$$p(r_m) = \frac{j\rho ck}{2\pi}\sum_{n=1}^{N} u_n \int_{S'} \frac{e^{(-jk|r_m-r_n'|)}}{|r_m-r_n'|}dS' \ldots (2)$$

If we let

$$H(m,n) = \frac{j\rho ck}{2\pi}\sum_{n=1}^{N} \int_{S'} \frac{e^{(-jk|r_m-r_n'|)}}{|r_m-r_n'|}dS' \ldots (3)$$

then we can represent equation 1 in matrix form where:

$$Hu = p \ldots (4)$$

where $u = [u_1, u_2, \ldots u_N]^t$ and $p = [p(r_1), p(r_2), \ldots p(r_M)]^t$

One can use equation 4 can help solve for amplitude and phase of N transducer elements that can generate desired pressure at M control points. When $M<N$, H has full rank and minimum-norm solution of the matrix in equation iv can be solved by:

$$\hat{u} = H^{*t}(HH^{*t})^{-1}p$$

where H^{*t} is the conjugate transpose of H.

The multiple foci patterns used in study were influenced by the frequency (650 kHz) and the focal size of our transducer (full width half maximum was 9.3mm and 2.2mm in the axial and lateral directions), and pressure threshold for PSNDs conversion [187]. We sought to perform patterns that closely match the studies performed by transducers at frequencies of 1.2 MHz with focal spot size of 1 x 1 x 8 mm^3 [184], [188]. The 5-mm diameter circle is comparable to ablation cell sizes used in clinical systems like Sonalleve [183], [188]. The choice of having points 5mm away from each other ensured that points did not overlap and at the same time generated enough pressures to

convert PSNDs to MBs.

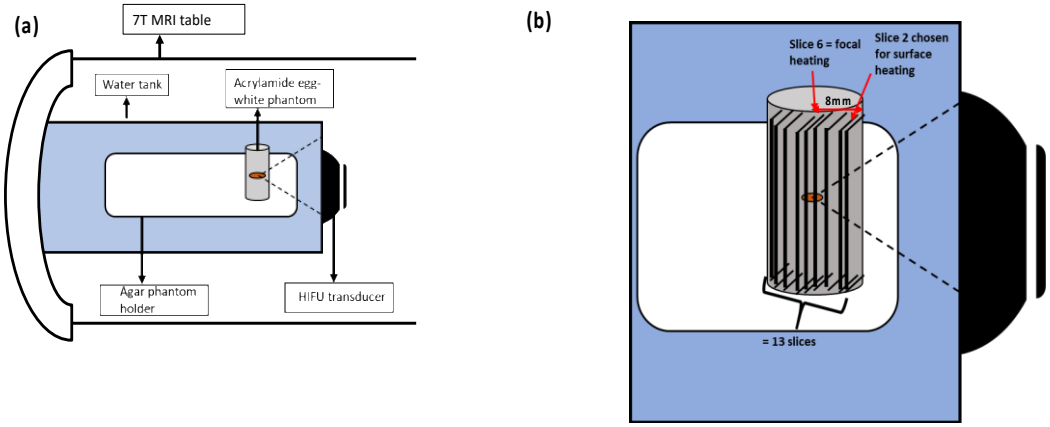

Figure 3.3: MRgFUS setup for ablation. (a) This figure is of side view of our experimental set up which consists of water bath and 5% agar phantom holder in that water bath. This agar phantom holder has a slot for our egg-white acrylamide phantom. The transducer is attached to the water bath and the agar phantom holder and egg white phantom is placed right in front of the transducer at a distance where the beam from the transducer converges to form the focus (red ellipse). This set up of transducer, water bath and our phantoms is then moved into the 7T MR bore encased in single channel NOVA coil. (b) A zoomed in representation of total number of slices that were acquired in our phantom and how the focus aligned with the slices. Each slice was evenly spaced apart by 2mm. Additionally, it shows location of slice that was chosen as to evaluate surface heating with respect to slice that saw most heating and was chosen as slice for focal heating. Slice 2 was 8mm away from the focus. It was important to choose slice inside the phantom for surface heating in order to provide accurate measurements of heating for conditions that use PSNDs.

3.2.7 Recording of Onset of Vaporization

The onset of vaporization followed by heating induced by these nanodroplets was visualized using an e17-4 probe of Phillips EPIQ7 ultrasound scanner machine in their contrast mode. The contrast mode enables identification of regions that give out signals at higher harmonics, and consequently help identify existing microbubbles in the image. The image obtained from the scanner was in a DICOM format and was processed in MATLAB R2018a.

3.2.8 MR-Thermometry

MR thermometry was employed to measure the volume of heat deposition and maximum rise in temperature. MRI was performed using human Philips Achieva 7 Tesla MRI (Best, Netherlands) using a NOVA

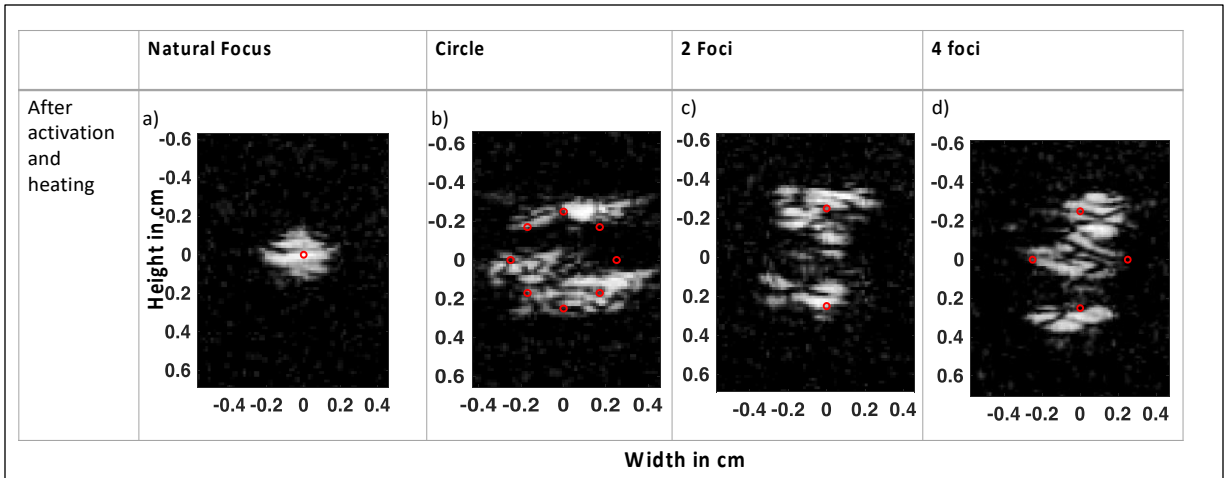

Figure 3.4: Contrast images acquired using imaging US after activating and heating phantoms. The red dots represent location of the focus in each case. Contrast imaging helps in identification of microbubbles in a medium as they give signals out at higher harmonics. We used this imaging technique to ensure conversion of our nanodroplets to microbubbles. (a) Contrast imaging obtained after activating and heating natural focus located at (0,0) in the image. (b) Contrast image obtained after activating and heating 8 point 5mm diameter circle. 7 out of 8 points saw heating in this case. (c) Contrast image obtained after activating and heating 2 points 5mm away from each other. Both points saw activation and heating. (d) Contrast image obtained after activating and heating 4 points – 2 points 5mm apart were heated and activated at a time. Once first 2 points were activated and heated, next 2 points went through the same regime. In this particular case, 3 out of 4 points saw activation and heating.

Medical (Wilmington, MA, USA) birdcage for both transmit and receive. Sonications were performed inside the scanner using our MR-compatible HIFU device. Albumin-acrylamide gel phantoms were insonated using continuous wave HIFU at 650 kHz. The first pulse was the activation pulse at 100 W for single focus and at 200 W for multi-focus. After the first pulse, the phantoms were heated at lower power to deliver a total energy of 3840 J in a span of 48 seconds. The average power was consistent across phantoms with standard deviation of ± 3%. Temperature rise and volumetric heating was monitored using 3D sagittal slices that were 2mm apart. All images were acquired using 2D multi-slice spoiled gradient echo with following parameters

TE (echo time) = 10ms

TR (repetition time) = 25 ms

Field of view = 120mm x 26mm x 120mm

In plane resolution – 2mm x 2mm

Flip angle = 10 degrees

Slice thickness – 2mm

Scan time – 120 seconds

For each application of ultrasound sonication, a total of 13 slices were acquired. Sonication was started 21 seconds into imaging and the heating continued for next 48 seconds. The total scan time was 2 minutes. Temperature maps were reconstructed using MR images by employing proton resonance frequency shift method[89], [189]. The temperature change was calculated by computing the phase difference between baseline images and images that proceeded right after heating was on assuming α = 0.01ppm/°C and field strength of 7T. The thermometry and imaging plane are presented in **Figure 3.3**. The data acquired from 7T MRI was processed off-line in MATLAB R2018a. The heating pixels were unwrapped using phaseUnwrap2D algorithm[190]. After unwrapping, the temperature rise in each slice was calculated using the phase difference in the images. The maximum ΔT observed in focus of each phantom with PSND and the maximum ΔT observed at the surface of that phantom was then calculated to quantify focal and pre-focal heating. This pre-focal heating slice was 8mm away from the focus proximal to the transducer. After evaluating the rise in temperature, volume that reached 240 cumulative number of equivalent minutes at 43 °C (240 CEM 43 °C) was calculated by setting the base temperature to 37 °C. The CEM 43 °C was calculated using the formula:

$$CEM_{43} = \sum_{i=1}^{N} [R_{CEM}]^{(43-T_i)} t_i \quad \ldots (5)$$

where t_i is the *i*-th time interval, *R* is related to the temperature dependence of the rate of cell death ($R(T< 43$ °C)=1/4, $R(T>43$ °C)=1/2) and T_i is the average temperature during time interval t_i. CEM_{43} values were used for creating isosurfaces (**figure 3.6(c)**) for volumes greater than 240 CEM 43 °C to study the shape of lesion formed.

3.3 Results

3.3.1 Nanodroplet Size Distribution

We found that the NDs formulated with a DDFP-DFB core had an average mean diameter ± standard deviation of 219 ± 67 nm (N=3). The average concentration for the size distribution was $2.9x10^{11}$ ± $6.3x10^{10}$.

3.3.2 B-Mode contrast image of phantoms with PSNDs:

The results of our B-Mode imaging confirm that phantoms with nanodroplets undergo phase transition at 4.4 MPa followed by heating pulse power matched at 80W (Figure 3.4). The size of focal zone after the treatment at the natural focus is consistent with lateral width of the beam at focus, which is ~2mm (Figure 3.4(a)). In the case of circle (Figure 3.4(b)), activation can be seen 6 out of 8 of the desired points. Similarly, in the cases of 2 foci (Figure 3.4(c)) and 4 foci (Figure 3.4(d)) activation can be seen at intended locations.

3.3.3 On target vs Off target heating

In order to quantify on target vs off target heating, we processed our acquired MR thermometry images that informed us of the rise in temperature at the focus (focal heating) and rise in the temperature at pre-focal surface of the phantom (surface heating). The maximum rise in temperature at the desired focal regions **(Figure 3.5(a))** in

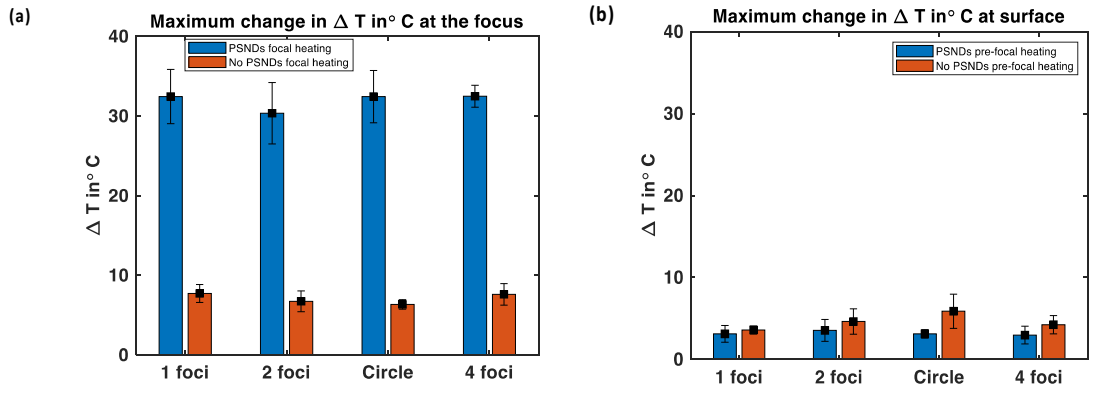

Figure 3.5: Change in temperature during HIFU. **(a)** Graph that shows maximum rise in temperature at the focus and **(b)** at the surface. The surface was 8mm away from the slice that saw the most heating. The values in this graph is comparable across all 4 cases. 4 foci saw the greatest focal heating, only slightly better (0.04°C greater) than 2 foci heating. But 2 foci performed the best when the maximum rise in surface heating was seen. It showed the lowest surface heating of 3.123 °C

phantoms bearing PSNDs is comparable across cases where a rise of 32.5 °C, 30.4 °C, 32.5°C, and 32.5 °C was seen in single focus, circular pattern, 2 foci and 4 foci cases respectively. The maximum temperature rise at the surface was 3.1 °C, 3.5 °C, 3.1 °C, and 3.0 °C for single focus, circular pattern, 2 foci and 4 foci cases respectively as seen in **Figure 3.5(b**).

Phantoms without PSNDs all experienced less heating overall. Maximum temperatures rose to only 7.7°C, 6.8°C, 6.4°C, 7.6°C in single focus, circular pattern, 2 foci and 4 foci cases respectively **(Figure 3.5(a)).** The maximum temperature rise at the surface was 3.4 °C, 4.6 °C, 5.9°C, and 4.2 °C for single focus, circular pattern, 2 foci and 4 foci cases respectively **(Figure 3.5 (b)).**

3.3.4 Volumetric ablation calculation

After obtaining the change in temperature values and adding 37 °C to those temperature values, values of 240 CEM 43 °C were calculated using equation 5. Any voxel that had reached a value greater than 240 CEM 43 °C was used to evaluate the final volumetric ablation **(Figure 3.6(a))**. The volumetric ablation achieved by 2 foci and 4 foci were consistent and greater than volumetric ablation achieved by single focus and circle pattern as shown by

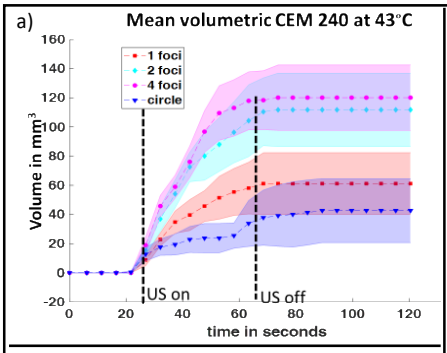

b)

Case	Average volumetric ablation(mm³)
Single	61.1431±24.4
Circle	42.665±25.3
2 foci	111.73±29.0
4 foci	120.18±25.8

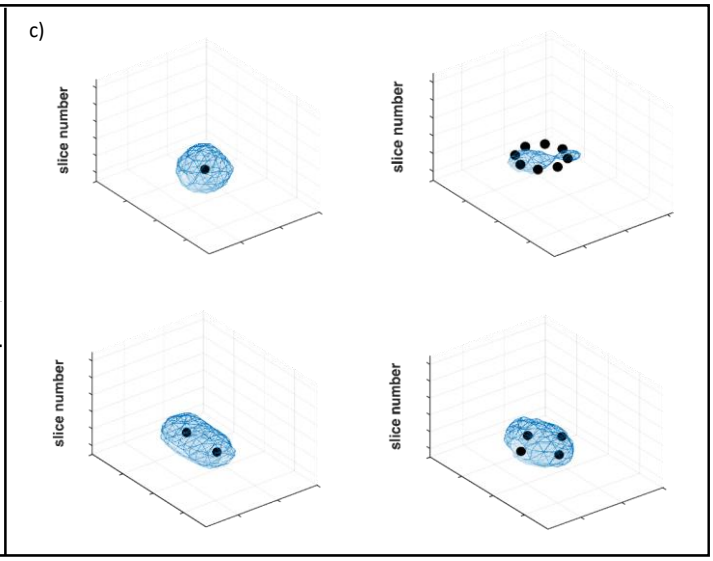

Figure 3.6: Mean volumetric ablation in cases with phantoms with PSNDs. **(a)** This graph represents the mean volume that reached at least 240 CEM 43 °C in phantoms with PSNDs. This was calculated by calculating the temperature in CEM 43 and thresholding all voxels in MR Thermometry slices that were greater than 240 CEM 43 °C. **(b)** Tabulated form of mean volume in each case. **c)** These images represent isosurface of volumetric ablation. It gives the spatial distribution of the ablated volume and shows single, 2 foci and 4 foci had contiguous lesions but circle does not. This is only for one phantom with PSNDs in each case but this scenario was also true for other phantoms with PSNDs in all cases.

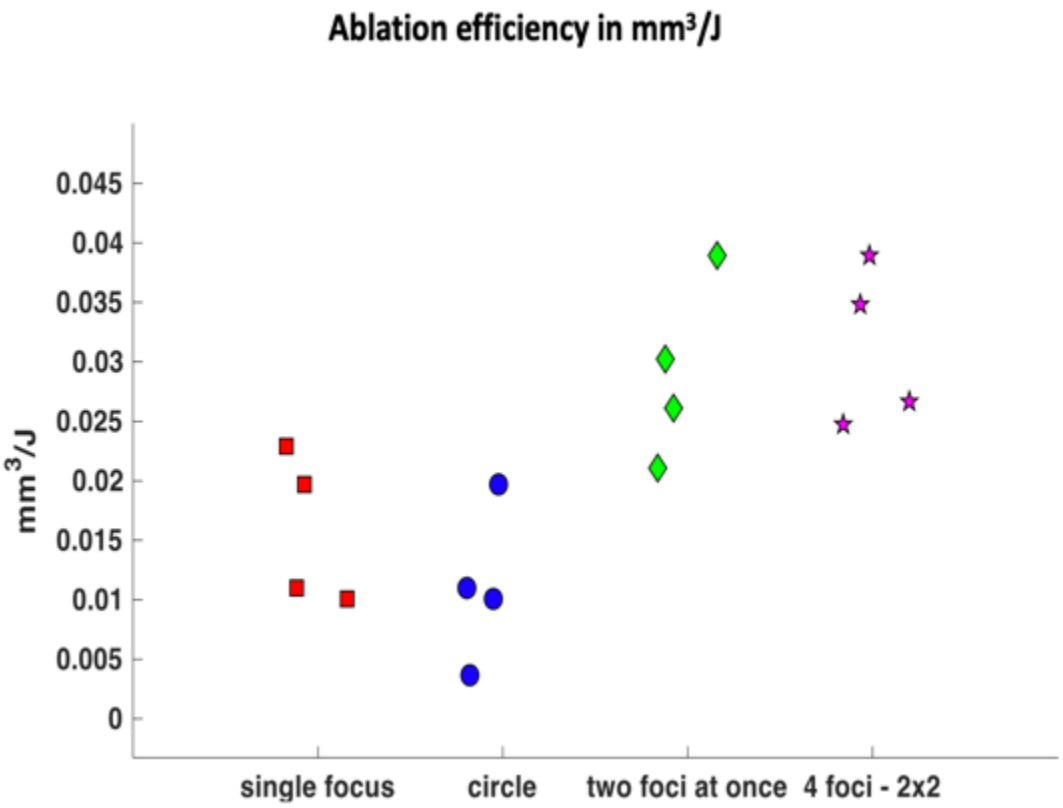

Figure 3.7: Graph representing maximum ablation efficiency. This was calculated by dividing ablation volume that reached greater than 240 CEM 43 °C with the total energy deposited to each phantom. Value for each case is presented here. Multi-foci performed the best here.

the rate of change of mean volumetric ablation **(Figure 3.6(a))**. The average volumetric ablation increased during the focused ultrasound on period in all heated phantoms with PSNDs (**Figure 3.6(a)**). Representative volumetric isosurfaces of voxels with temperature rises greater than 240 CEM 43°C show how 4 foci, 2 foci and single focus develop contiguous lesions, while circular foci often had gaps between foci (Figure 3.6(c)). Statistical analysis revealed that there was a significant difference ($p < 0.05$) between volumetric ablation of single focus and 4 foci based on two-sided Wilcoxon rank sum test; however, there was no significant difference between volumetric ablation of circle and single focus ($p > 0.05$) and between single focus and 2 foci ($p = 0.0571$). There was no significant difference observed between two multi-focus cases; however, there was a significant difference in volumetric ablation between multi focus (both 2 foci and 4 foci) and ablation in circle pattern ($p < 0.05$). Figure 3.6(b) shows mean 240 CEM at 43°C over 120 seconds where 4 foci performed the best and circle performed the poorest.

3.3.5 Evaluating ablation efficiency

After obtaining the volumetric ablation in all cases, values for ablation efficiency was calculated **(Figure 3.7)** where the volumetric ablation (in mm^3) in each case was divided by the total energy put in (in J). Again, 2 foci and 4 foci saw the greatest ablation efficiency values of up to 0.04 mm^3/J for each. Single foci and circle patterned foci saw maximum ablation efficiencies of 0.023 mm^3/J and 0.02mm^3/J respectively.

3.4 Discussion

We used HIFU in conjunction with PSNDs to improve the efficiency of HIFU thermal ablation. We developed a method where increased volumetric ablation for a fixed amount of energy could be delivered and tested it on phantoms with acoustic properties similar to tissues. We show an increased volumetric efficiency when combining multi-focal sonications and PSNDs while a decreased off-target heating, overcoming two of main challenges facing thermally ablative HIFU procedures.

3.4.1 Heating restricted to focal region with PSNDs

Phase shift nanodroplets were activated in the shape of chosen beam patterns. The heating was contained within the desired regions and no off-target regions show any ablation in **Figure 3.6(c)**. The natural focus activation pattern spans the 2-mm lateral beam width of the focus, while multi-focal and circularly steered cases have activation patterns that span the expected ranges (**Figure 3.6(c)**). Our sonication procedure resulted in a mean rise of only 6°C at the surface of the phantom implying that ablation using PSNDs only results in on-target heating. In the absence of PSNDs, the maximum focal heating observed was less than 7°C compared to >30°C in the presence of PSNDs. Similar to prior studies, heating was restricted only to the focal region with very little heating occurring at the surface (**Figure 3.5 (b)**)[110].

3.4.2 Increased volumetric ablation and ablation efficiencies observed in MF-PSND when compared with SF PSNDs at matched power levels.

Multi-focus heating at a constant energy and power generated an increased volumetric ablation when compared to single focus ablation at transducer's natural focus. The volume reaching CEM43 of 240 based on MR thermometry observed in multi-focus case was twice as large when compared to natural focus or circularly steered (**Figure 3.6**). Four foci ablation achieved the highest volume of 120.2±25.8 mm^3 which was followed by 2 foci

ablation which achieved a thermal ablation volume of 111.7±29.03 mm^3, all at constant power 80W.

3.4.3 Heated volumes observed in MF-PSND were contiguous when compared to single focus circle case.

Heating was observed to be more contiguous for multi-focus cases with no gaps present in between the multiple foci as demonstrated in **Figure 3.6(c)** whereas the sequentially scanned circular pattern showed gaps that did not reach CEM43 of 240 after sonications. The lack of contiguous lesions in circular pattern could be due to shorter duration of heating pulses per focus. For the case of ablation performed in the circle, each point on the circle was heated only for 6 seconds vs 48 seconds in other cases. Hence, longer duration of heating pulses may have caused diffusion of heat between adjacent nanoparticles, thereby causing them to convert as heating can also aide in phase shifting the nanodroplets [191]. Maximum observed efficiency of 0.04 mm^3/J in 2 foci and 4 foci ablation was almost twice of what was observed in single focus case. When these results were compared with 4mm circular trajectory HIFU ablation performed in clinical trials by Kim et al, they had an ablation efficiency of 0.06±0.12 mm^3/J which was higher than the ablation efficiency observed in our study. While the higher ablation efficiency in their study could be attributed to the 1.2 MHz center frequency, further analysis that includes frequency dependent attenuation between the transducer face and target would be required to quantitatively compare our PSND study to the *in vivo* study.

3.5 Study Limitations

Some limitations should be considered when interpreting our study results. Our study was aimed at improving ablation efficiency at constant power. This was achieved by combining multi-focus sonication sequences with PSNDs. These sonication patterns were chosen to closely match patterns in previous clinical trials but would likely benefit from optimization via simulation. Rayleigh-Sommerfeld integral simulations in conjunction with bioheat equation during electronic steering may result in a better treatment plan [192]–[195] as it give us pressure fields and heat deposition estimation at those pressure fields. To facilitate matched comparisons we did not implement any feedback control in our study, but feedback control could likely be optimized with the methods presented in prior studies [24], [196], [197]. Our finding that multifocal HIFU coupled with nanodroplets has increased volumetric ablation efficiency is general and should be function synergistically with prior optimizations. Volumetric ablation at lower powers than those currently used in clinical trials could benefit many therapeutic

ultrasound procedures, leading to decreased time when treating large regions and an increased safety margins due to the lower energy required.

3.6 Conclusion

This study successfully showed that PSNDs and multi-focus sonication can be used in conjunction to increase focal ablation volume while avoiding any off-target heating when compared to performing volumetric ablation at single focus. This approach could substantially improve the clinical translatability of HIFU ablation by reducing treatment time and reducing side effects.

CHAPTER 4: Using passively detected acoustic signals to characterize ultrasound gated nanoparticles[2]

4.1 Introduction

Modulating neurons in the brain is desirable for many treatment options like Parkinson's and essential tremor [35], [37]. Deep brain stimulation is one widely used neuromodulation technique for treating Parkinson's and OCD but its invasive and carries many side-effects[198]. Focused ultrasound (FUS) is another method which can cause neuromodulation non-invasively in a spatially selective regions [20]. Although the natural response of neurons to ultrasound has been explored, combining FUS with an acoustically active drug loaded nanoparticles have the benefit of yielding a pharmacological response that may be more predictable than the effects of FUS alone. FUS coupled with acoustically active drugs can modulate neural activity in a more controlled way in one of the two ways: 1) by opening blood brain barrier [23], or 2) by delivering drugs via nanoparticles that do not need opening of blood brain barrier(BBB) [22], [60]. In this study, we explored activity of nanoparticles (NPs) that release propofol upon FUS application and. These NPs can cause neuromodulation by allowing the uncaged propofol to cross the BBB without opening it. In-vitro, researchers showed that these NPs release propofol from nanoparticles starting at an MI of 1, and this release increased with an increase in MI. An increased release of propofol is desirable to elicit a stronger neuromodulatory effect. However, higher pressures have been associated with unwanted bioeffects due to cavitation which manifest in form of wideband signal [199]. In this study, we explored echoes originating from sonication of propofol-bearing nanoparticles at pressures that enhance the release of propofol using a single element receive transducer and mapped these echoes [148], [160].

---

2. The work described in this chapter is part of work published in IEEE IUS 2021 proceedings. © 2021 IEEE. Reprinted, with permission, from A. Singh *et al.*, "Using Passively Detected Acoustic Signals to Characterize Ultrasound Gated Nanoparticles," in *2021 IEEE International Ultrasonics Symposium (IUS)*, 2021, pp. 1–4, doi: 10.1109/IUS52206.2021.9593854.

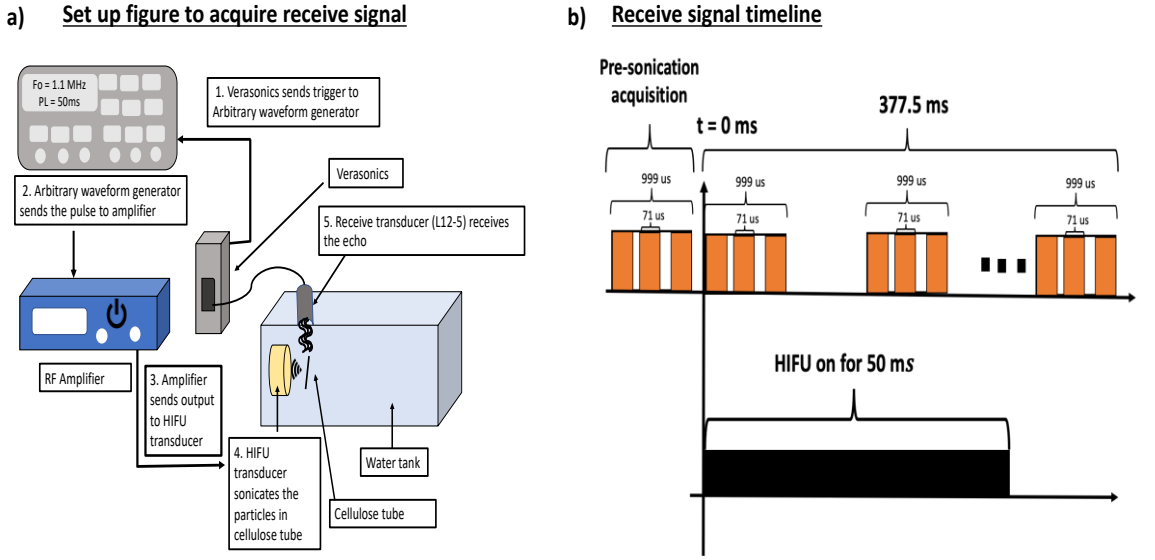

Figure 4.1: a) Set up figure shows steps to acquire receive signals, which result from sonicating NPs with FUS, on to a multi-element imaging transducer set on receive mode. Verasonics triggered imaging transducer L12-5 and arbitrary waveform generator at the same time. Arbitrary generator sends out signal at 1.1MHz which is then amplified by the RF amplifier. Amplified signal is the output to the HIFU transducer which then sonicates the particles in the cellulose tube. b) Prior to sonication, the imaging transducer records baseline signal. At t=0ms, HIFU turns on for 50ms and at the same time imaging transducer records 71μs of RF data at 3kHz. The signal recorded on the imaging transducer is then used to create passive acoustic map.

4.2 Materials and Methods:

4.2.1 Focused ultrasound pulse

These nanoparticles were shipped overnight from Stanford University. Cellulose tube (Spectra/Por, Spectrum Laboratories Inc.) in Fig 4.1 was situated near the FUS focus. The cellulose tube was flowed with solutions of either nanoparticles (diluted in saline) or saline (control). The flowing solution was then sonicated by single element focused ultrasound (FUS) transducer (H101, Sonic Concepts Inc, Bothell, WA) with a frequency of 1.1 MHz [119], [200]. This FUS transducer was driven by an arbitrary waveform generator (Agilent 33511B, Santa Clara, CA,USA) which was connected to an RF Amplifier (E&I, Rochester, NY, USA) as shown in Fig 3.1. FUS pulses were at an MI of 1.4,1.8,2.2 and 3.0. The pulse length was 50ms and it was repeated for a total of 10 times. These parameters were consistent with what has been used previously to release propofol [200].

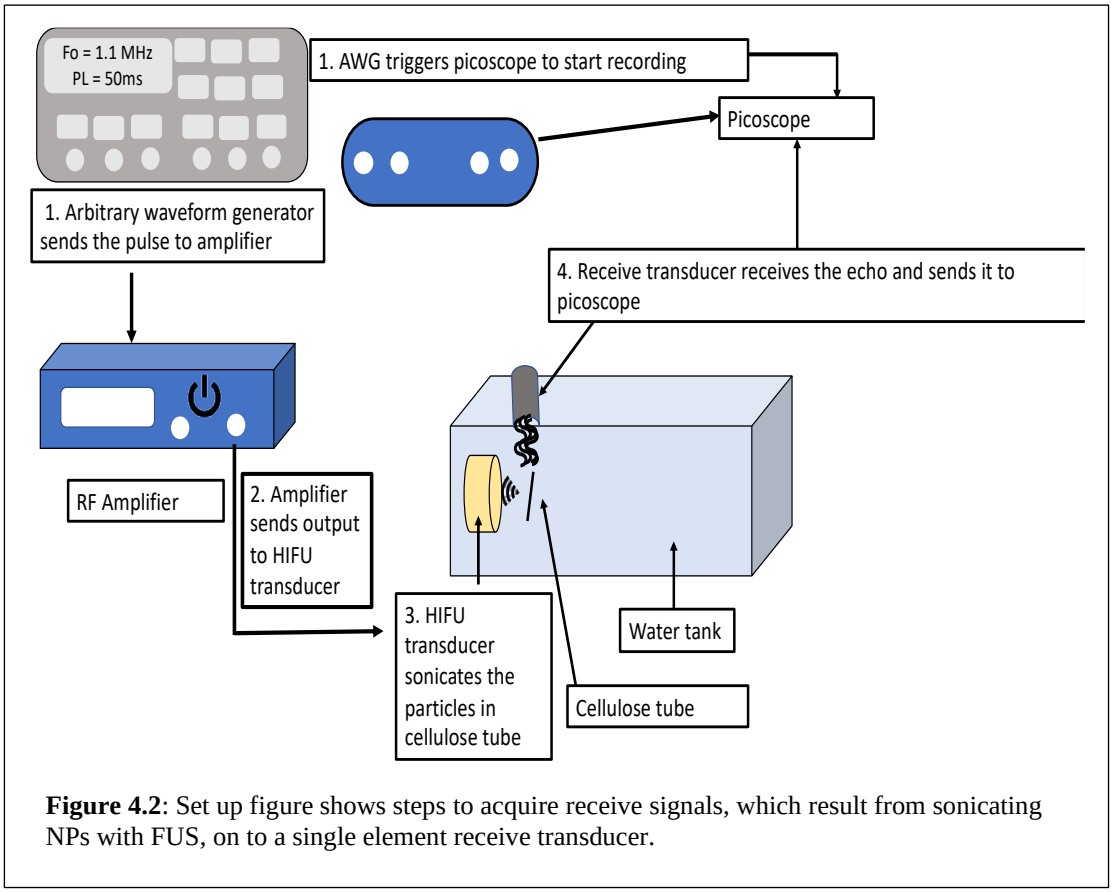

Figure 4.2: Set up figure shows steps to acquire receive signals, which result from sonicating NPs with FUS, on to a single element receive transducer.

4.2.2 Passive acoustic mapping using multi-element receive array

A 192 element array (L12-5) was set in receive mode to capture echoes arising from sonication of cellulose tube (Fig 4.1) using Verasonics (Verasonics Inc, Kirkland, Washington ,USA). The Verasonics system triggered FUS transducer (only at an MI = 2.2) and collected 77μs of RF data at 3kHz at a sampling rate of 35 MHz. A total of 377.7 ms of RF data was collected for every 50ms of HIFU pulse. RF data collected was then processed to make frequency spectrum graph and time exposure acoustics passive acoustic map and was used to count the instances of wideband signal.

4.2.3 Single element receive

A single element receive transducer in Fig 4.2 was used to collect passive receive data using Picoscope (PicoScope 3203D, Pico Technology, Tyler, TX). The receive data was sampled at 1 GHz and captured the entirety of the 50ms of HIFU pulse. This receive transducer was triggered by the arbitrary waveform generator, which also triggered the HIFU transducer at the same time. The RF data collected was first down sampled to 50 MHz and then an 18th order median filter was applied to the down sampled data to remove spike noise present in the measurement system. A bandpass filter between 10 Hz to 25 MHz was applied to this data thereafter. This filtered data was then

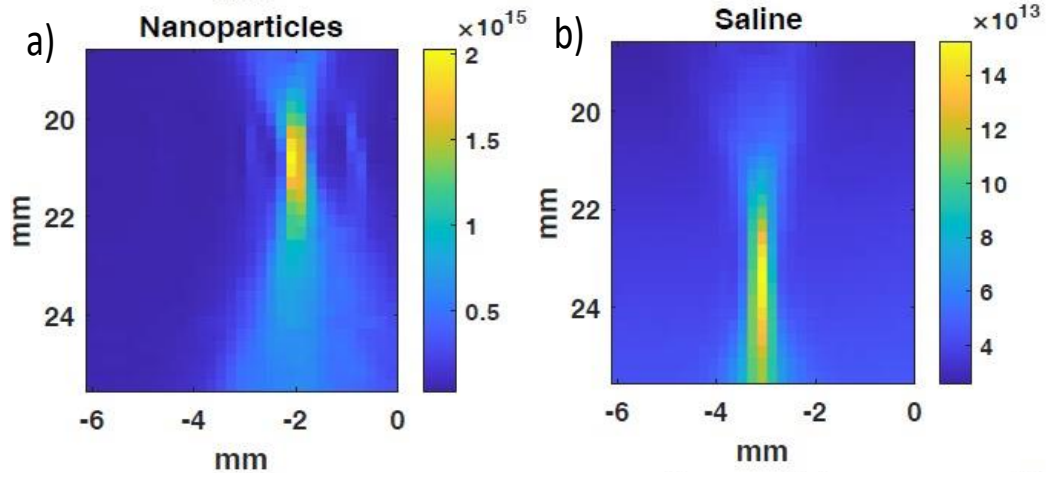

Figure 4.3: a) Passive acoustic map of nanoparticles. The regions of high intensity represent the regions undergoing cavitation and align well with where cellulose tube was located. b) Passive acoustic map created when saline flowing through cellulose tube was sonicated. The signal in saline is orders of magnitude less than that of NPs.

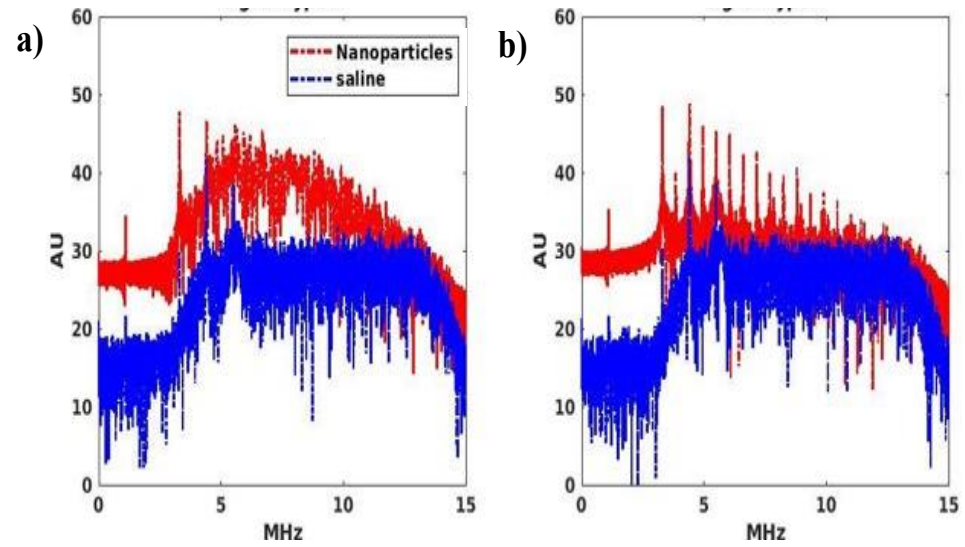

Figure 4.4: a) Wideband content present in nanoparticle trials upon FUS sonication. Such wideband signal was absent in saline alone. b) Ultra-harmonics were also seen in after FUS sonication of nanoparticles which was absent in saline.

used to compute spectrograms. For the spectrograms, a total of 1000 samples overlapped and total of 1024 points were used to compute discrete Fourier transform. We grouped spectrograms from saline and nanoparticle studies to visualize ultra-harmonic content content (e.g. fn = (n+1/2)f0 ,n = [1,2,…6]). We analyzed the ensemble of spectrograms by

counting the total number of spectrograms containing ultraharmonic magnitudes of >-40 dB at each pressure for samples with and without nanoparticles. We applied a chi-squared test of independence to compare echoes from solutions with and without nanoparticles as assess the effect of PNP on the presence of ultra-harmonic content.

4.3 Results:

4.3.1 Nanoparticles generated ultra-harmonic and wideband echoes that could be spatially mapped using passive acoustic mapping (PAM)

At an MI of 2.2, echoes received from nanoparticles showed wideband content (Fig 4.4a). In some instances, this wideband content was followed by ultra-harmonic seen in Fig 2b. The echoes from saline only contained harmonics of 1.1 MHz. Additionally, the wideband signal from the nanoparticles was successfully mapped using passive acoustic mapping (Fig 4.4a).

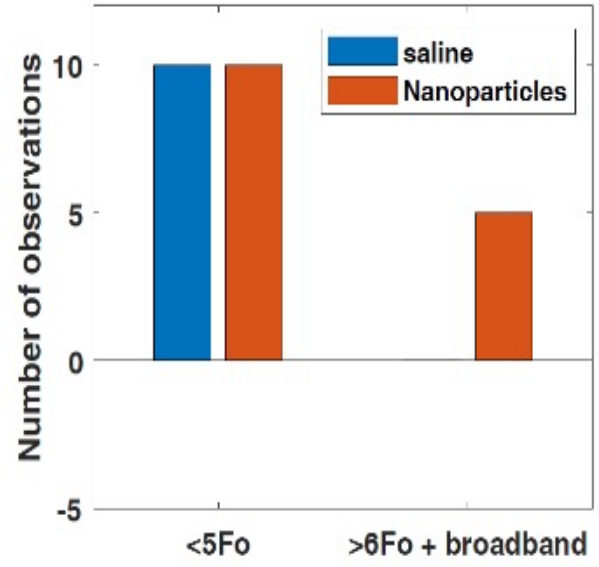

Figure 4.5: Number of trials in saline and in nanoparticles with harmonics and wideband content.

Passive acoustic map of saline was order of magnitudes less than that of nanoparticles (Fig 4.3b).

4.3.2 Ultra-harmonics and wideband presentation in nanopaticle trials vs saline trials

In Fig 4.5, it is shown that approximately 50% of nanoparticle trials had wideband and ultra-harmonic content. These sporadic wideband content in nanoparticle trials prompted us to investigate it further with single element receive transducer where much of the variables, such as handling and storage, were tightly controlled.

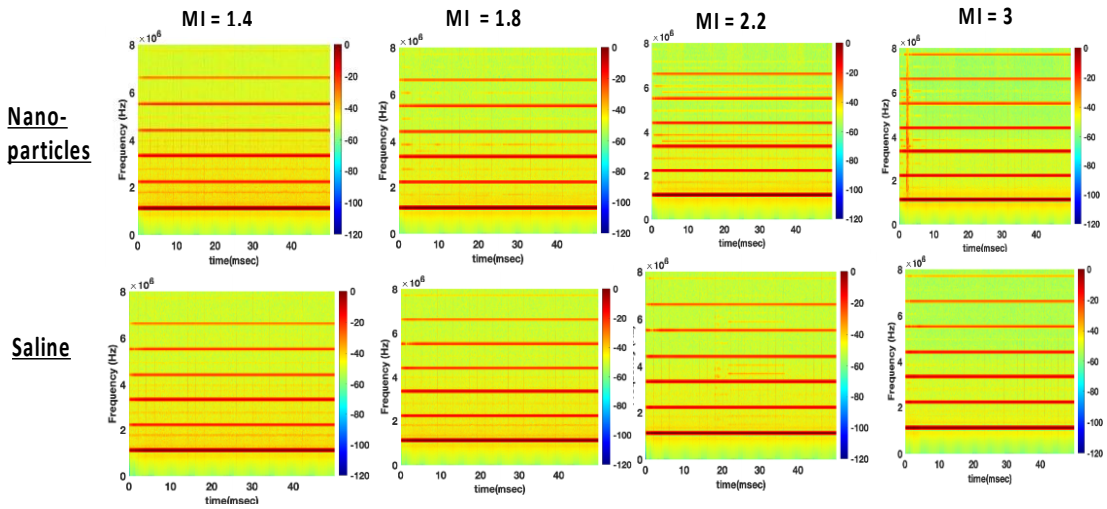

Figure 4.6: Spectrograms reconstructed from single element receive data. This spectrogram reveals that ultra-harmonics start to appear at MI of 1.8 in NPs but do not appear until MI of 2.2 in saline. Additionally, at an MI of 2.2, the number of harmonics in NPs are greater than saline and they are also present for longer duration in NPs than in saline. At MI of 3, NPs have wideband signal that give rise to ultra-harmonics. Such wideband and ultra-harmonic signals were absent in saline at MI = 3.

4.3.3 Echoes from nanoparticles had greater harmonic content and earlier onset of wideband emissions compared to saline

Spectrograms in Fig 4.6 show an onset of ultra-harmonic in nanoparticles trials at an MI = 1.8. The onset of ultra-harmonic content at MI of 1.8 was absent in all 10 trials of saline. Ultra-harmonics at f_n = 2.25 MHz and at 3.75 MHz was present for the entirety of the HIFU pulse in nanoparticles at MI = 1.8. At an incident pressure with MI of 2.2, both saline and nanoparticles emitted harmonics. However, there are differences in the number of ultra-harmonics, the timing and duration of those ultra-harmonics. In saline, harmonics were present between 3.3 MHz and 4.4 MHz and then again between 5.5 MHz and 6.6 MHz. These ultra-harmonics start at 20ms and end at 35ms. In the presence of nanoparticles, ultra-harmonic echoes occurred between each harmonic starting from 1.1MHz up until 6.6 MHz. In each of these cases, these ultra-harmonics lasted for the entirety of HIFU pulse. At MI = 3, saline presents no ultra-harmonic content whereas nanoparticles show a brief wide-band signal which is followed by ultra-harmonic content.

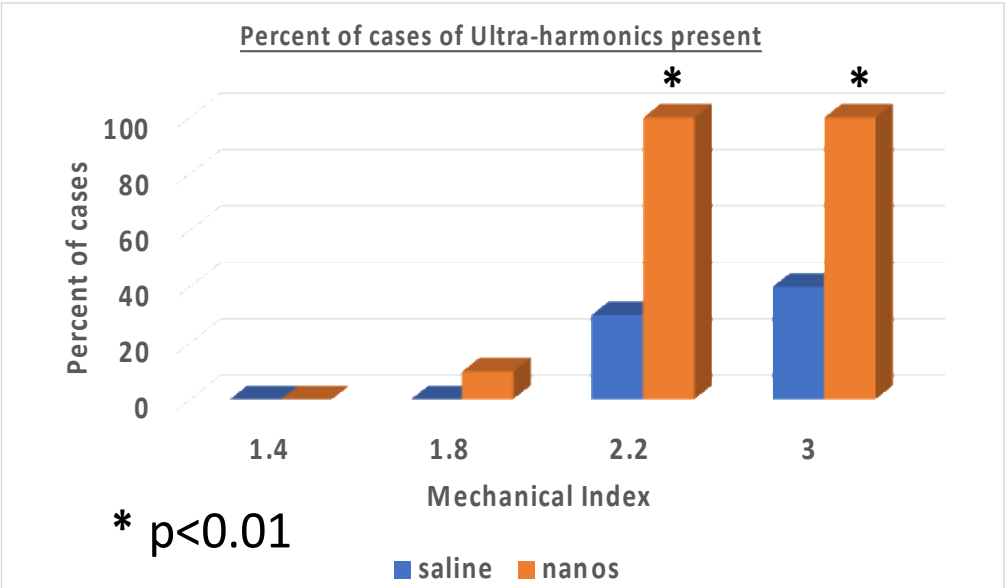

Figure 4.7: Percent of cases in which ultra-harmonics were present in saline vs nanos in single element receive data. At an MI of 1.8, 10% of NPs trials have ultra-harmonic content whereas 0% of saline present this ultra-harmonic content at MI of 1.8. At higher MI, NPs have twice the number of trials with ultra-harmonic content than saline.

4.3.4 Ensemble analysis of ultra-harmonics presentation at high MI shows significant association between presence and absence of nanoparticles

Fig 4.7 represents the percent of cases in which ultra-harmonics were present in saline vs nanoparticles trial. Such ultra-harmonics were present in 10% of cases of nanoparticles at MI = 1.8. However, this was not the case with saline where ultra-harmonics were absent in all trials at MI = 1.8. At higher MI of 2.2 and 3, ultra-harmonics start to appear in saline but the number of trials in which ultra-harmonics were present in nanoparticles were nearly double than that of in saline. A chi-squared test of independence showed that there was a significant association between the type of material (nanoparticles and saline) and ultra-harmonic presentation at MI of 2.2 and 3 ($p < 0.01$). No such significance was found at MI of 1.8 ($p=0.305$).

4.4 Discussion

Neuromodulation is a desirable treatment option for epilepsy, tremor or OCD. One widely used technique to treat such disorders is deep brain stimulation but it is invasive and carries many side-effects [198]. FUS is an attractive option for neuromodulation since its non-invasive and can cause safe neuromodulation. FUS, however, by itself can only elicit effects based on the natural response of the neurons. When coupled with acoustically active particles, FUS can elicit more predictable neuromodulatory activity. One such way to do it by combining FUS with nanoparticles that release propofol upon FUS application at MI ≥ 1 [22]. Greater amounts of drug release, which is possible at high FUS pressures, are desirable but increasing pressure can cause unintended bio-ef fects due to cavitation. In this study, we investigated echoes in an in-vitro setting by flowing saline with and without nanoparticles. We, then, collected these echoes using single element and multi-element receive transducer. The passive acoustic map from NPs in Fig 4.3 show cavitation activity in the presence of NPs. The spectrogram in Fig 4.4a also reveal wideband content in presence of NPs at MI of 2.2 which is otherwise absent in saline. As previously mentioned, such wideband content is undesirable as it could lead to harmful bioeffects. We addressed this situation by changing our handling protocol such that variables like storage temperature during experiment are in better control. We simplified our experiment further by using single element for receive (Fig 4.2). The spectrograms created from single element receive data showed ultra-harmonics in nanoparticles at lower pressures than that of saline. However, there was no wideband content at MI of 2.2. Wideband content was only present at MI of 3. Additionally, there was significant association between the type of material (saline and nanoparticles) and ultra-harmonics presentation.

The NPs used in our study release propofol at a threshold of MI = 1 [22], and this release is enhanced at higher MI. In our study, we sought to explore higher MI with the goal of increasing drug delivery while monitoring acoustic echoes that could be used to monitor particle activity during nanoparticle procedures. We explored pressures that release propofol starting at MI of 1.4, while keeping the pulse duration the same as prior studies [119]. We did not identify a unique spectral acoustic activity at MI=1.4 (e.g. pressure near the threshold of propofol release), but at MI of 1.8, NPs started to exhibit ultra-harmonic content. The magnitude of harmonic content present in echoes recorded on a single element receive from nanoparticles was 20 to 40 dB less than the fundamental. At MI of 2.2, echoes from NPs contained a greater number of ultra- harmonics. At MI of 3, NPs exhibited a wideband spectral

content. Wideband content had magnitude on the order of the fundamental frequency and could likely be used as an indicator for safety during NP procedures. In case of our negative control, saline, ultra-harmonics were only seen at MI of 2.2 and above. In none of the cases, wideband signals were observed in saline. Overall, our study identified a unique acoustic signature in form of ultra-harmonics from NPs that occur at pressures above the release threshold and highlights the importance of using acoustic feedback to monitor echoes from drug releasing nanoparticles—an approach that has been successfully employed with perfluorocarbon-based nanoparticles and microbubble therapies [60], [132], [201]. Our future directions include incorporating real-time acoustic feedback into nanoparticle therapies and assess whether frequency PAM could be used to identify ultra-harmonic echoes.

CHAPTER 5: An all-ultrasound method that combines power Doppler and passive acoustic mapping with steerable focused ultrasound array to monitor and open blood brain barrier in rats[3]

5.1 Introduction:

Focused ultrasound (FUS), when paired with microbubbles (MBs), can open the blood brain barrier (BBB) reversibly and safely in animal models[55], [115], [156], [202] .Opening BBB with FUS can help in successfully transporting various drug molecules such as doxorubicin and neurturin across BBB in small animals and can further enhance treatment of brain tumors and provide neuroprotection for Parkinson's disease[7], [56]. In clinical trials[6], researchers have opened the BBB using MR-guided focused ultrasound to deliver chemotherapy drugs to the brain in humans using [6], [53] and demonstrated feasibility of BBB opening in patients with Alzheimer's.

Focused ultrasound blood brain barrier opening (FUS-BBBO) typically targets specific regions of the brain and requires image guidance. In oncology applications, BBBO typically is targeted to the tumor region to enhance permeability to drugs or the blood-tumor barrier[118], [203]. In neuroscience applications, researchers have delivered molecules to elicit neuromodulation using schemes such as delivery of anesthetics[22], [60] or designer-receptors activated by designer drugs[204] to specific brain regions of rodents. Accurate targeting is fundamental to the experimental design of these studies, since the region of BBB opening must be located within a desired location (e.g., tumor, target brain region). MRI guidance is the gold standard and multiple systems exist that can apply FUS-BBBO under MRI guidance[86], [87]. To accurately place the FUS focus in the desired regions of the brain outside of the MRI, anatomical landmarks have been used [22] while other researchers have used a cross grid placement on the mouse skin of the skull which is visible in B-Mode image of the imaging transducer co-axially aligned to a single element FUS transducer [116]. The procedure was successful, with targeting accuracy within 2mm. In another study[135], researchers targeted hippocampus within 0.5mm of the actual FUS focus using single-element FUS transducer, with axial FWHM (=13mm) spanning entirety of the mice brain, to open BBB in mice using similar grid positioning system that used sutures of the skull as anatomical landmarks. Researchers, however, noted that sutures were not visible for all kinds of mice.

3. Work presented in this chapter is currently under review at Scientific Reports.

Ultrasound imaging presents a potential solution for guiding transcranial FUS procedures and indeed ultrasound imaging has often been used to guide focused ultrasound procedures in soft tissues, such as the liver[27]. However, B-mode imaging is of limited use in the brain due to attenuation in the skull. High frame Doppler with microbubbles has recently established itself as a powerful neuroimaging tool capable of visualizing vascular structures and providing functional information [134], [138], [140]. Brain vasculature can be visualized by using ultrasound contrast agent during imaging procedures [139]. Using contrast agents, such as microbubbles (MBs), to create power doppler images revealed vasculature in the brain at a micrometer scale and made ultrasound localization microscopy and functional ultrasound possible[134], [138], [145]. By combining imaging of brain vasculature and functional activity with array-based steering, treatment planning with accuracy equivalent to MR-guided FUS procedures is possible.

Here, we developed methods to steer a FUS transducer array, with axial FWHM spanning only 2.7mm, in a 2D plane using power Doppler imaging for guidance. We registered the imaging transducer with FUS array and used vascular reference points to guide the ultrasound focus to the intended target. During BBB opening, we received echoes at high frame rate to reconstruct robust capon beamforming passive acoustic maps (RCB-PAM)[148], [170] and overlayed these maps on power Doppler images[205] to visualize the area undergoing cavitation. We quantified the targeting error in our ultrasound-guided focused ultrasound (USgFUS) system *in vitro* using a cellulose tube in agar phantom and a cellulose tube in skull phantom with MBs flowing through it. The performance of power Doppler for image guidance was validated in healthy rats by opening the BBB in a cortical region of the left hemisphere. BBB opening was visualized using Gd-contrast MRI and was compared to RCB-PAM data. By overlaying the RCB-PAM image on the T_1-weighted (T1W) MRI coronal slice, we visualized regions that underwent FUS treatment and BBB opening procedure. Our study demonstrates an all-ultrasound method for combining power Doppler with a steerable focused ultrasound array to guide millimeter-scale FUS BBB opening while mapping and monitoring cavitation activity.

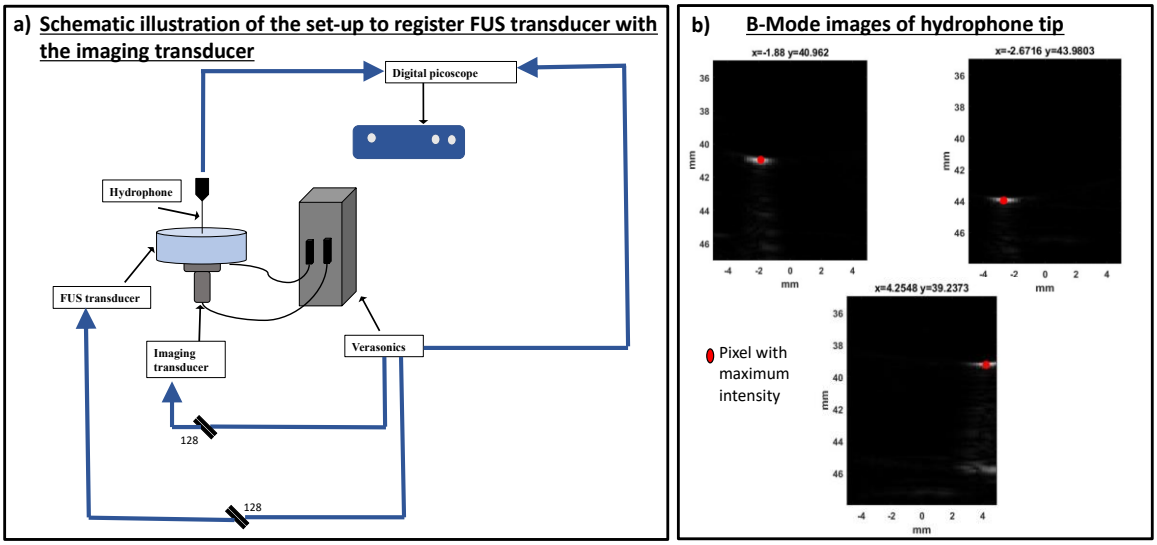

Figure 5.1: Registering FUS transducer with imaging transducer using a needle hydrophone. a) This set up figure shows a schematic diagram to record B-Mode hydrophone positions to register FUS transducer with the imaging transducer. First, Verasonics triggered the digital picoscope and FUS sonication at the same time (Step 1). Hydrophone, which was attached to a 3D axis stage, was then manually moved until the pressure reading on the Picoscope was maximized. The maximized pressure corresponded to the FUS focus (Step 2). FUS sonication was stopped once the focus was found. Imaging transducer was then turned on to gather B-Mode images of hydrophone (Step 3). The resulting B-Mode IQData was saved for post-processing. b) B-Mode image of hydrophone tip as seen by L12-5 transducer. Red dots represent pixels with maximum intensity and the values corresponding to this point is in the title of image. A total of 6 B-Mode images were collected to calculate rotation and translation matrix to register imaging transducer with FUS transducer. Another 7 B-Mode images were collected to verify registration and calculate target registration error.

5.2 Materials and Methods:

5.2.1 Registering imaging transducer with focused ultrasound transducer

We used a 128-element focused (FWHM = 2.6mm X 0.65mm x 0.3mm) ultrasound transducer[206] with a center frequency of 1.5 MHz (Imasonic SAS, Besançon, France). This focused ultrasound transducer has an opening for imaging transducer L12-5 such that it is coaxially aligned with the FUS transducer. We sonicated a 10-cycle FUS pressure pulses at 1.6V input voltage with a pulse repetition frequency of 1.5kHz using Verasonics Vantage system (Fig 5.1) (Verasonics Inc,Kirkland, WA, USA). We steered the focus to a location within the image plane and positioned the hydrophone using a manual 3-axis manipulator. Picoscope software (Pico technology, Tyler, TX, USA) amplified the signal record ed by needle hydrophone and displayed the signal on the computer. We maximized this signal so that the hydrophone tip was located at the focus. We detected the location of sonication the hydrophone, we set the L12-5 transducer in B-Mode at 8.9 MHz using Verasonics and recorded the location of the hydrophone. We saved the IQ data for post-processing to find the pixel with maximum intensity which would correspond to the tip of the hydrophone as shown in Fig 5.2a. We, then, steered FUS transducer at 6 different locations for the purposes of registration. After collecting the points, we computed the rotation matrix and translation vector required for rigid transformation using least square estimation such that equation 1 was satisfied[207]

$$\boldsymbol{y_{FUS}}' = R\boldsymbol{x_{imaging}} + \boldsymbol{t} \qquad (1)$$

We estimated our fiducial registration error using these transformed 6 points. After calculating rotation and translation matrix, we gathered 7 more points at imaging and FUS coordinates to compute the target registration error of points that were not used as input fiducials. We transformed these 7 imaging coordinates into FUS coordinates and compared transformed coordinate values (red circles) with ground truth FUS coordinates (blue diamond) in Fig 5.2b. Using transformed points and actual points, we calculated target registration error.

5.2.2 Microbubble fabrication

We produced lipid-shelled microbubbles in-house following the methods described in Borden et al 2005 [208]. Briefly, we combined and dried into film 90mol% 1,2-distearoyl-sn-glycero-3-phosphocholine (DSPC) and 10mol% 1,2-distearoyl-sn-glycero-3-phosphoethanolamine-N-[amino(polyethylene glycol)-2000] (DSPE-PEG2k) and resuspended it to 2.5mg/ml in microbubble buffer solution (80% v/v of 0.9% NaCl, 10% propylene glycol [1,2-propanediol], and 10% glycerol). We degassed the solution and filled the head space with F10C4 (FluoroMed, Round Rock, TN, USA). We repeated this process for a total of 3 times. We agitated bubble solution using a VialMix (DuPont, Wilmington, DE, USA) for 45 seconds to form microbubbles prior to experimentation. We purchased DSPC and DSPE-PEG2k from Avanti Polar lipids (Alabaster, AL, USA).

5.2.3 Confirmation of registration by using rotation and translation matrix in in-vitro phantoms of cellulose tube with and without skull phantom surrounding it

We first tested our registration in a 200 μm cellulose tube (Spectra/Por, Spectrum Laboratories Inc., USA) embedded in 2% agar (NOW Foods, IL, USA) phantom and then in cellulose tube inside a skull phantom. The concentration of microbubble and flow rates were identical in both *in-vitro* phantom. Briefly, we diluted microbubbles in saline at a concentration of 50µL in 1 mL to ensure there were enough microbubbles present for all trials. While the MBs were flowing in cellulose tube at 12 mm/sec, we captured and saved B-mode images at 50Hz. We captured a total of 1000 frames at 8.9 MHz. We subjected these 1000 frames to SVD filtering to eliminate any static signals, thereby leaving only microbubbles signals [205]. We selected a cutoff of 250 singular values to filter any static signal. After SVD filtering, we displayed SVD reconstructed image was on the screen and used MATLAB's ginput function to select target points on the cellulose tube. We used rotation and translation matrix to transform this selected point into FUS coordinates system and calculated amplitude and phases of the FUS transducer to steer to this point[164]. We sonicated this point was with a 100µs pulse at 1.5 MHz with 1.5 MPa free field pressure in the cellulose tube in water and at 2.5 MPa free field for cellulose tube in the skull phantom. While the FUS was on, we set imaging transducer in the receive mode to receive 96µs of receive data for each 100 µs of FUS on time. We sonicated with a total of 67 bursts of 100 µs pulses were every 1s. We repeated this transmit on FUS and receive on imaging for a total of 10 times at 1 Hz PRF for one point and repeated this procedure for 3

different steered position for the *in vitro* phantoms (i.e., Agarose-embedded tube and tube within skull). We processed the receive data offline to reconstruct passive acoustic mapping using robust capon beamforming method passive acoustic mapping (RCB-PAM) due to its ability to improve spatial resolution and removal of any incoherent artifacts[170]. The RCB-PAM algorithm can localize acoustic cavitation activity[160] and is briefly explained below. Assuming that there is a single acoustic event at location r with acoustic strength $q(\boldsymbol{r}, t)$, the pressure generated at point $\boldsymbol{r}'$ at time t will be:

$$p(\boldsymbol{r}', t) = \frac{q(t - \frac{|\boldsymbol{r}' - \boldsymbol{r}|}{c})}{4\pi|\boldsymbol{r}' - \boldsymbol{r}|} \qquad (2)$$

where *c* is the speed of sound in the medium. We set the speed of sound for phantoms in this study between 1450-1460mm/s to account for refrigeration of our skull and cellulose tube phantom at 4°C[209], [210] and at 1480mm/s for water at 20°C for our *in-vivo* study. We refrigerated this phantom to prevent denaturation of the phantom and to ensure repeatability of our experiment. Equation 2 considers the spherical propagation of the acoustic wave and time of arrival from the source of observer. By inverting equation 2, we can estimate acoustic source strength based on the acoustic pressures $\tilde{p}(\boldsymbol{r}_i, t)$ detected at each pressure sensor $\boldsymbol{r_i}$ for course of time t. The estimated acoustic strength $\tilde{q}(\boldsymbol{r}_i, t)$ is then calculated by applying relative delays to the acoustic signal of the i-th channel and averaging it across the *N* channels:

$$\tilde{q}(\boldsymbol{r}, t) = \frac{1}{N}\sum_{i=1}^{N} 4\pi|\boldsymbol{r_i} - \boldsymbol{r}|w_i\tilde{p}\left(\boldsymbol{r_i}, t + \frac{|\boldsymbol{r_i} - \boldsymbol{r}|}{c}\right) \qquad (3)$$

where w_i is the weight applied to the i-th channel. The RCB method determines the apodization weights w_i appearing in equation 3 that helps with suppression of interference pattern that otherwise arises in TEA – PAM algorithm. Eventually, we can use $\tilde{q}(\boldsymbol{r}, t)$ to calculate estimated acoustic energy radiated by a single acoustic event using equation 4 below:

$$\tilde{E}(\boldsymbol{r}) = \frac{1}{4\pi\rho_0 c}\int_0^T \widetilde{q^2}(\boldsymbol{r}, t)dt \qquad (4)$$

where ρ_0 is the density of the medium and *T* is the total duration of the signal.

In matrix format, equation 3 can be written as:

$$q(x,t) = \frac{4\pi}{\alpha}\boldsymbol{w^T D(x) s(x,t)} \quad (5)$$

where α is the piezoelectric coefficient, $\boldsymbol{w^T}$ is weighting matrix applied to each channel, $\boldsymbol{D(x)}$ is diagonal matrix of distances from channel 1 to N to voxel $\boldsymbol{x}$ of interest:

$$\boldsymbol{D(x)} = diag[d_1(\boldsymbol{x}), \dots d_N(\boldsymbol{x})] \quad (6)$$

and $\boldsymbol{s(x,t)}$) is matrix of pre-steered data of N channels. A correlation matrix of pre-steered for an interval length of T can be written as:

$$\boldsymbol{R_s(x)} = \int_{t_0}^{t_0+T} \boldsymbol{s(x,t)\, s(x,t)^T}\, dt \quad (7)$$

The source energy can, for each voxel is then:

$$E(\boldsymbol{x}) = \frac{4\pi}{\alpha^2 \rho_o c}\boldsymbol{w^T D(x) R_s(x) D(x) w}. \quad (8)$$

We beamformed each of the 67 bursts of 100μs of data and used bursts that resulted in an RCB PAM for further analysis. We normalized the reconstructed PAM maps to their maximum intensity and then estimated the 2D spatial location of maximum intensity in the PAM maps ($pixel_{PAM} = [x_{PAM}, y_{PAM}]$) and location of the pixel that was clicked on the power Doppler image ($pixel_{PD} = [x_{PD}, y_{PD}]$)to calculate targeting error vector ($\overrightarrow{\boldsymbol{T_{error\_PAM}}}$)using equation 9:

$$\overrightarrow{\boldsymbol{T_{error\_PAM}}} = \sqrt{(x_{PAM} - x_{PD})^2 + (y_{PAM} - y_{PD})^2} \quad (9)$$

5.2.4 Reconstruction of spectrograms

We collected the receive RF data at sampling frequency of 35.6 MHz. We used this data to compute spectrograms. For the spectrograms, a total of 500 samples were overlapped and total of 504 points were used to compute discrete Fourier transform. We grouped spectrograms from baseline FUS sonication and MBs assisted FUS sonication to visualize harmonic content (e.g. fn = n*f0 ,n = [1,2,…8]) and ultra-harmonic content (e.g. fn = (n+1/2)f0 ,n = [1,2,…8]) in fig 5.7.

5.2.5 FUS blood brain barrier opening *in-vivo*

We anesthetized a male Sprague-Dawley rats (568g) using isofluorane and performed to enable MBs injection. We shaved the head and used Nair (Nair Hair Remover Lotion ,Church & Dwight Co., USA) lotion to remove hair to improve coupling. Ultrasound gel was applied and our FUS and imaging transducer was placed on the rat head. We injected MBs in rats and used L12-5, to capture, reconstruct and save 1000 frames at frame rate of 50Hz at 5.2 MHz. Each frame was composed of 7 compounded planes waves ranging from -18° to 18°. We performed SVD filtering according to steps listed above and displayed SVD filtered image on the screen. We used MATLAB's ginput function to select sonication points in the brain transformed them into FUS coordinates system using the rotation and translation matrix. We calculated amplitude and phases of FUS transducer using methods described elsewhere to steer to these points [164], [211], [212]. We sonicated the selected points sequentially with 69 pulses where each pulse was 100µs and was repeated at 9.8kHz with a center frequency of 1.5 MHz and peak negative pressure of 0.7 MPa (3.5 MPa free-field). These 69 pulses were repeated for a total of 150 times at 1 Hz PRF accounting for 150s of treatment duration. Before collecting BBBO data, we also collected 10s of baseline data where we sonicated the desired regions with 3 foci at 0.7 MPa but before MBs injection. We accounted for the weight of the animal, position of our FUS transducer, and FUS transmission frequency to calculate pressure transmission factor[213]. While the FUS was on, we received 96µs of RF data for each 100 µs of FUS on time on L12-5. We performed this transmit on FUS and receive on imaging for a total of 150s and collected receive data for all 150s. We processed the receive data offline to reconstruct PAM using RCB. We beamformed each of the 69 bursts of 100µs of data into an RCB-PAM and used it to calculate mean $\overrightarrow{\boldsymbol{T}_{\boldsymbol{error\_PAM}}}$ by taking into account each 100µs of 150s of data that resulted in RCB-PAM map. We normalized the reconstructed RCB-PAM maps to its maximum intensity and overlayed it over T1W image of BBBO region.

5.2.6 Gadolinium contrast imaging to confirm BBB opening

All procedures were reviewed and approved by the Vanderbilt University Institutional Animal Care and Use Committee. We anesthetized adult male rats with 2-3% isoflurane (ISO) for induction and 1.5-2% for maintenance during MR imaging. We monitored and maintained respiration and rectal temperature during MRI. Respiration was kept around 60 cycles/min, and a rectal temperature of 37.5 °C was maintained throughout the experiments using a warm-air feedback system (SA Instruments, Stony Brook, NY, USA). We collected MRI data on a Varian DirectDrive™ horizontal 4.7 T magnet using a 38-mm inner diameter transceiver coil (Doty Scientific Inc. Columbia, SC, USA). We acquired T1W images before and after gadolinium injection (Bayer HealthCare Pharmaceuticals, Whippany, NJ, USA) for confirming BBB opening (3D spoiled gradient echo sequence, TR/TE= 9/2.37 ms, flip angle = 7°, number of excitations = 8, matrix size = 128 x128 x 64, field of view = 32 x 32 x16 mm^3, resolution = 0.25 x 0.25 x 0.25 mm^3, acquisition time of 9 min 50s). To calculate BBBO opening volume, we took an ROI encompassing the BBB opened region, we took all the pixels 2.5 times the standard deviation of the background and multiplied those number of voxels with the resolution. We selected points surrounding the ventricles and other features present in both power Doppler image and MRI image and point registered red stars in Gd subtracted MRI image (Fig 5.10b) to green stars in power Doppler image (Fig 5.10b) using the same method described in equation 1. We then overlayed RCB-PAM map onto the BBB opened regions. The point registered MRI images were used to calculate target error vector of opening BBB $\overrightarrow{\boldsymbol{T}_{\boldsymbol{error\_BBB}}}$ in equation 10, which is the difference between pixel of highest intensity of BBB opened region in the MRI image($pixel_{MRI} = [x_{MRI}, y_{MRI}]$)and location of the pixel that was clicked on the power Doppler image ($pixel_{PD} = [x_{PD}, y_{PD}]$) to open BBB. This was possible because after registration, both MRI image and power Doppler images were in the same coordinate system.

$$\overrightarrow{\boldsymbol{T}_{\boldsymbol{error\_BBB}}} = \sqrt{(x_{MRI} - x_{PD})^2 + (y_{MRI} - y_{PD})^2} \quad (10)$$

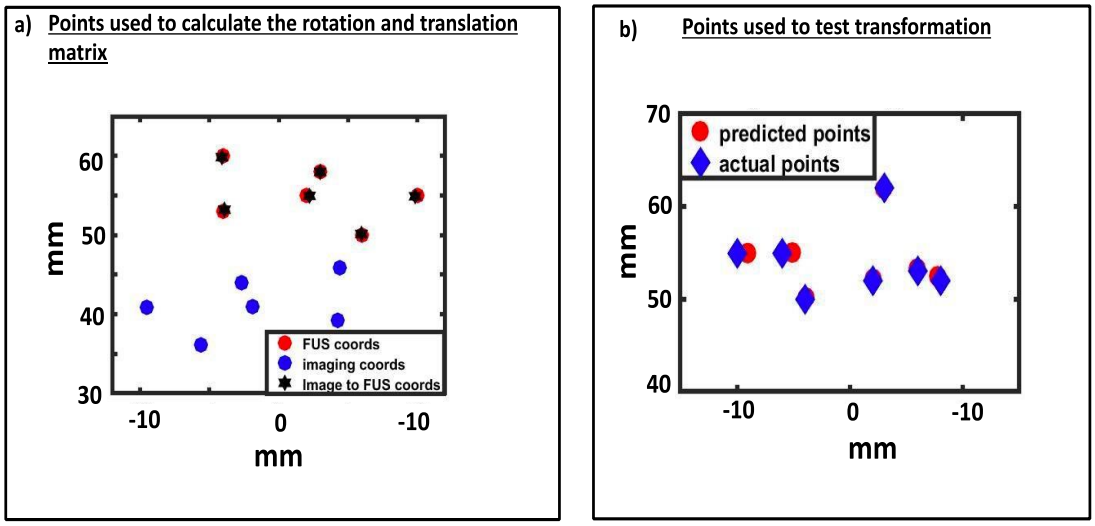

Figure 5.2: Registering imaging transducer to FUS transducer using rotation and translation matrix**.** a) Imaging coordinates in blue circles were registered to FUS coordinates in red circle. These points were used to solve for equation 1 to yield R (rotation matrix) and t (translation matrix). The FRE was 0.18mm. The R and t values obtained were applied to blue circular points to yield black star points. The values of R and t were used to then transform other imaging coordinates into FUS coordinates. c) Another 7 non-fiducial imaging points were then registered to FUS coordinates. The TRE for this registration was 0.59 ± 0.26mm.

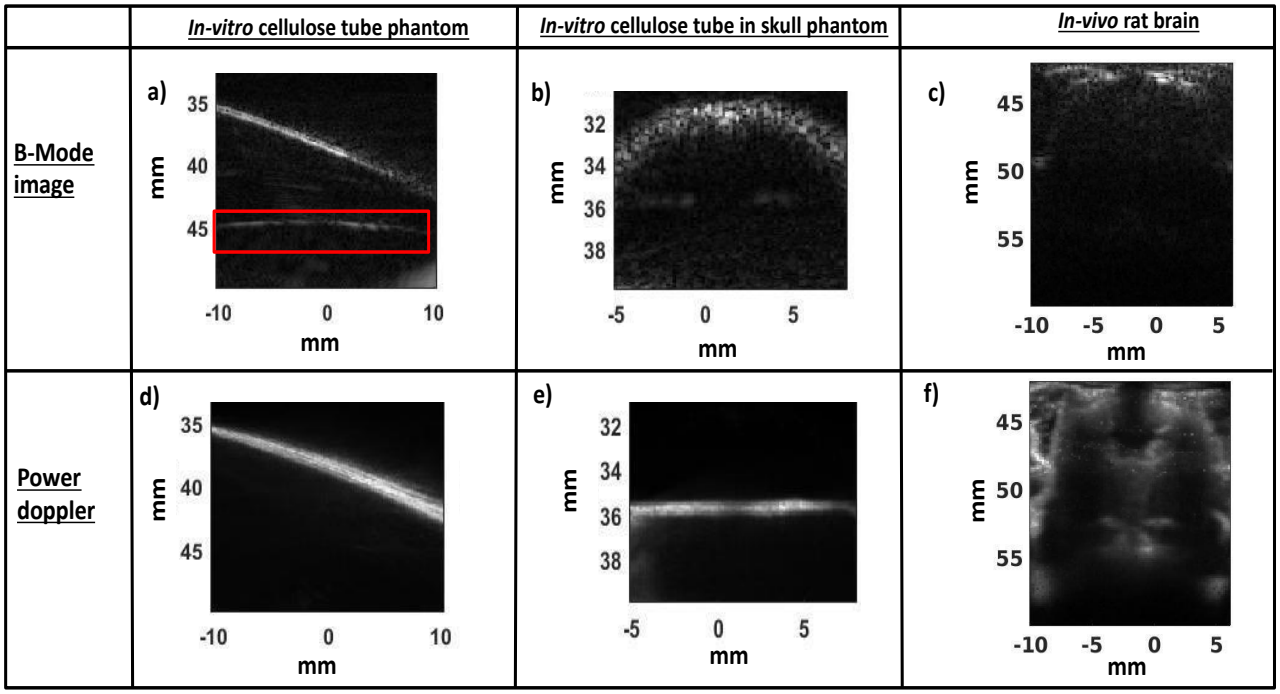

Figure 5.3: Power Doppler filters stationary and static tissue signals to reveal signal from flowing microbubbles. We filtered B-Mode data on the left using SVD filter. Briefly, a total of 1000 B-Mode frames obtained at 8.9 MHz at a frame rate of 50 Hz was filtered to remove any stationary signal in in-vitro setting. After filtering, static signals that is present in red rectangle in B-Mode image in a) in in-vitro cellulose tube in agar phantom is filtered from power Doppler image in d). When we applied SVD filtering to in-vitro skull phantom, the skull in b-mode in b) is no longer visible in e). With SVD filtering, only the tube with MBs flowing can be seen at around 36mm. In the in-vivo setup, a total of 1000 frames were acquired at 5.2 MHz. The transmission frequency was reduced to account for skull thickness of a 7 month old rat. SVD filtering on the B-Mode data in c) was able to successfully eliminate signal from arising from the skull and was able to reveal the rat brain vasculature. These SVD maps were used for targeting and steering the FUS transducer.

5.3 Results:

5.3.1 Registering image and therapy coordinate systems:

Using experimental set up shown in Fig 5.1, we steered the transducer to 6 points and positioned the hydrophone so that the pressure was maximized at each point. We then solved for the registration transform between the hydrophone tip locations in the B-mode image (red circle in Fig 5.2a) and steering location in the FUS transducer coordinate system. We registered six imaging coordinates to six corresponding FUS coordinates to create a transform from imaging coordinates to FUS coordinates (Fig 5.2b). The fiducial registration error (FRE) after registering these points was 0.18mm. We then gathered a separate set of paired hydrophone and image steering locations from those used to generate the transformation matrix and transformed these to the imaging coordinates. The target registration error (TRE) between predicted points and actual points was 0.59 ± 0.26mm (Fig 5.2c).

5.3.2 Power Doppler imaging with SVD filtering and RCB-PAM maps in-vitro

Power Doppler imaging with SVD filter isolated microbubbles signal in *in-vitro* cellulose tube: After validating registration, we acquired high frame rate images of microbubbles under flow applied SVD filtering to eliminate slow moving and static signal seen at the boundaries in red square in B-Mode image in Fig 5.3a to create image in Fig 5.3d. In *in-vitro* skull phantom, skull boundaries are present in B-Mode image in Fig 5.3b. Power

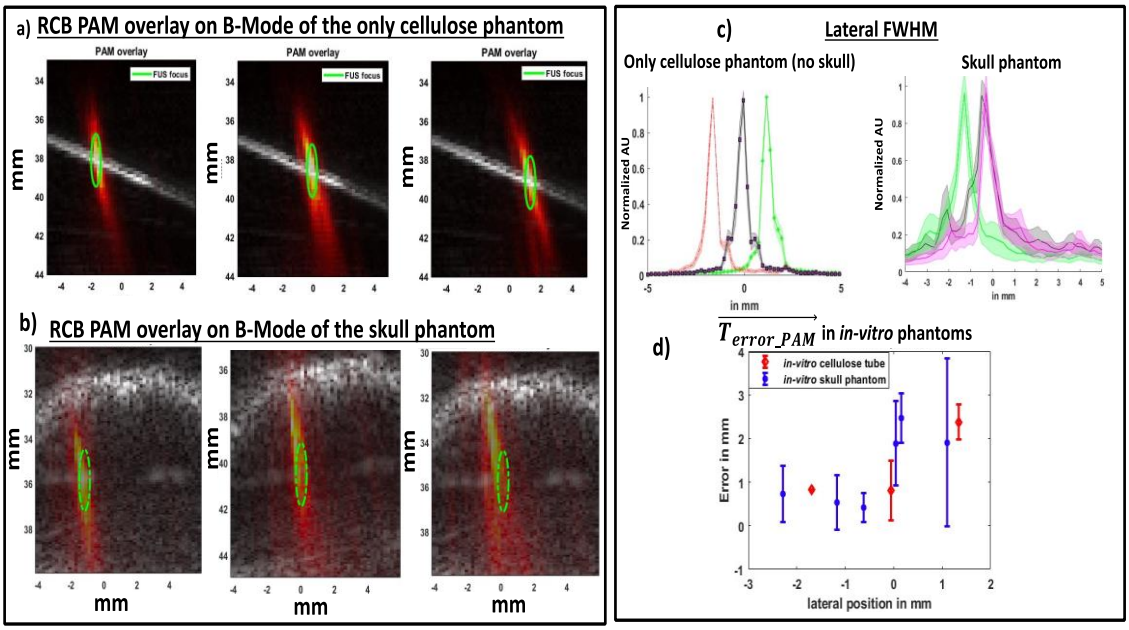

Figure 5.4: RCB-PAM can detect cavitation signal that arise from FUS sonication of MBs, even when transducer is steered. a) RCB-PAM map overlayed on cellulose tube B-Mode image in top row can reveal regions undergoing cavitation, even when transducer is steered to the right. Cavitation energy is contained within the green focus. b) RCB-PAM reconstruction can localize cavitation signal originating from cellulose tube in a skull phantom. An overlay of PAM-RCB on B-Mode image show that In 2/3 cases, majority of the PAM signal is contained within green FUS focus. c) The point of maximum intensity in 3 steered maps was calculated and plotted in lateral dimension for cellulose phantom with and without skull. For cellulose phantom without skull in, the calculated full width half max (FWHM) laterally for each steered location is 0.54±0.03 mm, 0.54±0.028 mm, and 0.56±0.03 mm respectively whereas the FWHM axial direction is 2.5±0.22 mm,3.02±0.13 mm,2.5±0.09 mm respectively The lateral FWHM of the points with maximum intensity in RCB PAM maps in skull phantom is as follows: 0.76±0.23 mm,0.89±0.07 mm, and. 0.69±0.16 mm FWHM along ellipsoid direction is 3.9±0.86 mm, 4.2±1.3 mm and 3.97±1.14 mm and this is also larger than FWHM of FUS focus (2.7mm) . d) A TREs comparison in in-vitro cellulose tube and skull phantom, each undergoing 10 trials, found that in majority of the cases, the $\overrightarrow{\mathbf{T}_{\mathbf{error\_PAM}}}$ is within 2mm. Error bars represent standard deviation.

doppler imaging in Fig 5.3e removed skull boundaries but retained signal coming from MBs flowing in the tube inside the skull around depth of 36 mm. *In vivo,* power Doppler imaging could successfully differentiate between tissue and blood flow signals and removed slow moving signal from B-Mode image (Fig 5.3c) to create transcranial vascular power Doppler image (Fig 5.3f). Power Doppler imaging was successful in removing skull boundaries that are present in the B-Mode image and reveal vasculature underneath.

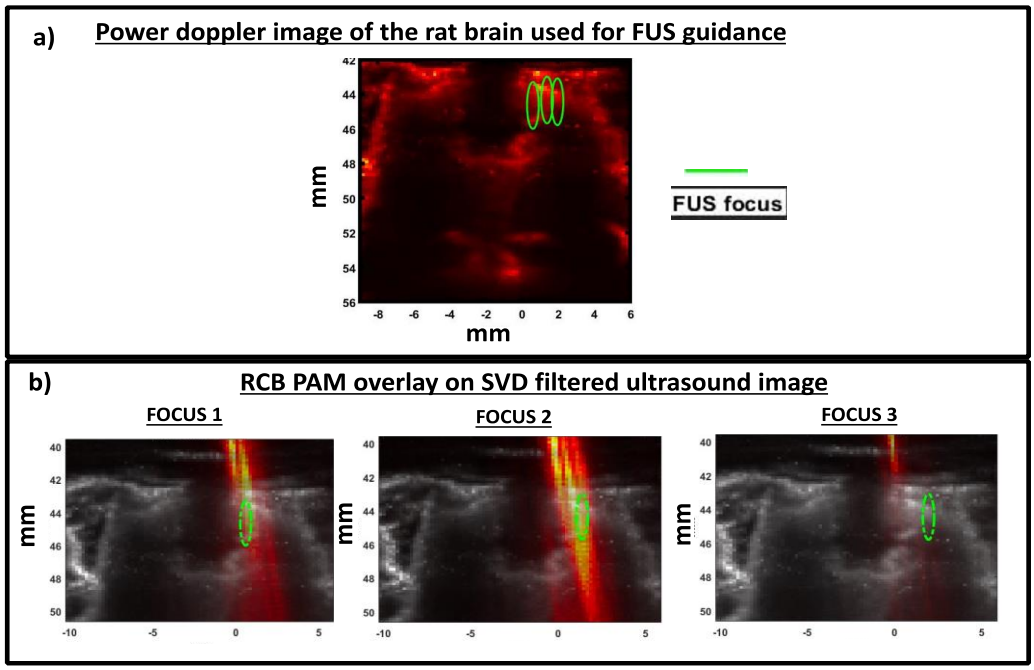

Figure 5.5: A power Doppler image can be used as a guidance to select regions to open BBB. a) SVD filtered image was used to open BBB. Three FUS foci (represented by green ellipsoid) was chosen such that our FUS transducer would sonicate 1 focus for 100μs at a time. Those points were clicked on the SVD image and ginput function from MATLAB was used to store the points. The stored points were then transformed into FUS coordinate system. The transformed coordinate system was used to solve Rayleigh Sommerfeld equations to calculate the appropriate phase and amplitude of the FUS transducer elements. b) RCB PAM overlayed on SVD filtered image show that PAM signals are present inside the intended FUS focus and inside the brain in 2/3 cases. For focus 3, we do not see any PAM signal near the focus. We believe that this is due to lack of MBs perfusion. For passively acquired signals, our 192 element transducer was set to only receive on the first 128 elements and this posed a physical limitation on which elements could receive signal in positive lateral dimension and resulted in inaccurate PAM map.

RCB-PAM maps reconstructed from signals received during FUS pulses designed for BBB opening have highest intensity located of the ultrasound focus (Fig 5.4a). The focus had an intensity profile with similar spatial dimensions as the point spread function of the L12-5 array. A plot of the location with maximum intensity across lateral dimension in Fig 5.4a for all 3 steering cases had a FWHM of 0.54 ± 0.03 mm, 0.54 ± 0.028 mm, and 0.56 ± 0.03 mm, while the intensity profile along the direction of the ellipsoid was 2.5 ± 0.22 mm, 3.02 ± 0.13 mm , and 2.5 ± 0.1 mm respectively. In the presence of the skull shown in Fig 5.4b, RCB passive acoustic maps detected steering of the focus laterally and axially but resulted in wider FWHM in lateral and axial direction. The plot of point with maximum intensity across lateral dimension in Fig 5.4b for 3 different steering cases had a FWHM of 0.76 ± 0.23 mm, 0.89 ± 0.07 mm, and 0.69 ± 0.16 mm while the steering profile along ellipsoid direction was 3.9

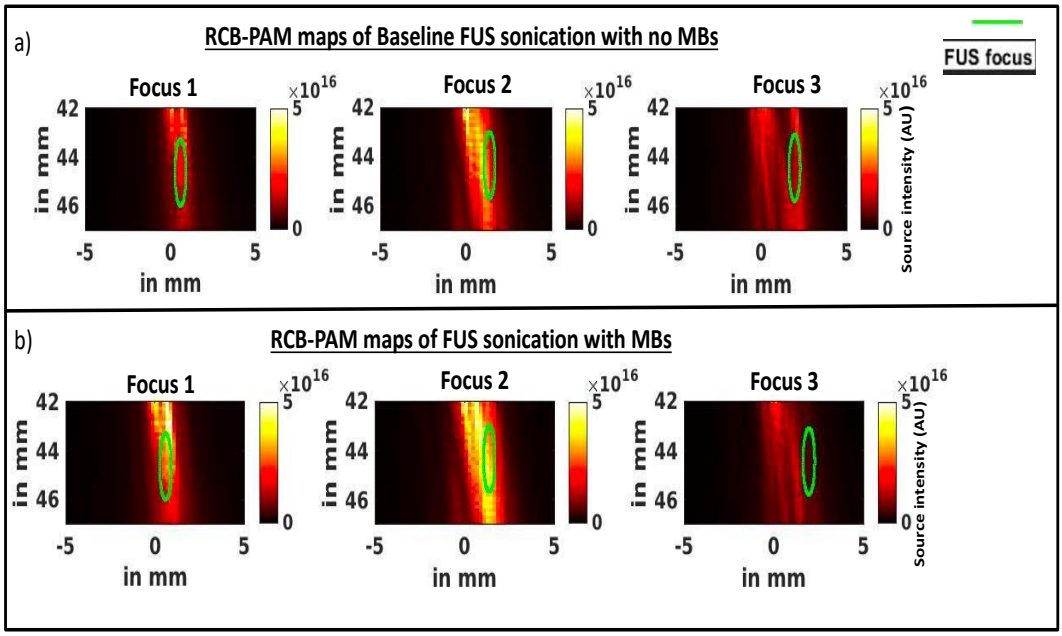

Figure 5.6: RCB-PAM can localize cavitation signals in an in-vivo rat brain with higher source intensity in presence of MBs than in absence. a) RCB-PAM maps of of focus 1, focus 2 and focus 3 of baseline show low magnitude intensities. Focus 2 shows some bright pixel but this pixel is close to the skull and could be attributed to skull reflection. The magnitude of the brightest pixels in focus 1 is $3.19e^{16}$, in focus 2 is $4.6e^{16}$, and in focus 3 is $2e^{16}$. b) RCB PAM image of FUS sonications with microbubbles show high intensity PAM maps. There is high intensity activity near the intended focus for foci 1 and 2. The PAM maps for focus 3 look similar to the baseline focus 3. The magnitude of the brightest pixels in focus 1 is $7.6e^{16}$, in focus 2 is $4.9e^{16}$ and in focus 3 is $2.1e^{16}$. The magnitude of the brightest pixel is more than 2 times in RCB-PAM map of focus 1 of FUS sonications with MBs than with no MBs. The value of brightest pixel in focus 2 in RCB-PAM maps with MBs is larger than without MBs but not as large as focus 1. However, the regions with higher energy is greater in RCB-PAM maps of focus 2 with MBs than without MBs. In RCB-PAM maps of focus 3 for both with and without MBs, these values are comparable.

± 0.86 mm, 4.2 ± 1.3 mm , 3.97 ± 1.14 mm respectively. RCB-PAM could localize signals in cellulose tube phantom in absence of skull and was used to calculate mean targeting error ($\overrightarrow{T_{error\_PAM}}$) in fig 5.4d, which is the error vector between the pixel with highest energy and pixel that was intended target. The $\overrightarrow{T_{error\_PAM}}$ in 1/3 steering cases of cellulose tube phantom with no skull was 2.37± 0.4mm. For 2 steering cases, RCB-PAM localized steering with sub-mm precision ($\overrightarrow{T_{error\_PAM}}$ of 0.81± 0.68mm and 0.81± 0.01mm). In 5/6 trials of cellulose tube inside the skull, the average $\overrightarrow{T_{error\_PAM}}$ for steering was within 2mm (0.94 ± 1.1mm, 1.88 ± 0.96mm ,1.9 ± 1.9mm, 0.42 ± 0.33mm, 0.5 ± 0.63mm, 2.47± 0.56mm, 0.72 ± 0.64mm).

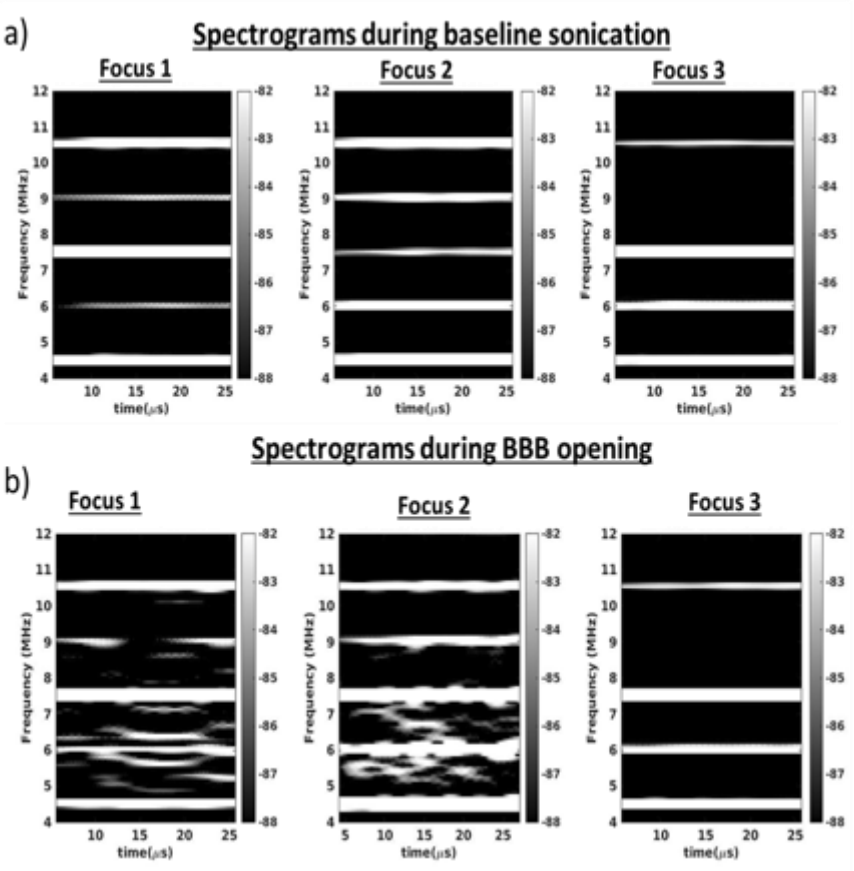

Figure 5.7: Spectrograms of FUS sonications in presence MBs overall reveal more wideband signal than in absence of MBs. a) The spectrograms of receive signal from the first 100μs of baseline FUS data show only presence of harmonics (f_0, $2*f_0$, $3*f_0$, $4*f_0$, .. $9*f_0$) for all 3 foci in baseline. b) The spectrograms of receive signal from the first 100μs of FUS sonication with MBs show greater presence of wideband signal in focus 1 and focus 2. There is overall more wideband signal of magnitudes ranging from -88dB to -82dB. There are also presence of harmonics and ultra-harmonics ($1.5*f_0$, $2.5*f_0$, $2.5*f_0$, $4.5*f_0$, .. $8.5*f_0$) in focus 2. In focus 3, the spectrograms look similar to focus 3 of the baseline where the wideband signal is absent and only harmonics and ultra-harmonics are present.

5.3.3 Guiding FUS therapy with power Doppler and RCB-PAM feedback in in-vivo rat brain

The SVD doppler filtered power Doppler image revealed vasculature in the rat brain that was otherwise not visible in the B-Mode image (Fig 5.3f). The vascular map served as a guide for FUS therapy as indicated by the green circle in Fig 5.5a. RCB-PAM maps for both focus in Figure 5.5b contains a majority of passive acoustic signal inside the SVD filtered brain image with $(\overrightarrow{T_{error\_PAM}})$ of 2.6 ± 0.89 mm for focus 1 and 2.3 ± 1.02 mm for focus 2. For focus 3, the RCB-PAM map contained majority of passive signals near the skull at around 42mm axially when the intended target was deeper at 44mm. We conducted further analysis and comparison of BBBO PAM data with our baseline data in Figure 5.6. We found that in the presence on MBs, the maximum intensity of PAM map was higher than in the absence of MBs for focus 1 (7.6×10^{16} vs 3.19×10^{16}) and focus 2 (4.9×10^{16} vs 4.6×10^{16}). In case of focus 3, the intensities were comparable (2.1×10^{16} vs 2×10^{16}). In focus 2, high intensities spanned larger axial regions than in focus 1 in presence of MBs. In our spectrogram analysis, we saw an overall greater presence of wideband signal in FUS sonication of focus 1 and 2 in presence of MBs than in absence of MBs (Fig 5.7a and Fig 5.7b). Spectrograms of receive signal in Figure 5.7a and 5.7b have more wideband signal in presence of MBs in focus 1 and focus 2. The spectrogram of focus 3 in the presence of MBs was similar to absence of MBs.

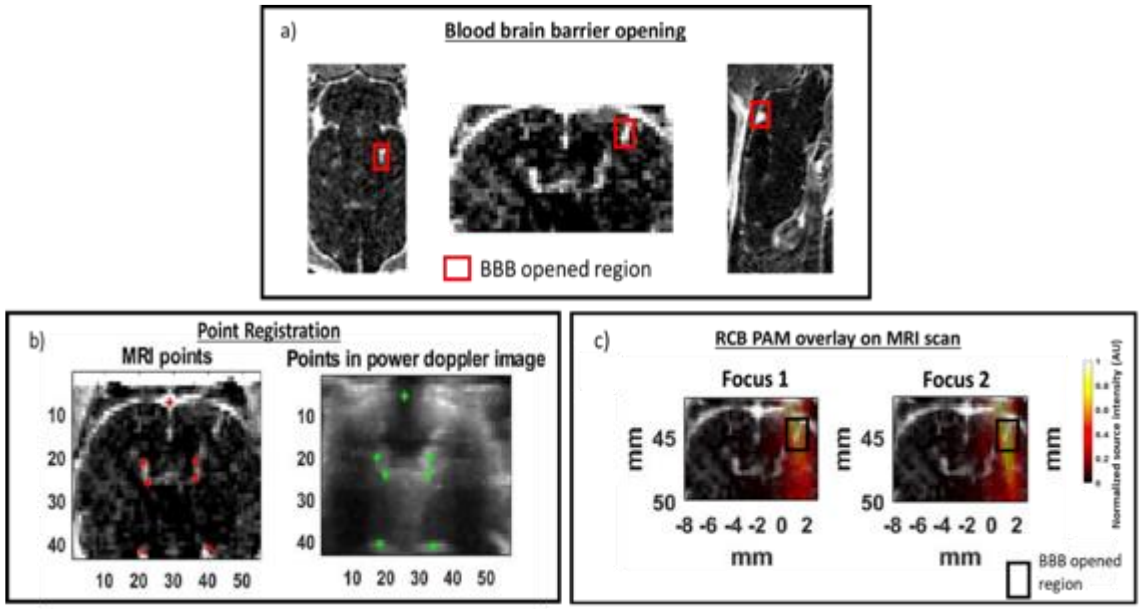

Figure 5.8: BBB opening confirmed in MRI images and overlaps with regions of high source intensity of PAM maps. a)BBB opening was confirmed in all 3 planes after pre-Gd MRI images was subtracted from post Gd-images. The red squares shows the locations of opened BBB. b) Presence and detection of large ventricle and other features present in both power Doppler image and MRI image enabled point registration of red stars in Gd subtracted MRI image to green stars in power Doppler image. c) After registering, two 100μs of RCB PAM data was overlayed, corresponding to two different FUS foci, over BBB opened MRI image. RCB-PAM signal of high spectral intensity is present in the regions that underwent BBB opening (inside the black square). Since FUS focus 3 did not result in any RCB PAM map, it was not used for this step.

BBB opening in gadolinium subtracted MRI images were visible in orthogonal planes (Fig 5.8a). The volumetric BBB opening did not exceed 0.21mm^3 which is less than half of the volume of our FUS focus (0.56 mm^3). After point registering red points in MRI coordinates to anatomical landmarks in the SVD doppler image (green points in Fig 5.8b), we overlayed PAM map onto the rat brain (Fig 5.8c), and the region of BBB opening was co-localized with the maximum of the RCB-PAM. Using equation 10, we found that the targeting error, $\overrightarrow{\boldsymbol{T}_{error\_BBB}}$, which is the error vector between the pixel with maximum intensity in BBB opened region of MRI image and the intended pixel in power Doppler image, was 1.1, 1.12 and 1.15 mm for focus 1, focus 2, and focus 3, respectively.

5.4 Discussion:

In this study, we used MB-enhanced power Doppler images to steer a FUS transducer to open BBB in rats and monitor the regions undergoing cavitation using RCB-PAM. We registered the imaging transducer with the FUS transducer and quantified the registration error. We characterized the ability to map bubble activity during MB-enhanced FUS therapy in an in vitro cellulose tube phantom with and without skull and found close correspondence between RCB-PAM map maxima and the steered FUS focal location. We applied these capabilities to open the BBB in rats and overlayed RCB-PAM maps on power Doppler image and Gd-subtracted T1W MRI, demonstrating a 0.21mm3 opening of the BBB in the location corresponding to the maximum of the RCB-PAM image. The system provides a method to open the BBB in rats with high accuracy and spatial selectivity.

Our in-vitro cellulose tube results without the skull in Fig 5.4a contained spectral energy in the RCB-PAM maps within the FUS focus. The FWHM for most of the cases were in excellent agreement with FWHM of our focused ultrasound transducer. Only in one steering case, we saw axial FWHM 0.4mm over the axial FWHM of FUS focus. The $\overrightarrow{\boldsymbol{T}_{error\_PAM}}$ for most cases was within sub-mm precision. In one case however, the $\overrightarrow{\boldsymbol{T}_{error\_PAM}}$ was over 2mm. This $\overrightarrow{\boldsymbol{T}_{error\_PAM}}$ was observed in lateral axis of around 1.5mm of the imaging transducer. We attribute the increase error in this region to only being able to receive on a sub-aperture spanning -18 to 6mm of the probe for our RCB-PAM sequence due to the way the 192-element array is addressed by our 128-element receiver. The reduced aperture would lead to an expected increase in the focal spot size achievable (on transmit and/or receive) at

the edges of lateral extent of the receive. In all in-vitro study inside the skull, the FWHM was greater than FWHM observed in absence of skull. A study showed that presence of rat skull in the way of FUS can distort and shift FUS focus by as much as 5mm at 1.2 MHz [214]. Another study from our lab showed that both, steering a phased array and skull in the way of focus can result in increase in axial FWHM[187]. Hence, a combination of steering our focus to the edge of the receive aperture and skull in the way FUS focus may be responsible for higher FWHM and an average $\overrightarrow{\boldsymbol{T}_{\boldsymbol{error\_PAM}}}$ over 1 mm.

RCB-PAM overlay on power Doppler image of in-vivo rat brain can reveal brain regions that underwent BBB opening. For our in-vivo BBB opening, the points we chose were 44.6,44.3, and 44.4mm axially and 0.6, 1.3, and 1.9mm laterally for focus 1, focus 2 and focus 3 respectively. In our in-vivo results, the spectral energy in the RCB-PAM map was within the brain in 2 out of 3 foci and was lower and more diffuse in the case when energy was mapped outside of the brain. Our post procedure MRI image showed BBB opening inside the brain in all three dimensions where spectral content in RCB-PAM maps was inside the brain. The opened region of the BBB is coincident with the PAM overlay of focus 1 and focus 2, which span 0-1.6mm laterally (Fig 5.8c). In the third focus, the RCB-PAM map in presence of MBs in Fig 5.6 for focus 3 looks like RCB-PAM map for focus 3 in absence of MBs and have similar spectral intensities. Spectrograms in Figs 5.7a and 5.7b reveal an overall greater wideband content in focus 1 and focus 2 in FUS sonications of MBs but show only harmonics content in focus 3. Focus 3 spectrogram in presence of MBs contain similar content when compared spectrograms in absence of MBs which suggests that MBs may not be present by the time focus 3 was sonicated. In one paper[85] researchers note that after contrast agents, such as MBs, are disrupted by FUS pulses for BBBO opening, the reperfusion kinetics occur on a time scale that can result in incomplete replenishment of the agent between the pulses. In the paper above, after the drop in perfusion at an MI of 0.52 (close to our MI of 0.57), it took 1.2 seconds for the microbubbles to reach 90% of its steady state value. With the highest blood flow velocity of 10mm/s in rat brain[138] and with our chosen sonication scheme, MBs would have moved around 0.1 μm between each focus. Since each focus was around at least 0.5mm apart from each other, MBs did not have enough time to be replaced. Hence, we believe that lack of reperfusion due to high PRF between sonication of each focus, there are no MBs present during the sonication of focus 3 which ultimately resulted in lack of signal in the intended target regions of RCB-PAM map in focus 3.

Values of $\overrightarrow{\boldsymbol{T}_{\boldsymbol{error\_PAM}}}$ is higher in in-vivo procedures which may be due to a combination of shift of FUS focus

and attenuation of receive signal through the skull. The $\overrightarrow{T_{error\_PAM}}$ observed in in-vivo was 2.6 ± 0.89 mm and 2.3 ± 1.02 mm but was less than 2mm in most cases of in-vitro. We attribute these higher $\overrightarrow{T_{error\_PAM}}$ to in-vivo skull (~1mm) being thicker than our in-vitro skull (<1 mm) which could have resulted in attenuation of receive signal and may have also shifted the FUS focus as shown in one study [214] where the focus shifted by as much as 5mm at 1.2 MHz when a rat skull was introduced near the focus of a FUS beam . We believe that the signal was attenuated because, although our intended target was at 44mm axially, the point in the RCB-PAM images with the highest signal was located at 42mm axially, which coincides with the location of the skull. Further MRI analysis confirmed that in fact the BBB opened regions were inside the brain away from the skull.

RCB-PAM overlay on Gd-Contrast MRI T1W MRI image of in-vivo rat brain coincides with BBB opened regions and $\overrightarrow{T_{error\_BBB}}$ show that our targeting is precise. An overlay of PAM data on the MRI BBBO image in Fig 5.8c for focus 1 and 2 also shows that RCB-PAM signals are present in the regions that underwent BBBO. The signals that overlap with BBB opened regions are among the highest magnitude signal. Due limitations posed on to us by reduced aperture of our receive transducer, we calculated the targeting error vector between the BBB opened region and the intended region $(\overrightarrow{T_{error\_BBB}})$ for our in-vivo experiment since this error would be independent of sensitivity and directivity of receive transducer elements and would not be impacted by reduced sub-aperture. The $\overrightarrow{T_{error\_BBB}}$ values for focus 1, focus 2, and focus 3 are 1.1, 1.12, and 1.15mm respectively and is in excellent agreement with other studies that involve in-vivo procedures [215]–[218]. With our FWHM of 2.7x0.6mm, the pixel with BBB opening is within the FWHM opening area.

BBB opening volume achieved here is smaller than BBB opening reported in literature. The BBB opening in this study was observed at peak negative pressure (PNP) of 0.7 MPa which is above than threshold pressure of 0.3-0.45 MPa at 1.5 MHz[219] used for opening BBB in mice. The focal opening volume of 0.21mm3 achieved, however, is less than FWHM focal volume of 0.56 mm3 achieved via our FUS transducer[206] and is also less than BBB opening observed in other studies conducted at similar frequency, lower pressures and lower sonication duration[220], [221]. A peak negative pressure of 0.7 MPa would result in pressures ranging from 0.35 MPa to 0.7 MPa in the FWHM focal volume. Since the rat skull is 2.5-5 times thicker than mice skull[222], it is plausible that the BBB opening spanned less than the FWHM focal volume due to attenuation of ultrasound in the presence of a

thicker skull. Hence, we believe that despite using higher pressures than threshold to open BBB, the presence of thicker skull could have attenuated ultrasound and resulted in smaller focal BBB opening.

A smaller BBB opening enables excellent control over different regions of small animal brains. Of particular interest is drug delivery after FUS mediated BBB opening in small animals. Researchers have delivered chemogenetics to hippocampal regions under MR guidance[204] in small animals. Our system can enhance the applications of such drug delivery by providing an all-ultrasound precise drug delivery to intended regions of brain with limited focal opening. The hippocampal regions in rat[223] span around $70mm^3$ and span around $20mm^3$ in mice[224]. With the ability to generate a small acoustic focus, in conjunction with power Doppler imaging, our methods could open BBB in hippocampal regions with improved spatial selectivity. Another FUS application, neuromodulation, can benefit from our system where precise targeting of intended regions is of utmost importance. Previous studies showed that due to a smaller FUS focus at megahertz frequency, a successful motor activation of the limbs[225], whiskers, and tail[226] can occur with greater specificity. With a focal opening volume of $0.21mm^3$ by our transducer, coupled with imaging, we can further enhance both specificity and spatial selectivity in the cerebral cortex regions of the rat and mice, which have volumes above $100mm^3$ [227], [228]. Overall, an all-ultrasound system can guide, steer, and target specific regions of the brain.

CHAPTER 6: Functional ultrasound detects unique responses to electrical stimulus applied to the hindpaw at varied frequencies in the rat brain[4]

6.1 Introduction

Functional ultrasound (fUS) is a promising technology for non-invasive functional neuroimaging that generates blood flow maps of regions of the brain with high spatiotemporal resolution [138], [139]. fUS blood flow estimates are created by using high frame rate ultrasound to detect echogenic scatterers in blood vessels that supply the brain [138]. During fUS, plane-wave illumination is used to obtain a large field image spanning multiple centimeters. The plane-wave illuminations occur at angles, and they are summed coherently to produce a compounded ultrasound image of a high resolution. The phase shift between scatterers detected in temporally sequential images can be processed to create an estimate of blood flow called power Doppler (PD), which provide a non-invasive estimate of cerebral blood flow that can act as a surrogate for brain activity. The PD flow signal detected by fUS has been linked to neural activity in various animal models such as in rats[134], [145], awake mice [142], [229], non-human primates [230] and in neo-natal applications [143] , but much remains unknown about the sensitivity of fUS to neural activity and differing experimental conditions. One method to help better understand the biological meaning of the information contained in the fUS signal is by performing fUS studies in a well-characterized experimental model. fUS provides similar information as fMRI which is the gold standard method to study somatosensory responses [231], [232] especially during paw stimulation of rat brain [233]–[237] via measuring changes to blood oxygenation level. BOLD fMRI signal is dependent on factors such as choice of anesthesia and stimulation pulse parameters. Anesthesia can not only affect cerebral blood flow and metabolism which can alter hemodynamic response to the stimulation [238], choice of certain anesthetics can cause vasodilation [239]. Stimulation pulse parameters also affect the hemodynamic response. In that, both the frequency of the pulse and width of the pulse can result in recruiting both sensory and proprioceptive inputs [234], [240]–[243].

In this study, we developed methods to acquire fUS signals in response to hindpaw stimulation in rat at two different stimulatory frequency under low level of isofluorane. With fUS, we achieved a spatial resolution of 87μm X 200μm in the imaging plane.

4. Work presented in this chapter is currently being prepared for submission at Scientific Reports.

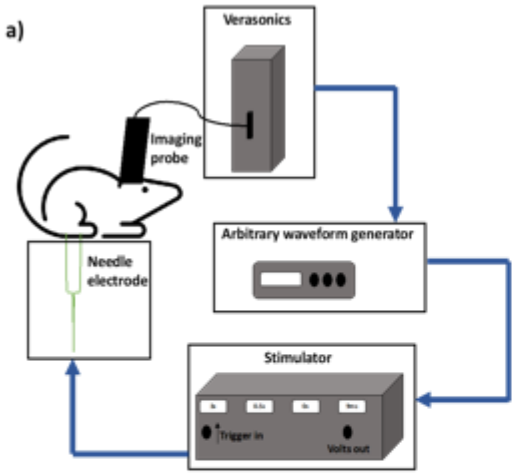

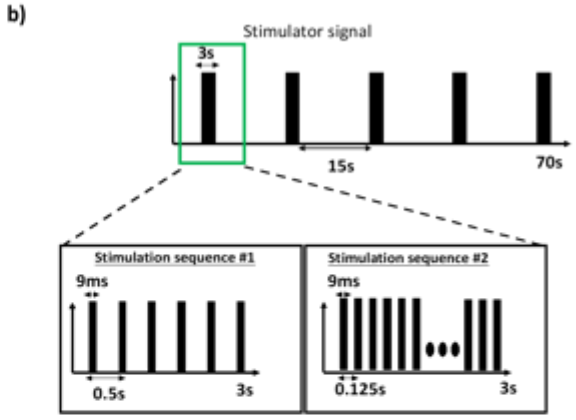

c)

Groups	Number of treatments at 2Hz	Number of treatments at 8Hz
Cohort 1 (Rat # 2)	2	3
Cohort 2 (Rat # 3)	1	1
Cohort 3 (Rat # 1)	1	0
Total number of treatments	4	4

Figure 6.1: Set up figure with stimulatory pulse sequences: a) A 9 MHz imaging probe is mounted on top of rat head. The imaging probe is attached to a 3-D axis stage such that it can be positioned at bregma-1mm. The imaging transducer is operated via Verasonics research machine. Verasonics sends trigger to arbitrary waveform generator 2.5s after imaging starts and sends trigger every 15s thereafter. Arbitrary waveform generator then sends the 1 cycle at 8Hz pulse to the stimulator which then sends electrical stimulation to the needle electrode which is attached to the rat hindpaw. b) The electrical stimulation signal send to the needle electrode via stimulator is either at 2Hz (stimulation sequence #1) or 8Hz (stimulation sequence #2). A 3s stimulation is sent every 15s for a total of 70s. The total duration of one stimulus is 9ms. c) There were in total 3 rats that underwent treatment at either just 2Hz or at both at 2Hz and 8Hz stimulatory frequencies. In total, there were 4 treatments at 2Hz and 4 treatments at 8Hz.

The spatial resolution was achieved with a penetration depth of 2cm in a very short acquisition time (2ms). We used the same functional ultrasound dataset and subjected them to ULM using an open-source tracking method [146]. We were able to see vasculature, in both, superficial and deeper region and this helped us compare our activation regions accurately with the rat brain atlas.

6.2 Materials and Methods:

6.2.1 Animals handling to make imaging window on the animal skull:

All procedures were reviewed and approved by the Vanderbilt University Institutional Animal Care and Use Committee. Animals arrived at least 2 weeks before the experiment. We anesthetized male Sprague-Dawley rats (N=3, 6 weeks old) using 2.5% isofluorane and performed catheterization in the femoral vein to enable MBs injection. Craniotomy was performed thereafter where a micro drill steel burr was used at low speed to remove layers of the bone skull. The craniotomy window was approximately 2cm x 2cm. During the drilling procedure, we cooled the skull with saline to reduce swelling and edema of skull cortex.

6.2.2 Microbubble fabrication

We produced lipid-shelled MBs in-house following the methods described in Borden et al 2005 [208]. Briefly, we combined and dried into film 90mol% 1,2-distearoyl-sn-glycero-3-phosphocholine (DSPC) and 10mol% 1,2-distearoyl-sn-glycero-3-phosphoethanolamine-N-[amino(polyethylene glycol)-2000] (DSPE-PEG2k) and resuspended it to 2.5mg/ml in MB buffer solution (80% v/v of 0.9% NaCl, 10% propylene glycol [1,2-propanediol], and 10% glycerol). We degassed the solution and filled the head space with F10C4 (FluoroMed, Round Rock, TN, USA). We repeated this process for a total of 3 times. The bubble solution was agitated using a VialMix (DuPont, Wilmington, DE, USA) for 45 seconds to form MBs prior to experimentation. DSPC and DSPE-PEG2k was purchased from Avanti Polar lipids (Alabaster, AL, USA).

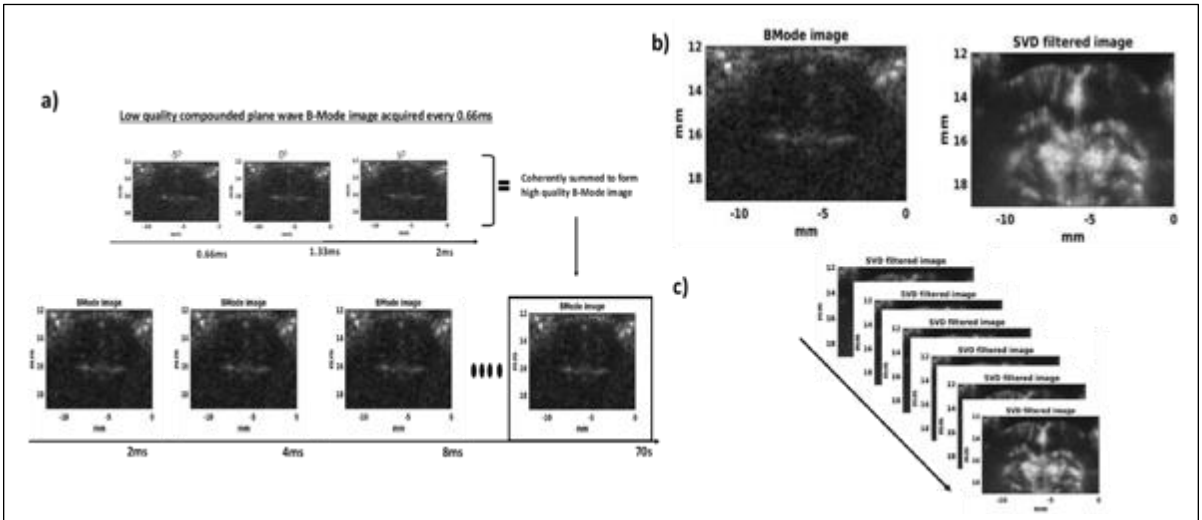

Figure 6.2: Functional ultrasound image processing steps: a) Low quality B-Mode images reconstructed from plane waves illuminated at -5^0 ,0^0 and 5^0 at 1500 Hz are summed coherently to form one high quality B-Mode images. In a time span of 70s, a total of 35,000 high quality B-Mode frames are captured at an effective frame rate of 500Hz.b) These high-quality B-Mode images are filtered using singular value decomposition method. First few singular values, which correspond to tissues, are eliminated and signal from microbubbles and red blood cells are preserved. The SVD filtered images are summed to form power Doppler images. c) For calculating the hemodynamic response, 1s of SVD filtered image is summed with 0.9s of overlap. These power Doppler images are also used to calculate activation maps to inform us of regions with increased blood flow during stimulation.

6.2.3 Animal anesthetization and probe placement

We anesthetized animals using isofluorane using 1.5% isofluorane for maintenance but reduced the isofluorane to 0.5% during stimulation and performed catheterization in the right femoral vein of the rat to enable microbubble injections. A layer of ultrasound gel was applied on the imaging window and animal was then put in a stereotactic frame. A 192-element transducer operating at 9 MHz was placed on the head of the animal and we coupled it with ultrasound gel (Fig 6.1a). Initially, a real time B-Mode imaging was used to guide the placement of the probe in the field of view. Using sutures at the bregma on rat skin, we moved the imaging transducer to bregma-1mm position using a 3D motion axis stage. Bregma-1mm position in the rat brain consists of somatosensory regions (S1HL and M1 and M2) that activate due to hindpaw stimulation. The body temperature of the rat was maintained using a heating pad that was set at 42oC . We inserted needle electrode on the right hind paw to alternatively induce electric stimulation and allowed the hind paw to rest for 5 mins between each stimulation. A 50uL bolus injection of MBs was administered before each imaging sequence and acquisition was started 10s thereafter. Our first acquisition was a control acquisition where no stimulations were delivered. After our first acquisition, we delivered

a train of five stimulations (6 pulses at 2 Hz of 9ms width for n=4 or 24 pulses at 8 Hz of 9ms width for n=4) for 3s separated by 12 s off period to recover to baseline during our subsequent acquisitions (Fig 6.1b and Fig 6.1c). These stimulations were repeated for total of 70s (3s on 12s off). Out of 3 animals used, 2 animals were stimulated at both 2Hz and 8Hz whereas n=1 was stimulated only at 2 Hz. For comparison between the effects of stimulation on the blood flow, data from two animals that were stimulated at both frequencies were used. The stimulation acquisitions were divided with control acquisition to account for signal decay due to bolus microbubble injection.

6.2.4 Ultrafast Doppler imaging acquisition sequence

We performed functional ultrasound (fUS) imaging based on compounded plane-wave ultrasound imaging. First, a real time vascularization map was obtained which verified microbubbles in the system. For real time vascularization map, 3 compounded planar ultrasonic waves (-5,0,5) were used and summed to form one summed compound frame (described below). These real-time maps refreshed at 50 Hz. Once we confirmed the MBs injection using the vasculature map, we started our fUS imaging sequence. Our fUS imaging sequence comprised of using three compounded plane waves (-5,0,5, PRF = 1500Hz) (Fig 6.2a). We recorded the backscattered echoes and used Verasonics for offline reconstruction of RF data into delay-and-summed in-phase and quadrature (IQ) images. We summed 3 IQ images corresponding to each angled plane wave to produce 35,000 B-mode images (stored as 140 of 250 B-mode images) over a time period of 70s at a frame rate of 500 Hz. During image acquisition process, the Verasonics triggered the arbitrary waveform generator set to trigger the electrical stimulator to stimulate 3s every 12s starting 2.5s into acquisition.

6.2.5 Creating PD images and vascular maps

We acquired and reconstructed the vascular map and activation maps using Verasonics with off-line processing in MATLAB. We filtered the backscattered signals to distinguish the moving red blood cells and microbubbles from the static tissue in Fig 2b. For each stack of 250 frames, we eliminated the first frame due to presence of an artifact in the image. In order to recover signals from moving red blood cells and microbubbles, we applied a singular value decomposition method on stack of fUS images [138], [229]. We eliminated the largest Eigenvalues to filter the slowest variations in power Doppler signal which corresponded to tissue signal. We performed SVD filtering on all 35,000 images at a time and eliminated first 300 eigenvalues. We then subjected

these SVD filtered stack of images to a 3rd order Butterworth high pass filter with a cut off frequency of 50 Hz to further remove tissue and motion artifact coming from the skull. We then summed each stack of 250 images to obtain a power Doppler (PD) image.

6.2.6 Creating activation maps of the entire bregma-1mm plane and calculating the hemodynamic response near the cortical regions

We created activation maps of the entire bregma-1mm plane by calculating temporal correlation between stimulation window *s(t)* by the hemodynamic response *PD(x,y,t)*.

To achieve this, we first normalized the power Doppler data and the stimulus with zero means:

$$\overline{PD}(x,y,t) = \frac{PD(x,y,t) - \frac{1}{n_t}\sum_t PD(x,y,t)}{\sqrt{\sum_t (PD(x,y,t) - \frac{1}{n_t}\sum_t PD(x,y,t))^2}}$$

$$\bar{s}(t) = \frac{s(t) - \frac{1}{n_t}\sum_t s(t)}{\sqrt{\sum_t (s(t) - \frac{1}{n_t}\sum_t s(t))^2}}$$

We then computed the Pearson's correlation in each pixel of the image. The output of following function gave us correlation map:

$$c(x,y) = \frac{\sum_t \overline{PD}(x,y,t)\,\bar{s}(t)}{\sqrt{\sum_t \overline{PD^2}(x,y,t)\sum_t \bar{s}^2(t)}}$$

We considered pixels with c > 0.25 as significantly activated in our study. We selected this value by selecting a P-value threshold of 0.05. We converted the P-value into corresponding *z*-score using a two-tailed t-test (z=2.8) similar to other functional ultrasound studies [142], [244]. Using Fisher's transform, we found the threshold of c > 0.25. We then chose pixels greater than the threshold in the cortical region to calculate change in power Doppler signal, since our regions of interest were S1HL, M1 and M2. We calculated the temporal mean of fUS images with a sliding window of 500 frames and overlap of 490 frames and used the mean images to calculate changes in cerebral blood volume (hemodynamic response) relative to stimulation blocks. We normalized temporal fluctuations in signal as a result of functional stimulations with 40ms of baseline signal and presented is as power Doppler percent (PD%).

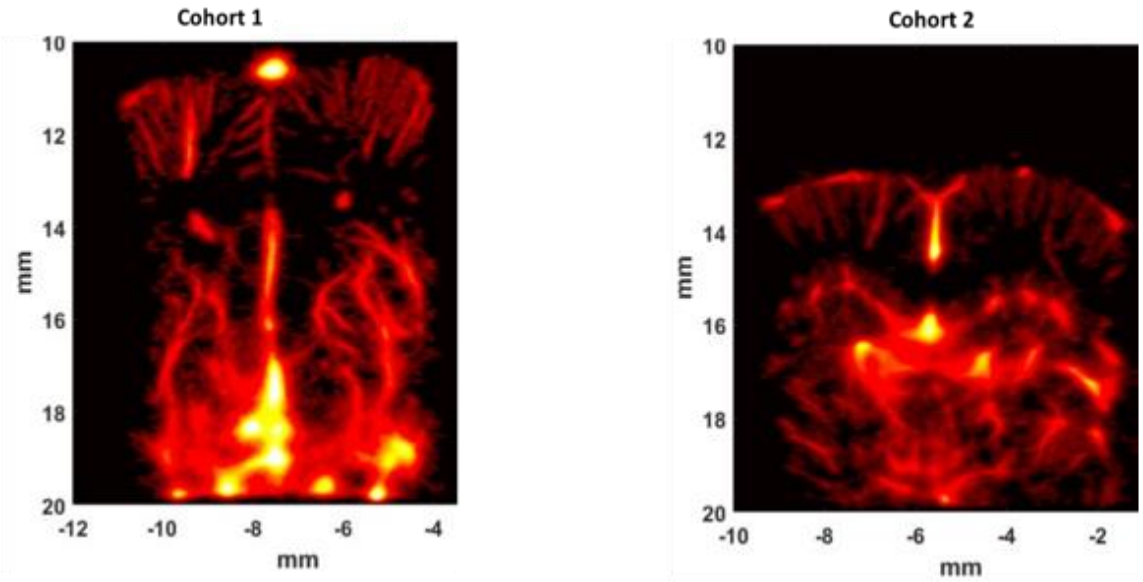

Figure 6.3: Ultrasound localization microscopy is able to localize vasculature near the cortex in both cohorts. Cohort 1 had a smaller craniotomized region than cohort 2. Being able to localize the cortex also helped in identifying somatosensory cortex and accurately pin-point regions undergoing activation after comparing it with the rat brain atlas.

The hemodynamic curve was further used to calculate duration of PD% which was above the baseline when stimulation was on and was computed as the difference between the time point at which the response started going above baseline after stimulation turned on and time point at which response got back to baseline. Additionally, hemodynamic response was also used to calculate the time difference between occurrence of one peak to another during the stimulation on period and this value represented peak-to-peak time.

6.2.7 Ultrasound localization microscopy (ULM)

We used the control frames from cohort that underwent both 2Hz and 8Hz treatment to create ultrasound localized images. We used open-source software to create these images [146]. Briefly, we performed SVD filtering to high frame RF data and removed the first 30 eigenvalues from each block of 250 frames and then applied a bandpass filter between 25 and 125 Hz to the SVD data. The local maxima for highest 60 particles were calculated from SVD filtered data and 5x5 pixel image around local maxima was then subjected to radial symmetry subwavelength localization method where gradient of that 5x5 pixel image pointed towards the microbubble position. In this manner, we localized microbubble with subwavelength precision. Hungarian algorithm was then used to track positions of these particles from one frame to another. In that, the distance from each particle to all

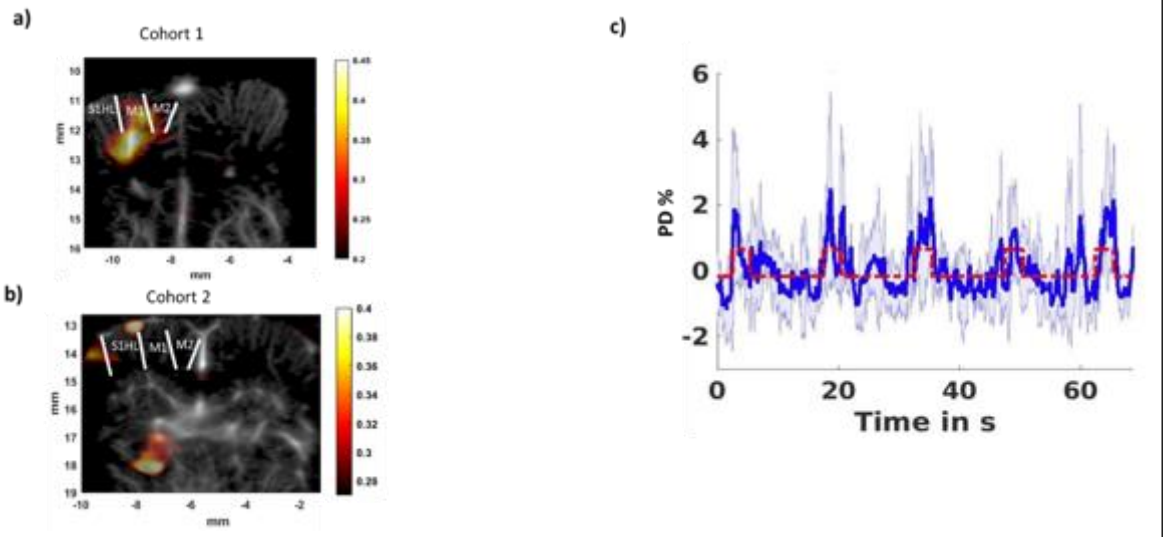

Figure 6.4: Activation maps and hemodynamic response at stimulatory frequency of 2Hz a) Activation maps were overlayed on SVD filtered image of cohort 1 to show the regions that were activated due to stimulation. Somatosensory regions (S1HL) were activated in addition to motor regions (M1) since the pixels in those regions are over the threshold coefficient value of 0.25 .b) Activation maps were overlayed on SVD filtered image of cohort 2. For cohort 2, S1HL regions were activated since the coefficient in those regions were greater than 0.25. We did not see any motor cortex activation. c) This graph is a mean with standard deviation hemodynamic response of 4 studies. Hemodynamic response for each study was calculated by choosing the regions around highest correlation value and computing its intensity temporally. The hemodynamic response was normalized with respect to the baseline and represented as % change in power Doppler signal.

particles in the subsequent frame was calculated and optimal pairing of particles from one frame to the subsequent frames was computed by minimizing the total squared distance. A track was created if this minimized distance was up to 2 pixels. We paired together successive position of these tracks for entire 70s of data collected and interpolated it for 10 times the resolution. Thus, by accumulating large number of tracks, interpolating it 10x the original resolution, and rendering it with power law compression, we reconstructed vascular maps from RF data that were obtained after a bolus MBs injection.

6.3 Results

6.3.1 Ultrafast Doppler scan and ULM after craniotomy

Ultrafast Doppler sequence using the Verasonics research scanner enabled us to acquire Doppler frames at 500Hz. We can see that SVD filtering can reveal vasculature in the brain in the power Doppler image, which is otherwise not visible in the B-Mode in Fig 6.2b. Figure 6.2b also is an example of power Doppler image which shows that we can see vasculature as deep as 15mm. Furthermore, ultrasound localization microscopy can reveal superficial and deeper vasculature. In Fig 6.3a, we see that after ULM, the vasculature near the cortex and in the deeper regions near the thalamus are visible, which were otherwise not visible in just the power Doppler image.

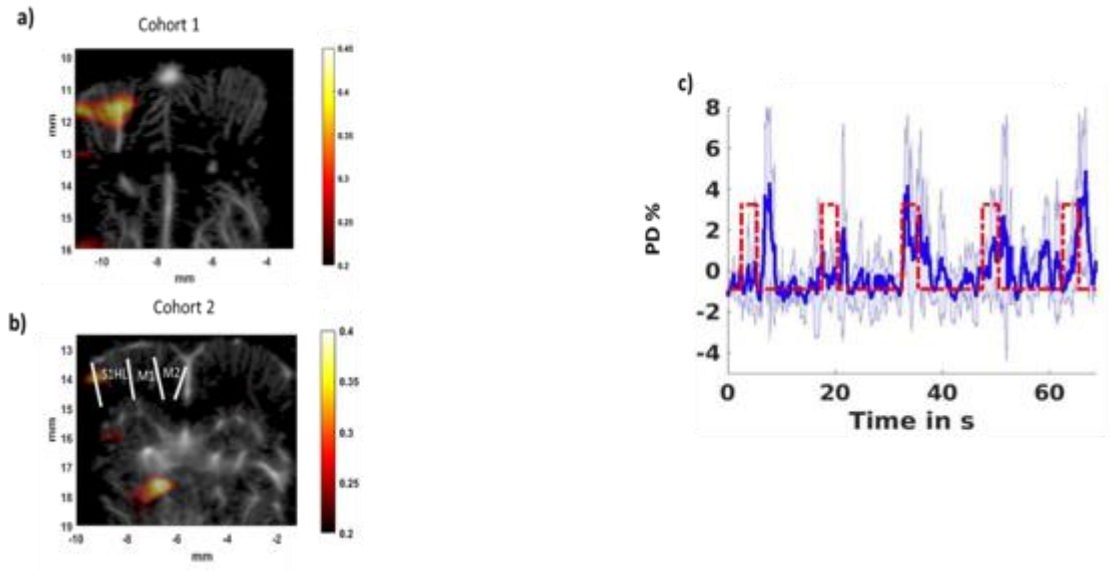

Figure 6.5: Activation maps and hemodynamic response at stimulatory frequency of 8Hz a) Activation maps were overlayed on SVD filtered image of cohort 1 to show the regions that were activated due to stimulation. Somatosensory regions (S1HL) were activated in addition to motor regions (M1) since the pixels in those regions are over the threshold coefficient value of 0.25 .b) Activation maps were overlayed on SVD filtered image of cohort 2. For cohort 2, S1HL regions were activated since the coefficient in those regions were greater than 0.25. We did not see any motor cortex activation. c) This graph is a mean with standard deviation hemodynamic response of 4 studies. Hemodynamic response for each study was calculated by choosing the regions around highest correlation value and computing its intensity temporally. The hemodynamic response was normalized with respect to the baseline and represented as % change in power Doppler signal.

6.3.2 Stimulatory frequencies of 2 Hz and 8Hz result in statistically significant activations in both S1HL region and M2 regions of somatosensory cortex of the rat

We inferred the regions of activation by carefully comparing vasculature present in ULM images with Sprague Dawley rat brain atlas and outlining it on activation maps overlayed on super resolution images in Figs 4 and 5 [245]. In cohort 1, stimulatory frequencies of 2 Hz stimulated both the motor cortex and S1HL regions in the rat in Fig 6.4a as depicted by the activation map. For cohort 2, the activated regions were restricted to S1HL in Fig 6.4b. In both these activation maps, the correlation coefficient was well above 0.25 (0.45 and 0.4 respectively), which informed us that these activation pixels were significant. At stimulatory frequencies of 8 Hz as well, we found

that activation in the correct side of the brain. Similar to stimulatory frequencies of 2 Hz, both S1HL and motor cortex regions of the rat brain saw significant activated pixels in Fig 6.5a but the signal was mostly confined to S1HL regions in Fig 6.5b.

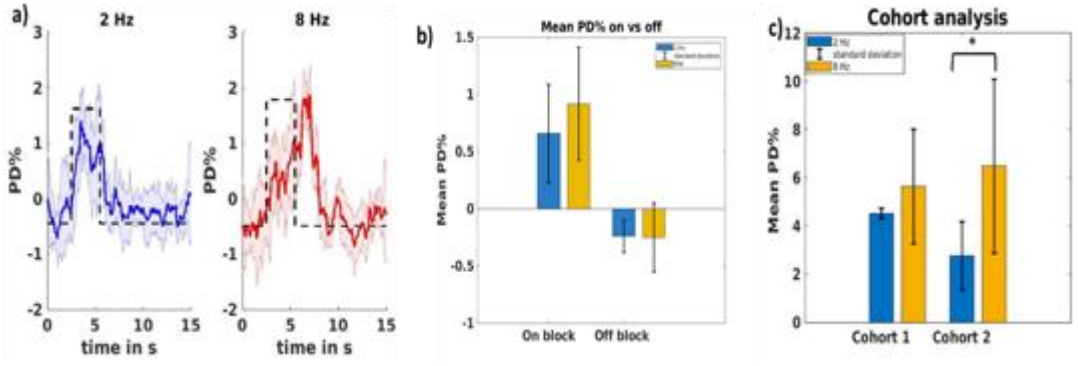

Figure 6.6: Comparison of power Doppler % signal between two stimulatory frequencies. a) A mean power Doppler signal (dark blue line) with standard deviation (light blue line) of all 5 stimulatory instances for all 70s of mean hemodynamic response at 2Hz show an overall increase in signal when stimulation is turned on from 2.5-5.5s. This graph also shows that the response goes back to baseline after the stimulation is stopped. Similar trend was seen when mean was taken for 5 stimulatory instances of all 70s of 8Hz hemodynamic response (dark red line represents the mean and light red line is the standard deviation). This time however, the peak was delayed and was reached at 7s. However, there was an increase in signal when stimulation was on. The signal started to drop after it reached peak. At that time, the stimulation was turned off. b) Mean power Doppler comparison of on and off instances at 2Hz and 8Hz showed increased PD% during the on instance than in off instance. At 2Hz, the PD% during on time was PD% 0.66±0.4 and PD% of -0.24 ±0.14 during the off period. The PD% on value and off value for 8Hz was 0.9±0.5 and -0.25 ±0.3 respectively. c) . In cohort 1, at 2Hz stimulatory frequency, a mean PD% of 4.5±0.2% was observed whereas in cohort 2 a mean PD% of 2.8±1.4% was observed. At stimulatory frequency of 8Hz, a mean PD% of 5.7±2.4% in cohort 1 and 6.5±3.6%.in cohort 2 was observed.

6.3.3 Mean hemodynamic response curve show fluctuations in power Doppler signal when stimulation is on

We created activation maps for all 8 trials to calculate change in power Doppler signal for both at 2Hz and 8Hz. A mean of 4 hemodynamic responses to stimulations at 2Hz in the activated regions in Fig 6.4c show fluctuations in blood flow where there is a rise in blood flow when stimulation is on for 3s. In Fig 6.6a, we plot a mean power Doppler signal within 5 stimulation events of Fig 6.4c. The plot shows that there is a rise in signal as the stimulation turns on, but the signal goes back to baseline shortly after stimulation is turned off. We found that

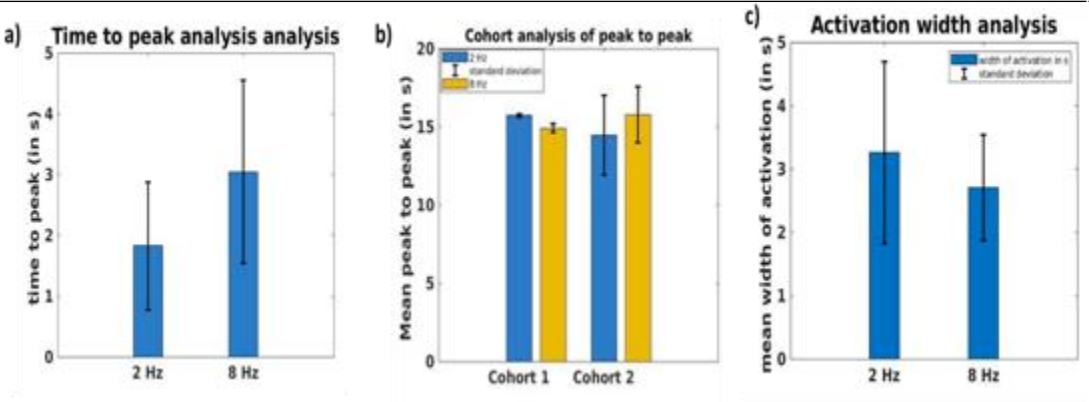

Figure 6.7: Comparison of power Doppler peak time and activation width analysis between 2Hz and 8Hz. a) Time to peak analysis of the mean hemodynamic response revealed that it took 1.8 ±1s for signals to reach the peak after stimulation is on at 2Hz. The time to peak value at 8Hz was 3±1.5s. b) A mean peak to peak analysis for cohorts revealed that one peak was on average 15.7±0.3s away from another peak at 2Hz and 14.9±0.28s at 8Hz. For cohort 2, one peak was on average 14.5±2.5s away from another peak at 2Hz and 15.8±1.8s at 8Hz. c) The width of activation pulse at 2Hz was 3.25±1.4s whereas the width of 8 Hz signal was 2.7±0.8s

mean time to peak at 2Hz was 1.8±1s (Fig 6.7a). A mean of 4 hemodynamic response to stimulations at 8Hz in Fig 6.5c show rise in PD% when the signal is turned on but in ¾ cases, the peak comes after the stimulation has ended. The delay in peak is also apparent in Fig 6.6a where mean PD% of hemodynamic signal in Fig 6.5c show a peak after stimulation is over. The peak is reached at 7s, which 1.5s after stimulation is over and that the mean time to peak at 8Hz was 3±1.5s (Fig 6.7a).

6.3.4 Mean PD% during on period was higher than during off period for 2Hz and 8Hz

Further analysis revealed that mean power Doppler% signal during on period at 2Hz was 0.66±0.4 and PD% during the off period was -0.24 ±0.14 in Fig 6.6b. The PD% on value and off value for 8Hz was 0.9±0.5 and -0.25 ±0.3 respectively in Fig 6.6b. In cohort 1 of Fig 6.6c, mean PD% at 2Hz was 4.5±0.2% whereas at 8Hz this value was higher at was 5.7±2.4% but was not found to be statistically significant. In cohort 2, mean PD% at 2Hz was 2.8±1.4 and at 8 Hz was found again to be higher at 6.5±3.6%. In cohort 2, there was statistically significant differences ($p<0.05$) between PD% at 2Hz and at 8Hz. We found that the width of hemodynamic response to stimulations at 2Hz in Fig 6.6c lasted for 3.25±1.4s and the width hemodynamic response to each stimulation at 8Hz lasted for 2.7±0.8s (Fig 6.7c).

6.4 Discussion:

Stimulatory frequencies of 2 Hz produced smaller peaks than 8 Hz. The stimulatory frequency of 2 Hz produced a mean PD% of 4.5±0.2% in cohort 1 and 2.8±1.4% in cohort 2 whereas stimulatory frequency of 8 Hz produced a mean PD% of 5.7±2.4% in cohort 1 and 6.5±3.6%.in cohort 2. In both cohorts, 8 Hz produced larger peaks than 2 Hz. In cohort 2, these peaks were on an average double than at 2 Hz. We performed a Mann-Whitney U test and found that there was no statistical significance between PD% in 2Hz and 8Hz in cohort 1 but there were statistically significant differences ($p<0.05$) between PD% in 2 Hz and 8Hz in cohort 2. These results are in line with what has been reported in literature where in one study [242], researchers wanted to find the optimal stimulation frequency for short stimulations (<10s) vs long stimulation duration (30s), and found that BOLD responses in rat forepaw stimulation under isofluorane anesthesia was frequency dependent. When the researchers conducted further analysis, they found a BOLD response of around 1.5% at 3Hz but this value nearly doubled to 2.9% at 12Hz and found these results to be statistically significant. In this study, researchers concluded that 8-12Hz is an optimal stimulus frequency for short stimulation durations (<10s) whereas 6-8Hz is optimal for 30s stimulation.

Stimulatory frequencies of 2 Hz had wider width of the stimulus than 8 Hz. When we compared the width of activated signal in response to 2 Hz and 8 Hz electrical stimulus, we found that 2 Hz signal lasted for approximately 3.25±1.4s whereas the width of 8 Hz signal lasted for 2.7±0.8s. However, these results were not found to be statistically significant. These results are in agreement with what has been previously published [242] where researchers found that when the rat forepaw is stimulated for 30s at 1.5 Hz, the full width half max of the response was around 18s whereas when it was stimulated at 6 Hz the FWHM dropped to around 12s. The researchers suggested that this may be due to cortical neurons becoming increasingly adaptive to highly repeating strong stimuli which would result in decrease activity over the stimulus period. Hence, they observed that the neural activity and BOLD % was initially larger for high stimulus frequency, but neural responses due to high stimulus frequency caused duration of stimulus period to be shorter. Our work suggests that blood flow detected by functional ultrasound

is sensitive to these fluctuations.

Mean time from one peak to another peak for both 2 Hz and 8 Hz in both cohorts were close to actual time between stimulations. The mean peak to peak time in Fig 6.6b in cohort 1 at 2 Hz and 8 Hz were 15.7±0.3s and 14.9±0.28s respectively. In cohort 2, the mean peak to peak at 2 Hz and 8 Hz 14.5±2.5s and 15.8±1.8s. Although these values are very close to the actual time between stimulations, there were instances where the stimulation peak occurred after the stimulation pulse. Peaks that occur after stimulation pulse ended resulted in mean peak to peak time be either lower or higher depending on if the next peak came during or after the stimulation pulse. In Fig 6.5a, we also observed that the peak at 2Hz was achieved during the on pulse but was delayed by 2s relative to the stimulus onset at 8Hz. Such delay in time to peak has been observed in fMRI studies when it can take about 15s [234] to reach a peak BOLD signal during a 45s activation forepaw electrical stimulation at 3 Hz. In yet another study, it took up to 6s to reach a peak BOLD signal when rat forepaw was simulated at 3 Hz for 30s [242].

Activations of somatosensory regions and subcortical regions agree with literature. We observed increased somatosensory response when the stimulation on for both 2Hz and 8Hz stimulation. After consulting with rat brain atlas, we saw activation in primary motor cortex M2 region and primary sensory hindpaw S1HL in cohort 1 for both stimulatory regions as shown via sensory motor cortex outlines in Figs 6.4 and 6.5. In cohort 2, the regions of activation were only present in S1HL for both stimulatory frequencies and these regions were larger for 2 Hz than compared to 8Hz. These activated regions are in agreement with what has been reported in functional ultrasound literature [134]. Similar regions were activated in an BOLD fMRI study in rats when rats received stimulation in their hindpaw for 10ms at 8 Hz frequency [239] where researchers noted signals present in S1HL and M1 regions. In cohort 2, some pixels with correlation coefficient > 0.25 were also present near subcortical structures, such as thalamus, which has previously not been reported in functional ultrasound literature. While a vast majority of fMRI literature with stimulation duration of less than 0.3ms do not show activation of subcortical regions during forepaw or hindpaw stimulation, [234], [246]–[248], there have been few studies where activation of subcortical regions in fMRI studies have been linked to pulse parameters such as pulse duration and frequency [234], [239]. It has been shown in literature that changing pulse duration from 0.3ms to 10ms alone can alter optimal electrical stimulatory frequency at which maximum BOLD response occurs from 3Hz to 8Hz [240]. Furthermore, under isofluorane

anesthesia, a combination of specific stimulus pulse durations and frequencies, 10ms electrical stimulus at 8Hz, can result in BOLD responses in cortical and subcortical areas of rat thalamus in addition to somatosensory areas [239]. Similar effects were seen under α-chloralose [234] anesthesia where activations were observed in thalamus regions in response at 3Hz stimulation. In both studies, it was believed that both sensory and proprioceptive pathways were recruited that enabled cortical and subcortical activations. These parameters and observations are not far from our stimulation width (9ms) and frequency (2Hz and 8Hz) which also resulted in power Doppler signal in the thalamus.

6.5 Conclusion

Functional ultrasound is being widely used to study blood flow in response to external stimulations and provides similar information to fMRI but from blood flow instead of BOLD signal. The regions of activation and increase in BOLD signal is dependent on factors such as choice of anesthesia and stimulation pulse parameters. Anesthesia is found to directly affect cerebral blood flow and metabolism which can alter hemodynamic response to the stimulation [238]. Stimulation pulse parameters also affect the hemodynamic response. In that, both the frequency of the pulse and width of the pulse can result in recruiting not only sensory but proprioceptive inputs [234], [240]–[243]. For instance, a pulse width greater than 1ms has shown BOLD signal in thalamus which is otherwise not reported in vast majority of fMRI literature. Pulse widths of 0.3ms only reported BOLD induced activations of sensory motor cortex [241], [246], [249], [250]. In this study we wanted to demonstrate sensitivity of fUS to frequency-specific hindpaw stimulation at a fixed pulse width in a rodent brain. We observed that stimulatory frequency of 2Hz produces sustained but lower magnitude of functional response whereas stimulatory frequency of 8Hz produces shorter but higher magnitude of functional response. Additionally, we also observed recruitment of proprioceptive pathways which resulted in activations of thalamus. Overall, we demonstrate that fUS can detect unique responses to electrical stimulations of different frequencies and can serve as a complimentary technique to fMRI.

6.6 Study Limitations

In our study, we performed a craniotomy in a terminal procedure to minimize attenuation of the received ultrasound signal. However, transcranial functional ultrasound in younger rat and mice models have been previously reported in literature [134], [229], [251]. Hence this procedure can be made non-invasive by performing transcranial functional ultrasound.

Another limitation of this study is that the functional ultrasound was performed in only one 2-D plane. Bregma-2mm position also contained S1HL, M1 and M2 regions. But the signal from bregma-2mm were not captured simultaneously as bregma-1mm position. Capturing signal from both slices would give us more information about activation characteristics. This limitation can be overcome by using a 3D imaging transducer than can capture functional ultrasound signal from multiple slices [140], [142], [229].

Additionally, via the help of super resolution image and rat brain atlas, we were able to infer locations of activations. Future work will include combining rat brain atlas with super resolution imaging, which have been reported in literature for mice studies, such that the rat brain atlas can be overlayed on the super resolution image and activation maps to identify regions of activation more accurately.

CHAPTER 7: Applications and future directions

Acoustically active particles have the potential to improve ultrasound therapy and imaging outcomes. FUS in conjunction with microbubbles are being used to open blood brain barrier and deliver chemotherapy for brain tumor application. FUS in conjunction with nanoparticles are being used for precise neuromodulation application. Combining microbubbles with ultrasound imaging has helped many researchers study small animal brains, non-human primate brains and neo-natal brains. Combining FUS with acoustically active particles and pairing with ultrasound imaging with acoustically active particles, targeting can be achieved without requiring any MRI. The combination of targeting FUS using imaging ultrasound can open door to cause neuromodulation and studying its effects all with one ultrasound machine setup.

7.1 Summary of Key Findings:

Chapter 3 presented methods to use acoustically active particle, phase shift nanodroplets, to enhance ablation volume and ablation efficiency with minimal off-target heating. Pressure field simulations were performed to create desired single focus and multiple foci sonications in egg-white acrylamide phantoms at constant power. While performing FUS ablation on phantoms, MRI thermometry was used to monitor changes in temperature and ablated volume during the heating pulse. It was found that phantoms without PSNDs saw only 7^0C of heating at the focus whereas phantoms with PSNDs saw a temperature rise over 30^0C. The surface temperature in both phantoms with and without PSNDs were minimal and no more than 5^0C. The volumetric ablation was only observed in phantoms with PSNDS. In that, the greatest volumetric ablation was seen in multiple foci pattern followed by single foci pattern at the natural focus. The regions were more contiguous overall in multiple foci pattern than in single foci pattern.

Chapter 4 presents my original work where I investigated the safety of nanoparticles for neuromodulation application where we studied echoes originating from sonicating propofol loaded nanoparticles. We flowed either nanoparticles diluted in saline or just saline (as control) in cellulose tube and sonicated them with FUS at MI $\geq$ 1.4. We were able to create passive acoustic maps in our first set of experiments at MI of 2.2 using a linear imaging array. Detailed analysis of the RF data revealed a wideband content with subsequent ultra-harmonic content. In our second set of experiments, we controlled the handling and temperature of nanoparticles and we observed no

wideband activity from the particles until MI of 3 but wideband activity was not seen in saline. The ultra-harmonic content prevailed and was seen in nanoparticles at MI ≥ 1.8 but was not seen in saline until MI of 2.2. Overall, we were able to evaluate the safety of using these particles for neuromodulation activity and observed that ultra-harmonic content occurs at MI ≥ 1.8, which is within the range that tissues cavitate as well. The nanoparticles are shown to release drugs at lower MI than 1.8 and presumably do not release drugs due to cavitation effects.

Chapter 5 presents my original work where I combined microbubbles with focused ultrasound (FUS) and ultrasound imaging to open blood brain barrier under image guidance. We developed methods to steer FUS array, with axial FWHM of 2.7mm, using a 2D power Doppler image to guide the FUS focus to intended targets to open BBB. We first registered the FUS transducer with the imaging transducer with TRE of 0.5mm. We then developed methods to filter tissue signal from ultrasound images to reveal vasculature in the rat brain and create power Doppler image from the filtered ultrasound images. We then combined both the transducer in a manner such that clicking on the power Doppler image would appropriately steer the FUS transducer to sonicate at that regions and open BBB. During the BBB opening procedure, we used ultrasound imaging transducer to record receive echoes at high frame rate to reconstruct robust capon beamforming passive acoustic maps. We overlayed these PAM maps onto the BBB opened MRI image and found that the regions of high intensity of PAM maps coincide with BBB opened regions with millimeter (1.2mm) scale precision.

Chapter 6 presents my original work where I combined acoustically active particles with ultrasound imaging at high frame rate to study the change in blood flow in the rat brain brought on by electrical stimulation of the rat hindpaw 2 different stimulatory frequencies of 2Hz and 8Hz. I developed methods to image rat brain at 500 Hz frame rate and subjected them to SVD filtering and high pass filtering to remove static tissue signal. I, then, summed the filtered frames after applying moving average filter and correlated them with stimulation signal to make activation maps. I used activation maps to create hemodynamic response. Hemodynamic response at 2Hz had lower change in signal, represented as PD%, when compared to 8Hz but the activation width of 2Hz was greater than 8Hz, probably due to neural adaptation to the response. These outcomes are in line with what has been reported in literature when somatosensory stimulations were carried out in rat and hemodynamic response was measured using fMRI. In this chapter, I showed distinct hemodynamic responses at different stimulatory frequency.

7.2 Ongoing work and Applications

The work presented here has been a part of ongoing tumor vasculature imaging study. High frame rate imaging is being used to study tumor vasculature growth since the tumor implantation to animal sacrifice. The power Doppler images are used to quantify vasculature present in the image.

High frame rate imaging, in 2D, is also being translated to 3D imaging where planar images are gathered during tumor growth to quantify vasculature in a 3D plane over time. High frame rate imaging is also being performed on hydrogel plugs implanted into mice. These plugs eventually grow vasculature and power Doppler imaging will be an important tool to study this growth in vasculature.

Super resolution imaging is currently being explored in a transcranial setting where lower imaging frequencies (5MHz) are used to create vascular map of rat brain.

7.3 Future applications and directions

Power Doppler guided FUS technology can be extended for the use of drug delivery after BBB opening or to cause neuromodulation using acoustically active particles. With a focal opening volume of $0.21mm^3$ by our transducer, we have an excellent control over different regions of small animal brains. Of particular interest to us is drug delivery after FUS mediated BBB opening in small animals. Literature notes researches have delivered chemogenetics to hippocampal regions under MR guidance[204] in small animals. An all-ultrasound system designed in this dissertation can enhance the applications of such drug delivery by providing precise drug delivery to intended regions of brain with limited focal opening. The hippocampal regions in rat[223] span around $70mm^3$ and span around 20mm3 in mice[224]. With the ability to generate a small acoustic focus, in conjunction with power Doppler imaging, our methods could open BBB in hippocampal regions with improved spatial selectivity. Combined with ultrasound localization microscopy, ultrasound imaging could be used to verify BBB opened regions and make USgFUS a self-sufficient modality that can target, open, and detect BBB opened regions all with one system.

Another FUS application, neuromodulation, can benefit from our system where precise targeting of intended regions is of utmost importance. Previous studies showed that due to a smaller FUS focus at megahertz frequency, a successful motor activation of the limbs[225], whiskers, and tail[226] can occur with greater specificity. With our transducer, coupled with imaging, we can further enhance both specificity and spatial selectivity in the cerebral

cortex regions of the rat and mice, which have volumes above $100mm^3$ [227], [228].

Furthermore, power Doppler guided FUS system can also be used in conjunction with ultrasound gated nanoparticles, such as propofol-loaded nanoparticles. With small and precise focusing, these nanoparticles can be sonicated using FUS to release propofol and cause neuromodulatory effects in the desired regions. Power Doppler guided FUS and high frame rate imaging can be combined to study the effects of BBB opening on somatosensory regions using an all-ultrasound system. Prior studies using fMRI have shown that opening BBB can affect the blood flow and activation of somatosensory cortex[87] and this can be replicated using the power Doppler guided FUS systems.

This technology can be extended using a 3D imaging ultrasound array [140]. Using small animal brain maps [229], 3D power Doppler images can be overlayed on top of animal brain maps to identify desired regions of treatment. The applications of power Doppler guided FUS is not only limited for the use of brain applications. Using vascular imaging, FUS in conjunctions with PSNDs can be used to target specific vasculature in tumor using multiple foci with the goal of causing ablation and necrosis, thereby promoting tumor vasculature destruction by ablating the tumors.

BIBLIOGRAPHY

[1] S. Tsukamoto *et al.*, "Current Overview of Treatment for Metastatic Bone Disease," *Curr. Oncol.*, vol. 28, no. 5, pp. 3347–3372, Aug. 2021, doi: 10.3390/curroncol28050290.

[2] C. Iorio-Morin *et al.*, "Bilateral Focused Ultrasound Thalamotomy for Essential Tremor (BEST-FUS Phase 2 Trial)," *Mov. Disord.*, vol. 36, no. 11, pp. 2653–2662, Nov. 2021, doi: https://doi.org/10.1002/mds.28716.

[3] P. S. Fishman and J. M. Fischell, "Focused Ultrasound Mediated Opening of the Blood-Brain Barrier for Neurodegenerative Diseases.," *Front. Neurol.*, vol. 12, p. 749047, 2021, doi: 10.3389/fneur.2021.749047.

[4] L. R. Abrams, M. O. Koch, and C. D. Bahler, "Focal High-Intensity Focused Ultrasound Ablation of the Prostate.," *J. Endourol.*, vol. 35, no. S2, pp. S24–S32, Sep. 2021, doi: 10.1089/end.2020.1161.

[5] A. Abrahao *et al.*, "First-in-human trial of blood–brain barrier opening in amyotrophic lateral sclerosis using MR-guided focused ultrasound," *Nat. Commun.*, vol. 10, no. 1, p. 4373, 2019, doi: 10.1038/s41467-019-12426-9.

[6] T. Mainprize *et al.*, "Blood-Brain Barrier Opening in Primary Brain Tumors with Non-invasive MR-Guided Focused Ultrasound: A Clinical Safety and Feasibility Study," *Sci. Rep.*, vol. 9, no. 1, pp. 1–7, 2019, doi: 10.1038/s41598-018-36340-0.

[7] L. H. Treat, N. McDannold, N. Vykhodtseva, Y. Zhang, K. Tam, and K. Hynynen, "Targeted delivery of doxorubicin to the rat brain at therapeutic levels using MRI-guided focused ultrasound.," *Int. J. cancer*, vol. 121, no. 4, pp. 901–907, Aug. 2007, doi: 10.1002/ijc.22732.

[8] F. Wu *et al.*, "Extracorporeal high intensity focused ultrasound ablation in the treatment of 1038 patients with solid carcinomas in China: An overview," *Ultrason. Sonochem.*, vol. 11, no. 3–4, pp. 149–154, 2004, doi: 10.1016/j.ultsonch.2004.01.011.

[9] F. Wu *et al.*, "A randomised clinical trial of high-intensity focused ultrasound ablation for the treatment of patients with localised breast cancer," *Br. J. Cancer*, vol. 89, no. 12, pp. 2227–2233, 2003, doi: 10.1038/sj.bjc.6601411.

[10] D. Gianfelice, A. Khiat, M. Amara, A. Belblidia, and Y. Boulanger, "MR imaging-guided focused ultrasound surgery of breast cancer: correlation of dynamic contrast-enhanced MRI with histopathologic findings.," *Breast Cancer Res. Treat.*, vol. 82, no. 2, pp. 93–101, Nov. 2003, doi:

10.1023/B:BREA.0000003956.11376.5b.

[11] D. Gianfelice, A. Khiat, M. Amara, A. Belblidia, and Y. Boulanger, “MR Imaging–guided Focused US Ablation of Breast Cancer: Histopathologic Assessment of Effectiveness—Initial Experience,” *Radiology*, vol. 227, no. 3, pp. 849–855, 2003, doi: 10.1148/radiol.2281012163.

[12] L. G. Merckel *et al.*, “First clinical experience with a dedicated MRI-guided high-intensity focused ultrasound system for breast cancer ablation,” *Eur. Radiol.*, vol. 26, no. 11, pp. 4037–4046, 2016, doi: 10.1007/s00330-016-4222-9.

[13] M. L. Schwartz *et al.*, “Skull bone marrow injury caused by MR-guided focused ultrasound for cerebral functional procedures.,” *J. Neurosurg.*, vol. 130, no. 3, pp. 758–762, May 2018, doi: 10.3171/2017.11.JNS17968.

[14] L. C. Phillips, C. Puett, P. S. Sheeran, P. A. Dayton, G. Wilson Miller, and T. O. Matsunaga, “Erratum: Phase-shift perfluorocarbon agents enhance high intensity focused ultrasound thermal delivery with reduced near-field heating [J. Acoust. Soc. Am. 134, 1473–1482 (2013)],” *J. Acoust. Soc. Am.*, vol. 134, no. 6, pp. 4575–4575, 2013, doi: 10.1121/1.4828830.

[15] G. Wilson Miller, P. A. Dayton, P. S. Sheeran, T. O. Matsunaga, L. C. Phillips, and C. Puett, “Phase-shift perfluorocarbon agents enhance high intensity focused ultrasound thermal delivery with reduced near-field heating,” *J. Acoust. Soc. Am.*, vol. 134, no. 2, pp. 1473–1482, 2013, doi: 10.1121/1.4812866.

[16] H. Furusawa *et al.*, “The evolving non-surgical ablation of breast cancer: Mr Guided focused ultrasound (MRgFUS),” *Breast Cancer*, vol. 14, no. 1, pp. 55–58, 2007, doi: 10.2325/jbcs.14.55.

[17] R. Magnin *et al.*, “Magnetic resonance-guided motorized transcranial ultrasound system for blood-brain barrier permeabilization along arbitrary trajectories in rodents,” *J. Ther. ultrasound*, vol. 3, p. 22, Dec. 2015, doi: 10.1186/s40349-015-0044-5.

[18] R. Í. O’Connor, P. A. Kiely, and C. P. Dunne, “The relationship between post-surgery infection and breast cancer recurrence,” *J. Hosp. Infect.*, vol. 106, no. 3, pp. 522–535, 2020, doi: https://doi.org/10.1016/j.jhin.2020.08.004.

[19] Z. Brownlee, R. Garg, M. Listo, P. Zavitsanos, D. E. Wazer, and K. E. Huber, “Late complications of radiation therapy for breast cancer: evolution in techniques and risk over time,” *Gland Surg.*, vol. 7, no. 4, pp. 371–378, Aug. 2018, doi: 10.21037/gs.2018.01.05.

[20] J. Blackmore, S. Shrivastava, J. Sallet, C. R. Butler, and R. O. Cleveland, “Ultrasound Neuromodulation:

A Review of Results, Mechanisms and Safety.," *Ultrasound Med. Biol.*, vol. 45, no. 7, pp. 1509–1536, Jul. 2019, doi: 10.1016/j.ultrasmedbio.2018.12.015.

[21] F. Wu *et al.*, "Heat fixation of cancer cells ablated with high-intensity-focused ultrasound in patients with breast cancer," *Am. J. Surg.*, vol. 192, no. 2, pp. 179–184, 2006, doi: 10.1016/j.amjsurg.2006.03.014.

[22] R. D. Airan *et al.*, "Noninvasive Targeted Transcranial Neuromodulation via Focused Ultrasound Gated Drug Release from Nanoemulsions.," *Nano Lett.*, vol. 17, no. 2, pp. 652–659, Feb. 2017, doi: 10.1021/acs.nanolett.6b03517.

[23] N. Todd *et al.*, "Modulation of brain function by targeted delivery of GABA through the disrupted blood-brain barrier," *Neuroimage*, vol. 189, pp. 267–275, Apr. 2019, doi: 10.1016/j.neuroimage.2019.01.037.

[24] Y. S. Kim *et al.*, "Volumetric MR-HIFU ablation of uterine fibroids: Role of treatment cell size in the improvement of energy efficiency," *Eur. J. Radiol.*, vol. 81, no. 11, pp. 3652–3659, 2012, doi: 10.1016/j.ejrad.2011.09.005.

[25] A.-S. Bertrand *et al.*, "Focused ultrasound for the treatment of bone metastases: effectiveness and feasibility," *J. Ther. ultrasound*, vol. 6, p. 8, Nov. 2018, doi: 10.1186/s40349-018-0117-3.

[26] J. J. Li, M. F. Gu, G. Y. Luo, L. Z. Liu, R. Zhang, and G. L. Xu, "Complications of high intensity focused ultrasound for patients with hepatocellular carcinoma," *Technol. Cancer Res. Treat.*, vol. 8, no. 3, pp. 217–224, 2009, doi: 10.1177/153303460900800306.

[27] H. Fukuda *et al.*, "Treatment of Small Hepatocellular Carcinomas with US-Guided High-Intensity Focused Ultrasound," *Ultrasound Med. Biol.*, vol. 37, no. 8, pp. 1222–1229, 2011, doi: 10.1016/j.ultrasmedbio.2011.04.020.

[28] C. H. Halpern *et al.*, "Three-year follow-up of prospective trial of focused ultrasound thalamotomy for essential tremor.," *Neurology*, vol. 93, no. 24, pp. e2284–e2293, Dec. 2019, doi: 10.1212/WNL.0000000000008561.

[29] M. Rohani and A. Fasano, "Focused ultrasound for essential tremor: Review of the evidence and discussion of current hurdles," *Tremor and Other Hyperkinetic Movements*, vol. 7, pp. 1–12, 2017, doi: 10.7916/D8Z89JN1.

[30] G. T. Clement and K. Hynynen, "A non-invasive method for focusing ultrasound through the human skull," *Phys. Med. Biol.*, vol. 47, no. 8, pp. 1219–1236, 2002, doi: 10.1088/0031-9155/47/8/301.

[31] G. T. Clement, J. Sun, T. Giesecke, and K. Hynynen, "A hemisphere array for non-invasive ultrasound

brain therapy and surgery," *Phys. Med. Biol.*, vol. 45, no. 12, pp. 3707–3719, 2000, doi: 10.1088/0031-9155/45/12/314.

[32] C. M. C. Tempany, E. A. Stewart, N. McDannold, B. J. Quade, F. A. Jolesz, and K. Hynynen, "MR imaging-guided focused ultrasound surgery of uterine leiomyomas: a feasibility study.," *Radiology*, vol. 226, no. 3, pp. 897–905, Mar. 2003, doi: 10.1148/radiol.2271020395.

[33] E. A. Stewart *et al.*, "Focused ultrasound treatment of uterine fibroid tumors: safety and feasibility of a noninvasive thermoablative technique.," *Am. J. Obstet. Gynecol.*, vol. 189, no. 1, pp. 48–54, Jul. 2003, doi: 10.1067/mob.2003.345.

[34] Y. Wang, X. Liu, W. Wang, J. Tang, and L. Song, "Long-term Clinical Outcomes of US-Guided High-Intensity Focused Ultrasound Ablation for Symptomatic Submucosal Fibroids: A Retrospective Comparison with Uterus–Sparing Surgery," *Acad. Radiol.*, vol. 28, no. 8, pp. 1102–1107, 2021, doi: https://doi.org/10.1016/j.acra.2020.05.010.

[35] M. Zappia *et al.*, "Treatment of essential tremor: a systematic review of evidence and recommendations from the Italian Movement Disorders Association.," *J. Neurol.*, vol. 260, no. 3, pp. 714–740, Mar. 2013, doi: 10.1007/s00415-012-6628-x.

[36] E. Della Flora, C. L. Perera, A. L. Cameron, and G. J. Maddern, "Deep brain stimulation for essential tremor: a systematic review.," *Mov. Disord.*, vol. 25, no. 11, pp. 1550–1559, Aug. 2010, doi: 10.1002/mds.23195.

[37] Y. Higuchi, S. Matsuda, and T. Serizawa, "Gamma knife radiosurgery in movement disorders: Indications and limitations.," *Mov. Disord.*, vol. 32, no. 1, pp. 28–35, Jan. 2017, doi: 10.1002/mds.26625.

[38] O. Sydow, S. Thobois, F. Alesch, and J. D. Speelman, "Multicentre European study of thalamic stimulation in essential tremor: a six year follow up," *J. Neurol. Neurosurg. \& Psychiatry*, vol. 74, no. 10, pp. 1387–1391, 2003, doi: 10.1136/jnnp.74.10.1387.

[39] J. W. Chang *et al.*, "A prospective trial of magnetic resonance-guided focused ultrasound thalamotomy for essential tremor: Results at the 2-year follow-up.," *Ann. Neurol.*, vol. 83, no. 1, pp. 107–114, Jan. 2018, doi: 10.1002/ana.25126.

[40] W. J. Elias *et al.*, "A Randomized Trial of Focused Ultrasound Thalamotomy for Essential Tremor," *N. Engl. J. Med.*, vol. 375, no. 8, pp. 730–739, Aug. 2016, doi: 10.1056/NEJMoa1600159.

[41] M. J. Kim *et al.*, "Technical and operative factors affecting magnetic resonance imaging–guided focused

ultrasound thalamotomy for essential tremor: experience from 250 treatments," *J. Neurosurg.*, pp. 1–9, 2021, doi: 10.3171/2020.11.jns202580.

[42] Y. Ji, Z. Han, L. Shao, and Y. Zhao, "Evaluation of in vivo antitumor effects of low-frequency ultrasound-mediated miRNA-133a microbubble delivery in breast cancer," *Cancer Med.*, vol. 5, no. 9, pp. 2534–2543, Sep. 2016, doi: 10.1002/cam4.840.

[43] J. Kang *et al.*, "Antitumor effect of docetaxel-loaded lipid microbubbles combined with ultrasound-targeted microbubble activation on VX2 rabbit liver tumors.," *J. ultrasound Med. Off. J. Am. Inst. Ultrasound Med.*, vol. 29, no. 1, pp. 61–70, Jan. 2010, doi: 10.7863/jum.2010.29.1.61.

[44] M. C. Cochran *et al.*, "Disposition of ultrasound sensitive polymeric drug carrier in a rat hepatocellular carcinoma model," *Acad. Radiol.*, vol. 18, no. 11, pp. 1341–1348, Nov. 2011, doi: 10.1016/j.acra.2011.06.013.

[45] I. Lentacker, B. Geers, J. Demeester, S. C. De Smedt, and N. N. Sanders, "Design and evaluation of doxorubicin-containing microbubbles for ultrasound-triggered doxorubicin delivery: cytotoxicity and mechanisms involved," *Mol. Ther.*, vol. 18, no. 1, pp. 101–108, Jan. 2010, doi: 10.1038/mt.2009.160.

[46] L. Zhu, A. Nazeri, M. Altman, D. Thotala, N. Sharifai, and H. Chen, "Focused ultrasound-mediated microbubble destruction for glioblastoma treatment," *J. Acoust. Soc. Am.*, vol. 145, no. 3, p. 1862, Mar. 2019, doi: 10.1121/1.5101727.

[47] D. Kim, J. Han, S. Y. Park, H. Kim, J.-H. Park, and H. J. Lee, "Antitumor Efficacy of Focused Ultrasound-MFL Nanoparticles Combination Therapy in Mouse Breast Cancer Xenografts," *Mater. (Basel, Switzerland)*, vol. 13, no. 5, p. 1099, Mar. 2020, doi: 10.3390/ma13051099.

[48] Q. Gong, X. Gao, W. Liu, T. Hong, and C. Chen, "Drug-Loaded Microbubbles Combined with Ultrasound for Thrombolysis and Malignant Tumor Therapy," *Biomed Res. Int.*, vol. 2019, p. 6792465, 2019, doi: 10.1155/2019/6792465.

[49] N. Y. Rapoport, A. M. Kennedy, J. E. Shea, C. L. Scaife, and K. H. Nam, "Controlled and targeted tumor chemotherapy by ultrasound-activated nanoemulsions/microbubbles," *J. Control. Release*, vol. 138, no. 3, pp. 268–276, 2009, doi: 10.1016/j.jconrel.2009.05.026.

[50] A. Kheirolomoom *et al.*, "Complete regression of local cancer using temperature-sensitive liposomes combined with ultrasound-mediated hyperthermia," *J. Control. Release*, vol. 172, no. 1, pp. 266–273, Nov. 2013, doi: 10.1016/j.jconrel.2013.08.019.

[51] M. A. Santos, D. E. Goertz, and K. Hynynen, “Focused Ultrasound Hyperthermia Mediated Drug Delivery Using Thermosensitive Liposomes and Visualized With in vivo Two-Photon Microscopy,” *Theranostics*, vol. 7, no. 10, pp. 2718–2731, Jul. 2017, doi: 10.7150/thno.19662.

[52] C. Gasca-Salas *et al.*, “Blood-brain barrier opening with focused ultrasound in Parkinson’s disease dementia,” *Nat. Commun.*, vol. 12, no. 1, p. 779, 2021, doi: 10.1038/s41467-021-21022-9.

[53] A. R. Rezai *et al.*, “Noninvasive hippocampal blood−brain barrier opening in Alzheimer’s disease with focused ultrasound,” *Proc. Natl. Acad. Sci. U. S. A.*, vol. 117, no. 17, pp. 9180–9182, 2020, doi: 10.1073/pnas.2002571117.

[54] K. Yamamoto *et al.*, “Focused Ultrasound Thalamotomy for Tremor-dominant Parkinson’s Disease: A Prospective 1-year Follow-up Study,” *Neurol. Med. Chir. (Tokyo).*, vol. 61, no. 7, pp. 414–421, Jul. 2021, doi: 10.2176/nmc.oa.2020-0370.

[55] K. Hynynen, N. McDannold, N. Vykhodtseva, and F. A. Jolesz, “Noninvasive MR Imaging–guided Focal Opening of the Blood-Brain Barrier in Rabbits,” *Radiology*, vol. 220, no. 3, pp. 640–646, Sep. 2001, doi: 10.1148/radiol.2202001804.

[56] G. Samiotaki, C. Acosta, S. Wang, and E. E. Konofagou, “Enhanced delivery and bioactivity of the neurturin neurotrophic factor through focused ultrasound-mediated blood--brain barrier opening in vivo.,” *J. Cereb. blood flow Metab. Off. J. Int. Soc. Cereb. Blood Flow Metab.*, vol. 35, no. 4, pp. 611–622, Mar. 2015, doi: 10.1038/jcbfm.2014.236.

[57] N. Todd, Y. Zhang, M. Livingstone, D. Borsook, and N. McDannold, “The neurovascular response is attenuated by focused ultrasound-mediated disruption of the blood-brain barrier.,” *Neuroimage*, vol. 201, p. 116010, Nov. 2019, doi: 10.1016/j.neuroimage.2019.116010.

[58] H.-L. Liu *et al.*, “Blood-Brain Barrier Disruption with Focused Ultrasound Enhances Delivery of Chemotherapeutic Drugs for Glioblastoma Treatment,” *Radiology*, vol. 255, no. 2, pp. 415–425, Apr. 2010, doi: 10.1148/radiol.10090699.

[59] H.-J. Wei *et al.*, “Focused Ultrasound-Mediated Blood-Brain Barrier Opening Increases Delivery and Efficacy of Etoposide for Glioblastoma Treatment,” *Int. J. Radiat. Oncol.*, vol. 110, no. 2, pp. 539–550, 2021, doi: https://doi.org/10.1016/j.ijrobp.2020.12.019.

[60] H. Lea-Banks, M. A. O’Reilly, C. Hamani, and K. Hynynen, “Localized anesthesia of a specific brain region using ultrasound-responsive barbiturate nanodroplets.,” *Theranostics*, vol. 10, no. 6, pp. 2849–

2858, 2020, doi: 10.7150/thno.41566.

[61] J. Y. Chapelon *et al.*, “Effects of High-Energy Focused Ultrasound on Kidney Tissue in the Rat and the Dog,” *Eur. Urol.*, vol. 22, pp. 147–152, 1992, doi: 10.1159/000474743.

[62] G. ter Haar, I. Rivens, L. Chen, and S. Riddler, “High intensity focused ultrasound for the treatment of rat tumours.,” *Phys. Med. Biol.*, vol. 36, no. 11, pp. 1495–1501, Nov. 1991, doi: 10.1088/0031-9155/36/11/009.

[63] D. Gianfelice, A. Khiat, Y. Boulanger, M. Amara, and A. Belblidia, “Feasibility of magnetic resonance imaging-guided focused ultrasound surgery as an adjunct to tamoxifen therapy in high-risk surgical patients with breast carcinoma.,” *J. Vasc. Interv. Radiol.*, vol. 14, no. 10, pp. 1275–1282, Oct. 2003, doi: 10.1097/01.rvi.0000092900.73329.a2.

[64] M. A. Hall-Craggs, “Interventional MRI of the breast: minimally invasive therapy.,” *Eur. Radiol.*, vol. 10, no. 1, pp. 59–62, 2000, doi: 10.1007/s003300050007.

[65] P. E. Huber *et al.*, “A new noninvasive approach in breast cancer therapy using magnetic resonance imaging-guided focused ultrasound surgery.,” *Cancer Res.*, vol. 61, no. 23, pp. 8441–8447, Dec. 2001.

[66] H. Furusawa *et al.*, “Magnetic Resonance-Guided Focused Ultrasound Surgery of Breast Cancer: Reliability and Effectiveness,” *J. Am. Coll. Surg.*, vol. 203, no. 1, pp. 54–63, 2006, doi: 10.1016/j.jamcollsurg.2006.04.002.

[67] S. Bhadane, R. Karshafian, and J. Tavakkoli, “Microbubble-enhanced HIFU therapy: Effect of exposure parameters on thermal lesion volume and temperature,” *AIP Conf. Proc.*, vol. 1503, no. November 2012, pp. 65–70, 2012, doi: 10.1063/1.4769919.

[68] D. Cosgrove, “Ultrasound contrast agents: an overview.,” *Eur. J. Radiol.*, vol. 60, no. 3, pp. 324–330, Dec. 2006, doi: 10.1016/j.ejrad.2006.06.022.

[69] T. Yu, X. Fan, S. Xiong, K. Hu, and Z. Wang, “Microbubbles assist goat liver ablation by high intensity focused ultrasound,” *Eur. Radiol.*, vol. 16, no. 7, pp. 1557–1563, 2006, doi: 10.1007/s00330-006-0176-7.

[70] F. S. Villanueva and W. R. Wagner, “Ultrasound molecular imaging of cardiovascular disease,” *Nat. Clin. Pract. Cardiovasc. Med.*, vol. 5 Suppl 2, no. 0 2, pp. S26–S32, Aug. 2008, doi: 10.1038/ncpcardio1246.

[71] K. Ferrara, R. Pollard, and M. Borden, “Ultrasound Microbubble Contrast Agents: Fundamentals and Application to Gene and Drug Delivery,” *Annu. Rev. Biomed. Eng.*, vol. 9, no. 1, pp. 415–447, Jul. 2007, doi: 10.1146/annurev.bioeng.8.061505.095852.

[72] L. Mullin, R. Gessner, J. Kwan, M. Kaya, M. A. Borden, and P. A. Dayton, “Effect of anesthesia carrier gas on in vivo circulation times of ultrasound microbubble contrast agents in rats,” *Contrast Media Mol. Imaging*, vol. 6, no. 3, pp. 126–131, 2011, doi: 10.1002/cmmi.414.

[73] M. W. Dewhirst, B. L. Viglianti, M. Lora-Michiels, P. J. Hoopes, and M. Hanson, “THERMAL DOSE REQUIREMENT FOR TISSUE EFFECT: EXPERIMENTAL AND CLINICAL FINDINGS,” *Proc. SPIE--the Int. Soc. Opt. Eng.*, vol. 4954, p. 37, Jun. 2003, doi: 10.1117/12.476637.

[74] N. McDannold, E.-J. Park, C.-S. Mei, E. Zadicario, and F. Jolesz, “Evaluation of three-dimensional temperature distributions produced by a low-frequency transcranial focused ultrasound system within ex vivo human skulls.,” *IEEE Trans. Ultrason. Ferroelectr. Freq. Control*, vol. 57, no. 9, pp. 1967–1976, Sep. 2010, doi: 10.1109/TUFFC.2010.1644.

[75] K. Hynynen *et al.*, “Pre-clinical testing of a phased array ultrasound system for MRI-guided noninvasive surgery of the brain--a primate study.,” *Eur. J. Radiol.*, vol. 59, no. 2, pp. 149–156, Aug. 2006, doi: 10.1016/j.ejrad.2006.04.007.

[76] InSightec, “A Clinical Study to Evaluate Safety of the ExAblate 2100 UF V2 System in the Treatment of Symptomatic Uterine Fibroids.” ClinicalTrials.gov Identifier: NCT01092988, 2010, [Online]. Available: https://clinicaltrials.gov/ct2/show/NCT01092988.

[77] E. S. Ebbini and G. Ter Haar, “Ultrasound-guided therapeutic focused ultrasound: Current status and future directions,” *Int. J. Hyperth.*, vol. 31, no. 2, pp. 77–89, 2015, doi: 10.3109/02656736.2014.995238.

[78] E. Hutchinson, M. Dahleh, and K. Hynynen, “The feasibility of MRI feedback control for intracavitary phased array hyperthermia treatments,” *Int. J. Hyperth.*, 1998, doi: 10.3109/02656739809018213.

[79] M. O. Leach, “Breast cancer screening in women at high risk using MRI.,” *NMR Biomed.*, vol. 22, no. 1, pp. 17–27, Jan. 2009, doi: 10.1002/nbm.1326.

[80] K. Hynynen, “MRI-guided focused ultrasound treatments,” *Ultrasonics*, vol. 50, no. 2, pp. 221–229, 2010, doi: 10.1016/j.ultras.2009.08.015.

[81] K. Hynynen, A. Darkazanli, E. Unger, and J. F. Schenck, “MRI-guided noninvasive ultrasound surgery.,” *Med. Phys.*, vol. 20, no. 1, pp. 107–115, 1993, doi: 10.1118/1.597093.

[82] K. Hynynen *et al.*, “MR imaging-guided focused ultrasound surgery of fibroadenomas in the breast: a feasibility study.,” *Radiology*, vol. 219, no. 1, pp. 176–185, Apr. 2001, doi: 10.1148/radiology.219.1.r01ap02176.

[83] K. Hynynen *et al.*, “500-element ultrasound phased array system for noninvasive focal surgery of the brain: a preliminary rabbit study with ex vivo human skulls.,” *Magn. Reson. Med.*, vol. 52, no. 1, pp. 100–107, Jul. 2004, doi: 10.1002/mrm.20118.

[84] N. McDannold, G. T. Clement, P. Black, F. Jolesz, and K. Hynynen, “Transcranial magnetic resonance imaging- guided focused ultrasound surgery of brain tumors: initial findings in 3 patients,” *Neurosurgery*, vol. 66, no. 2, pp. 323–332, Feb. 2010, doi: 10.1227/01.NEU.0000360379.95800.2F.

[85] D. E. Goertz, C. Wright, and K. Hynynen, “Contrast agent kinetics in the rabbit brain during exposure to therapeutic ultrasound,” *Ultrasound Med. Biol.*, vol. 36, no. 6, pp. 916–924, Jun. 2010, doi: 10.1016/j.ultrasmedbio.2010.03.005.

[86] N. McDannold *et al.*, “Blood-brain barrier disruption and delivery of irinotecan in a rat model using a clinical transcranial MRI-guided focused ultrasound system,” *Sci. Rep.*, 2020, doi: 10.1038/s41598-020-65617-6.

[87] N. Todd *et al.*, “Focused ultrasound induced opening of the blood-brain barrier disrupts inter-hemispheric resting state functional connectivity in the rat brain,” *Neuroimage*, 2018, doi: 10.1016/j.neuroimage.2018.05.063.

[88] J. Hindman, “Proton resonance shift of water in gas and liquid states,” *J. Chem. Phys.*, vol. 44, pp. 4582–4592, 1966.

[89] Y. Ishihara *et al.*, “A precise and fast temperature mapping using water proton chemical shift,” *Magn. Reson. Med.*, vol. 34, no. 6, pp. 814–823, Dec. 1995, doi: 10.1002/mrm.1910340606.

[90] V. Rieke and K. Butts Pauly, “MR thermometry,” *J. Magn. Reson. Imaging*, vol. 27, no. 2, pp. 376–390, Feb. 2008, doi: 10.1002/jmri.21265.

[91] P. S. Fishman *et al.*, “Neurological adverse event profile of magnetic resonance imaging-guided focused ultrasound thalamotomy for essential tremor.,” *Mov. Disord.*, vol. 33, no. 5, pp. 843–847, May 2018, doi: 10.1002/mds.27401.

[92] N. McDannold and S. E. Maier, “Magnetic resonance acoustic radiation force imaging,” *Med. Phys.*, vol. 35, no. 8, pp. 3748–3758, 2008, doi: 10.1118/1.2956712.

[93] M. A. Phipps *et al.*, “Considerations for ultrasound exposure during transcranial MR acoustic radiation force imaging,” *Sci. Rep.*, vol. 9, no. 1, p. 16235, 2019, doi: 10.1038/s41598-019-52443-8.

[94] Y. Huang, L. Curiel, A. Kukic, D. B. Plewes, R. Chopra, and K. Hynynen, “MR acoustic radiation force

imaging: in vivo comparison to ultrasound motion tracking.," *Med. Phys.*, vol. 36, no. 6, pp. 2016–2020, Jun. 2009, doi: 10.1118/1.3120289.

[95] C. Y. Kong *et al.*, "MRI-Guided Focused Ultrasound Surgery for Uterine Fibroid Treatment: A Cost-Effectiveness Analysis," *Am. J. Roentgenol.*, vol. 203, no. 2, pp. 361–371, Jul. 2014, doi: 10.2214/AJR.13.11446.

[96] Y. Meng *et al.*, "Cost-effectiveness analysis of MR-guided focused ultrasound thalamotomy for tremor-dominant Parkinson's disease," *J. Neurosurg.*, vol. 135, no. 1, pp. 273–278, 2020, doi: 10.3171/2020.5.JNS20692.

[97] M. Inoue, S. Nakatsuka, and M. Jinzaki, "Cryoablation of early-stage primary lung cancer," *Biomed Res. Int.*, vol. 2014, 2014, doi: 10.1155/2014/521691.

[98] C. R. De Lope, S. Tremosini, A. Forner, M. Reig, and J. Bruix, "Management of HCC," *J. Hepatol.*, vol. 56, no. SUPPL. 1, pp. 75–87, 2012, doi: 10.1016/S0168-8278(12)60009-9.

[99] H. B. El-Serag, "Epidemiology of viral hepatitis and hepatocellular carcinoma," *Gastroenterology*, vol. 142, no. 6, pp. 1264–1273, 2012, doi: 10.1053/j.gastro.2011.12.061.

[100] T. Livraghi, H. Mäkisalo, and P. D. Line, "Treatment options in hepatocellular carcinoma today," *Scand. J. Surg.*, vol. 100, no. 1, pp. 22–29, 2011, doi: 10.1177/145749691110000105.

[101] H. Nishikawa and Y. Osaki, "Comparison of high-intensity focused ultrasound therapy and radiofrequency ablation for recurrent hepatocellular carcinoma.," *Hepatobiliary Surg. Nutr.*, vol. 2, no. 3, pp. 168–70, 2013, doi: 10.3978/j.issn.2304-3881.2013.03.01.

[102] M. S. Sabel *et al.*, "Cryoablation of early-stage breast cancer: Work-in-progress report of a multi-institutional trial," *Ann. Surg. Oncol.*, vol. 11, no. 5, pp. 542–549, 2004, doi: 10.1245/ASO.2004.08.003.

[103] B. D. Fornage *et al.*, "Small breast cancer treated with US-guided RFA- Feasibility Study," no. 11, pp. 215–224, 2004.

[104] B. D. Fornage *et al.*, "Small (≤2-cm) Breast Cancer Treated with US-guided Radiofrequency Ablation: Feasibility Study," *Radiology*, vol. 231, no. 1, pp. 215–224, 2007, doi: 10.1148/radiol.2311030651.

[105] W. Zhou *et al.*, "Microwave Coagulation of Small Breast Cancers: A Clinical Study," *Radiology*, vol. 263, no. 2, 2012, doi: 10.1148/radiol.12111901/-/DC1.

[106] P. S. Sheeran, J. D. Rojas, C. Puett, J. Hjelmquist, C. B. Arena, and P. A. Dayton, "Contrast-enhanced ultrasound imaging and in vivo circulatory kinetics with low-boiling-point nanoscale phase-change

perfluorocarbon agents," *Ultrasound Med. Biol.*, vol. 41, no. 3, pp. 814–831, Mar. 2015, doi: 10.1016/j.ultrasmedbio.2014.10.020.

[107] L. C. Phillips, C. Puett, P. S. Sheeran, P. A. Dayton, G. Wilson Miller, and T. O. Matsunaga, "Erratum: Phase-shift perfluorocarbon agents enhance high intensity focused ultrasound thermal delivery with reduced near-field heating [J. Acoust. Soc. Am. 134, 1473–1482 (2013)]," *J. Acoust. Soc. Am.*, vol. 134, no. 6, pp. 4575–4575, 2013, doi: 10.1121/1.4828830.

[108] P. S. Sheeran and P. A. Dayton, "Improving the performance of phase-change perfluorocarbon droplets for medical ultrasonography: current progress, challenges, and prospects," *Scientifica (Cairo).*, vol. 2014, p. 579684, 2014, doi: 10.1155/2014/579684.

[109] L. C. Phillips, C. Puett, P. S. Sheeran, P. A. Dayton, G. Wilson Miller, and T. O. Matsunaga, "Erratum: Phase-shift perfluorocarbon agents enhance high intensity focused ultrasound thermal delivery with reduced near-field heating [J. Acoust. Soc. Am. 134, 1473–1482 (2013)]," *J. Acoust. Soc. Am.*, vol. 134, no. 6, pp. 4575–4575, 2013, doi: 10.1121/1.4828830.

[110] L. C. Moyer, K. F. Timbie, P. S. Sheeran, R. J. Price, G. W. Miller, and P. A. Dayton, "High-intensity focused ultrasound ablation enhancement in vivo via phase-shift nanodroplets compared to microbubbles," *J. Ther. Ultrasound*, vol. 3, no. 1, pp. 1–9, 2015, doi: 10.1186/s40349-015-0029-4.

[111] L. C. Moyer, K. F. Timbie, P. S. Sheeran, R. J. Price, G. W. Miller, and P. A. Dayton, "High-intensity focused ultrasound ablation enhancement in vivo via phase-shift nanodroplets compared to microbubbles," *J. Ther. Ultrasound*, vol. 3, no. 1, pp. 1–9, 2015, doi: 10.1186/s40349-015-0029-4.

[112] N. Shi and W. M. Pardridge, "Noninvasive gene targeting to the brain.," *Proc. Natl. Acad. Sci. U. S. A.*, vol. 97, no. 13, pp. 7567–7572, Jun. 2000, doi: 10.1073/pnas.130187497.

[113] D. Wu and W. M. Pardridge, "Neuroprotection with noninvasive neurotrophin delivery to the brain.," *Proc. Natl. Acad. Sci. U. S. A.*, vol. 96, no. 1, pp. 254–259, Jan. 1999, doi: 10.1073/pnas.96.1.254.

[114] A. Burgess, K. Shah, O. Hough, and K. Hynynen, "Focused ultrasound-mediated drug delivery through the blood-brain barrier.," *Expert Rev. Neurother.*, vol. 15, no. 5, pp. 477–491, May 2015, doi: 10.1586/14737175.2015.1028369.

[115] Z. K. Englander *et al.*, "Focused ultrasound mediated blood–brain barrier opening is safe and feasible in a murine pontine glioma model," *Sci. Rep.*, vol. 11, no. 1, pp. 1–10, 2021, doi: 10.1038/s41598-021-85180-y.

[116] Y. Yang *et al.*, “Cavitation dose painting for focused ultrasound-induced blood-brain barrier disruption,” *Sci. Rep.*, 2019, doi: 10.1038/s41598-019-39090-9.

[117] F. Xie, M. D. Boska, J. Lof, M. G. Uberti, J. M. Tsutsui, and T. R. Porter, “Effects of Transcranial Ultrasound and Intravenous Microbubbles on Blood Brain Barrier Permeability in a Large Animal Model,” *Ultrasound Med. Biol.*, vol. 34, no. 12, pp. 2028–2034, 2008, doi: 10.1016/j.ultrasmedbio.2008.05.004.

[118] N. D. Sheybani, A. R. Witter, W. J. Garrison, G. W. Miller, R. J. Price, and T. N. J. Bullock, “Profiling of the immune landscape in murine glioblastoma following blood brain/tumor barrier disruption with MR image-guided focused ultrasound,” *J. Neurooncol.*, 2021, doi: 10.1007/s11060-021-03887-4.

[119] J. B. Wang, M. Aryal, Q. Zhong, D. B. Vyas, and R. D. Airan, “Noninvasive Ultrasonic Drug Uncaging Maps Whole-Brain Functional Networks.,” *Neuron*, vol. 100, no. 3, pp. 728-738.e7, Nov. 2018, doi: 10.1016/j.neuron.2018.10.042.

[120] R. Seip and E. S. Ebbini, “Noninvasive estimation of tissue temperature response to heating fields using diagnostic ultrasound.,” *IEEE Trans. Biomed. Eng.*, vol. 42, no. 8, pp. 828–839, Aug. 1995, doi: 10.1109/10.398644.

[121] C. Simon, P. VanBaren, and E. S. Ebbini, “Two-dimensional temperature estimation using diagnostic ultrasound,” *IEEE Trans. Ultrason. Ferroelectr. Freq. Control*, vol. 45, no. 4, pp. 1088–1099, 1998, doi: 10.1109/58.710592.

[122] J. Civale *et al.*, “Calibration of ultrasound backscatter temperature imaging for high-intensity focused ultrasound treatment planning.,” *Ultrasound Med. Biol.*, vol. 39, no. 9, pp. 1596–1612, Sep. 2013, doi: 10.1016/j.ultrasmedbio.2013.04.001.

[123] R. M. Arthur, W. L. Straube, J. D. Starman, and E. G. Moros, “Noninvasive temperature estimation based on the energy of backscattered ultrasound.,” *Med. Phys.*, vol. 30, no. 6, pp. 1021–1029, Jun. 2003, doi: 10.1118/1.1570373.

[124] W. L. Straube and R. M. Arthur, “Theoretical estimation of the temperature dependence of backscattered ultrasonic power for noninvasive thermometry.,” *Ultrasound Med. Biol.*, vol. 20, no. 9, pp. 915–922, 1994, doi: 10.1016/0301-5629(94)90051-5.

[125] J. McLaughlan, I. Rivens, T. Leighton, and G. ter Haar, “A Study of Bubble Activity Generated in Ex Vivo Tissue by High Intensity Focused Ultrasound,” *Ultrasound Med. Biol.*, vol. 36, no. 8,

pp. 1327–1344, Aug. 2010, doi: 10.1016/j.ultrasmedbio.2010.05.011.

[126] A. Casper, A. Haritonova, D. Liu, J. Ballard, and E. Ebbini, “Real-time implementation of a dual-mode ultrasound array system: In vivo results,” in *2012 IEEE International Ultrasonics Symposium*, 2012, pp. 2164–2167, doi: 10.1109/ULTSYM.2012.0540.

[127] Y. Y. Botros, J. L. Volakis, P. VanBaren, and E. S. Ebbini, “A hybrid computational model for ultrasound phased-array heating in presence of strongly scattering obstacles.,” *IEEE Trans. Biomed. Eng.*, vol. 44, no. 11, pp. 1039–1050, Nov. 1997, doi: 10.1109/10.641331.

[128] P. Gélat, G. Ter Haar, and N. Saffari, “A comparison of methods for focusing the field of a HIFU array transducer through human ribs.,” *Phys. Med. Biol.*, vol. 59, no. 12, pp. 3139–3171, Jun. 2014, doi: 10.1088/0031-9155/59/12/3139.

[129] S. Bobkova, L. Gavrilov, V. Khokhlova, A. Shaw, and J. Hand, “Focusing of high-intensity ultrasound through the rib cage using a therapeutic random phased array.,” *Ultrasound Med. Biol.*, vol. 36, no. 6, pp. 888–906, Jun. 2010, doi: 10.1016/j.ultrasmedbio.2010.03.007.

[130] I. A. Shehata, J. R. Ballard, A. J. Casper, D. Liu, T. Mitchell, and E. S. Ebbini, “Feasibility of targeting atherosclerotic plaques by high-intensity-focused ultrasound: an in vivo study.,” *J. Vasc. Interv. Radiol.*, vol. 24, no. 12, pp. 1880-1887.e2, Dec. 2013, doi: 10.1016/j.jvir.2013.08.013.

[131] C. C. Coussios and M. Gyöngy, “Passive Spatial Mapping of Inertial Cavitation During HIFU Exposure,” *IEEE Trans. Biomed. Eng.*, vol. 57, no. 1, pp. 48–56, 2010.

[132] A. Novell *et al.*, “A new safety index based on intrapulse monitoring of ultra-harmonic cavitation during ultrasound-induced blood-brain barrier opening procedures,” *Sci. Rep.*, vol. 10, no. 1, p. 10088, 2020, doi: 10.1038/s41598-020-66994-8.

[133] S. V Morse *et al.*, “Rapid Short-pulse Ultrasound Delivers Drugs Uniformly across the Murine Blood-Brain Barrier with Negligible Disruption,” *Radiology*, vol. 291, no. 2, pp. 459–466, Mar. 2019, doi: 10.1148/radiol.2019181625.

[134] C. Errico, B. F. Osmanski, S. Pezet, O. Couture, Z. Lenkei, and M. Tanter, “Transcranial functional ultrasound imaging of the brain using microbubble-enhanced ultrasensitive Doppler,” *Neuroimage*, vol. 124, pp. 752–761, 2016, doi: 10.1016/j.neuroimage.2015.09.037.

[135] J. J. Choi, M. Pernot, S. A. Small, and E. E. Konofagou, “Noninvasive, transcranial and localized opening of the blood-brain barrier using focused ultrasound in mice,” *Ultrasound Med. Biol.*, 2007, doi:

10.1016/j.ultrasmedbio.2006.07.018.

[136] A. D'Andrea *et al.*, "Transcranial Doppler Ultrasound: Physical Principles and Principal Applications in Neurocritical Care Unit," *J. Cardiovasc. Echogr.*, vol. 26, no. 2, pp. 28–41, 2016, doi: 10.4103/2211-4122.183746.

[137] E. Macé, G. Montaldo, M. Fink, M. Tanter, I. Cohen, and R. Miles, "High sensitivity brain angiography using Ultrafast Doppler," *Proc. - IEEE Ultrason. Symp.*, pp. 1194–1197, 2010, doi: 10.1109/ULTSYM.2010.5935810.

[138] E. MacÉ, G. Montaldo, I. Cohen, M. Baulac, M. Fink, and M. Tanter, "Functional ultrasound imaging of the brain," *Nat. Methods*, vol. 8, no. 8, pp. 662–664, 2011, doi: 10.1038/nmeth.1641.

[139] C. Errico, B. F. Osmanski, S. Pezet, O. Couture, Z. Lenkei, and M. Tanter, "Transcranial functional ultrasound imaging of the brain using microbubble-enhanced ultrasensitive Doppler," *Neuroimage*, vol. 124, pp. 752–761, 2016, doi: 10.1016/j.neuroimage.2015.09.037.

[140] M. Gesnik *et al.*, "3D functional ultrasound imaging of the cerebral visual system in rodents," *Neuroimage*, vol. 149, pp. 267–274, 2017, doi: https://doi.org/10.1016/j.neuroimage.2017.01.071.

[141] É. Macé *et al.*, "Whole-Brain Functional Ultrasound Imaging Reveals Brain Modules for Visuomotor Integration," *Neuron*, vol. 100, no. 5, pp. 1241-1251.e7, 2018, doi: https://doi.org/10.1016/j.neuron.2018.11.031.

[142] C. Brunner, M. Grillet, A. Urban, B. Roska, G. Montaldo, and E. Macé, "Whole-brain functional ultrasound imaging in awake head-fixed mice," *Nat. Protoc.*, vol. 16, no. 7, pp. 3547–3571, 2021, doi: 10.1038/s41596-021-00548-8.

[143] C. Demene *et al.*, "Functional ultrasound imaging of brain activity in human newborns.," *Sci. Transl. Med.*, vol. 9, no. 411, Oct. 2017, doi: 10.1126/scitranslmed.aah6756.

[144] C. Demené, J. Mairesse, J. Baranger, M. Tanter, and O. Baud, "Ultrafast Doppler for neonatal brain imaging.," *Neuroimage*, vol. 185, pp. 851–856, Jan. 2019, doi: 10.1016/j.neuroimage.2018.04.016.

[145] C. Errico *et al.*, "Ultrafast ultrasound localization microscopy for deep super-resolution vascular imaging," *Nature*, vol. 527, no. 7579, pp. 499–502, 2015, doi: 10.1038/nature16066.

[146] B. Heiles, A. Chavignon, V. Hingot, P. Lopez, E. Teston, and O. Couture, "Performance benchmarking of microbubble-localization algorithms for ultrasound localization microscopy," *Nat. Biomed. Eng.*, 2022, doi: 10.1038/s41551-021-00824-8.

[147] E. S. Ebbini and C. A. Cain, “Multiple-Focus Ultrasound Phased-Array Pattern Synthesis: Optimal Driving-Signal Distributions for Hyperthermia,” *IEEE Trans. Ultrason. Ferroelectr. Freq. Control*, vol. 36, no. 5, pp. 540–548, 1989, doi: 10.1109/58.31798.

[148] A. N. Pouliopoulos, C. Li, M. Tinguely, V. Garbin, M.-X. Tang, and J. J. Choi, “Rapid short-pulse sequences enhance the spatiotemporal uniformity of acoustically driven microbubble activity during flow conditions,” *J. Acoust. Soc. Am.*, vol. 140, no. 4, pp. 2469–2480, 2016, doi: 10.1121/1.4964271.

[149] J. J. Choi *et al.*, “Microbubble-size dependence of focused ultrasound-induced bloodBrain barrier opening in mice in vivo,” *IEEE Trans. Biomed. Eng.*, 2010, doi: 10.1109/TBME.2009.2034533.

[150] Y.-S. Tung, F. Vlachos, J. J. Choi, T. Deffieux, K. Selert, and E. E. Konofagou, “In vivo transcranial cavitation threshold detection during ultrasound-induced blood-brain barrier opening in mice.,” *Phys. Med. Biol.*, vol. 55, no. 20, pp. 6141–6155, Oct. 2010, doi: 10.1088/0031-9155/55/20/007.

[151] M. A. O’Reilly, R. M. Jones, and K. Hynynen, “Transcranial bubble activity mapping for therapy and imaging,” *J. Acoust. Soc. Am.*, vol. 134, no. 5, pp. 3975–3975, Nov. 2013, doi: 10.1121/1.4830483.

[152] R. M. Jones, L. Deng, K. Leung, D. McMahon, M. A. O’Reilly, and K. Hynynen, “Three-dimensional transcranial microbubble imaging for guiding volumetric ultrasound-mediated blood-brain barrier opening,” *Theranostics*, vol. 8, no. 11, pp. 2909–2926, 2018, doi: 10.7150/thno.24911.

[153] R. M. Jones, D. McMahon, and K. Hynynen, “Ultrafast three-dimensional microbubble imaging *in vivo* predicts tissue damage volume distributions during nonthermal brain ablation,” *Theranostics*, vol. 10, no. 16, pp. 7211–7230, 2020, doi: 10.7150/thno.47281.

[154] E. E. Konofagou *et al.*, “Ultrasound-induced blood-brain barrier opening,” *Curr. Pharm. Biotechnol.*, vol. 13, no. 7, pp. 1332–1345, Jun. 2012, doi: 10.2174/138920112800624364.

[155] K. Hynynen *et al.*, “Focal disruption of the blood-brain barrier due to 260-kHz ultrasound bursts: a method for molecular imaging and targeted drug delivery.,” *J. Neurosurg.*, vol. 105, no. 3, pp. 445–454, Sep. 2006, doi: 10.3171/jns.2006.105.3.445.

[156] H. Chen and E. E. Konofagou, “The Size of Blood–Brain Barrier Opening Induced by Focused Ultrasound is Dictated by the Acoustic Pressure,” *J. Cereb. Blood Flow Metab.*, vol. 34, no. 7, pp. 1197–1204, Apr. 2014, doi: 10.1038/jcbfm.2014.71.

[157] S. Hu, X. Zhang, M. Unger, I. Patties, A. Melzer, and L. Landgraf, “Focused Ultrasound-Induced Cavitation Sensitizes Cancer Cells to Radiation Therapy and Hyperthermia,” *Cells*, vol. 9, no. 12, p. 2595,

Dec. 2020, doi: 10.3390/cells9122595.

[158] C. Peng *et al.*, "Intracranial Non-thermal Ablation Mediated by Transcranial Focused Ultrasound and Phase-Shift Nanoemulsions," *Ultrasound Med. Biol.*, vol. 45, no. 8, pp. 2104–2117, Aug. 2019, doi: 10.1016/j.ultrasmedbio.2019.04.010.

[159] C.-H. Fan *et al.*, "Submicron-Bubble-Enhanced Focused Ultrasound for Blood–Brain Barrier Disruption and Improved CNS Drug Delivery," *PLoS One*, vol. 9, no. 5, p. e96327, May 2014, [Online]. Available: https://doi.org/10.1371/journal.pone.0096327.

[160] M. Gyöngy, "Passive cavitation mapping for monitoring ultrasound therapy," *Thesis*, pp. 1–244, 2010, doi: http://ora.ouls.ox.ac.uk/objects/uuid%3Aaf6f3c5a-bec5-4378-a617-c89d2b16d95d.

[161] C. Coviello *et al.*, "Passive acoustic mapping utilizing optimal beamforming in ultrasound therapy monitoring," *J. Acoust. Soc. Am.*, vol. 137, no. 5, pp. 2573–2585, 2015, doi: 10.1121/1.4916694.

[162] J. Li, P. Stoica, and Z. Wang, "On robust Capon beamforming and diagonal loading," *ICASSP, IEEE Int. Conf. Acoust. Speech Signal Process. - Proc.*, vol. 5, no. 7, pp. 337–340, 2003, doi: 10.1109/TSP.2003.812831.

[163] W. J. FRY, "Intense ultrasound; a new tool for neurological research," *J. Ment. Sci.*, 1954, doi: 10.1192/bjp.100.418.85.

[164] E. S. Ebbini and C. A. Cain, "Multiple-Focus Ultrasound Phased-Array Pattern Synthesis: Optimal Driving-Signal Distributions for Hyperthermia," *IEEE Trans. Ultrason. Ferroelectr. Freq. Control*, vol. 36, no. 5, pp. 540–548, 1989, doi: 10.1109/58.31798.

[165] C. R. Merritt, "Doppler US: the basics.," *Radiographics*, vol. 11, no. 1, pp. 109–119, 1991, doi: 10.1148/radiographics.11.1.1996384.

[166] J. M. Fitzpatrick, J. B. West, and C. R. Maurer, "Predicting error in rigid-body point-based registration," *IEEE Trans. Med. Imaging*, vol. 17, no. 5, pp. 694–702, 1998, doi: 10.1109/42.736021.

[167] E. Lyka, "Passive Acoustic Mapping for Improved Detection and Localisation of Cavitation Activity," no. October, 2016.

[168] S. Norton, I. Won, A. Witten, A. Oren, and F. Funak, "Time-Exposure Acoustics for Imaging Underground Structures," Sep. 2003.

[169] J.Capon, "High-Resolution Frequency-Wavenumber Spectrum Analysis," *Proc. IEEE*, vol. 57, no. 8, pp. 1408–1418, 1969.

[170] C. Coviello *et al.*, “Passive acoustic mapping utilizing optimal beamforming in ultrasound therapy monitoring,” *J. Acoust. Soc. Am.*, vol. 137, no. 5, pp. 2573–2585, 2015, doi: 10.1121/1.4916694.

[171] R. F. Brem, “Radiofrequency Ablation of Breast Cancer: A Step Forward,” *Radiology*, vol. 289, no. 2, pp. 325–326, Aug. 2018, doi: 10.1148/radiol.2018181784.

[172] S. Stuver and D. Trichopoulos, “Cancer of the Liver and Biliary Tract,” in *Textbook of Cancer Epidemiology*, 2nd ed., New York: Oxford University Press, 2008.

[173] M. S. Grandhi, A. K. Kim, S. M. Ronnekleiv-Kelly, I. R. Kamel, M. A. Ghasebeh, and T. M. Pawlik, “Hepatocellular carcinoma: From diagnosis to treatment,” *Surg. Oncol.*, vol. 25, no. 2, pp. 74–85, 2016, doi: 10.1016/j.suronc.2016.03.002.

[174] S. D. Ryder and B. S. of Gastroenterology, “Guidelines for the diagnosis and treatment of hepatocellular carcinoma (HCC) in adults,” *Gut*, vol. 52 Suppl 3, no. Suppl 3, pp. iii1–iii8, May 2003, doi: 10.1136/gut.52.suppl_3.iii1.

[175] M. R. Middleton *et al.*, “The safety and feasibility of extracorporeal high-intensity focused ultrasound (HIFU) for the treatment of liver and kidney tumours in a Western population,” *Br. J. Cancer*, vol. 93, no. 8, pp. 890–895, 2005, doi: 10.1038/sj.bjc.6602803.

[176] L. Zhang *et al.*, “High-intensity focused ultrasound (HIFU): Effective and safe therapy for hepatocellular carcinoma adjacent to major hepatic veins,” *Eur. Radiol.*, vol. 19, no. 2, pp. 437–445, 2009, doi: 10.1007/s00330-008-1137-0.

[177] T. Leslie *et al.*, “High-intensity focused ultrasound treatment of liver tumours: post-treatment MRI correlates well with intra-operative estimates of treatment volume,” *Br. J. Radiol.*, vol. 85, no. 1018, pp. 1363–1370, Oct. 2012, doi: 10.1259/bjr/56737365.

[178] O. D. Kripfgans *et al.*, “Acceleration of ultrasound thermal therapy by patterned acoustic droplet vaporization,” *J. Acoust. Soc. Am.*, vol. 135, no. 1, pp. 537–544, Jan. 2014, doi: 10.1121/1.4828832.

[179] S. Hilgenfeldt, D. Lohse, and M. Zomack, “Sound scattering and localized heat deposition of pulse-driven microbubbles,” *J. Acoust. Soc. Am.*, vol. 107, no. 6, pp. 3530–3539, May 2000, doi: 10.1121/1.429438.

[180] A. Ignee, N. S. S. Atkinson, G. Schuessler, and C. F. Dietrich, “Ultrasound contrast agents,” *Endosc. ultrasound*, vol. 5, no. 6, pp. 355–362, 2016, doi: 10.4103/2303-9027.193594.

[181] M. Kudo, “Properties of Levovist BT - Contrast Harmonic Imaging in the Diagnosis and Treatment of Hepatic Tumors,” M. Kudo, Ed. Tokyo: Springer Japan, 2003, pp. 15–18.

[182] Y. Kaneko *et al.*, "Use of a microbubble agent to increase the effects of high intensity focused ultrasound on liver tissue," *Eur. Radiol.*, vol. 15, no. 7, pp. 1415–1420, 2005, doi: 10.1007/s00330-005-2663-7.

[183] A. Partanen, M. Tillander, P. S. Yarmolenko, B. J. Wood, M. R. Dreher, and M. O. Köhler, "Reduction of peak acoustic pressure and shaping of heated region by use of multifoci sonications in MR-guided high-intensity focused ultrasound mediated mild hyperthermia," *Med. Phys.*, vol. 40, no. 1, pp. 1–13, 2013, doi: 10.1118/1.4769116.

[184] M. R. Dreher, M. O. Köhler, A. Partanen, B. J. Wood, M. Tillander, and P. S. Yarmolenko, "Reduction of peak acoustic pressure and shaping of heated region by use of multifoci sonications in MR-guided high-intensity focused ultrasound mediated mild hyperthermia," *Med. Phys.*, vol. 40, no. 1, p. 013301, 2012, doi: 10.1118/1.4769116.

[185] V. Chaplin and C. F. Caskey, "Multi-focal HIFU reduces cavitation in mild-hyperthermia," *J. Ther. Ultrasound*, vol. 5, no. 1, pp. 1–14, 2017, doi: 10.1186/s40349-017-0089-8.

[186] K. Takegami, Y. Kaneko, T. Watanabe, T. Maruyama, Y. Matsumoto, and H. Nagawa, "Polyacrylamide gel containing egg white as new model for irradiation experiments using focused ultrasound," *Ultrasound Med. Biol.*, vol. 30, no. 10, pp. 1419–1422, 2004, doi: 10.1016/j.ultrasmedbio.2004.07.016.

[187] V. Chaplin, M. A. Phipps, and C. F. Caskey, "A random phased-array for MR-guided transcranial ultrasound neuromodulation in non-human primates Authors :," *Phys. Med. Biol.*, vol. 63, 2018, [Online]. Available: https://doi.org/10.1088/1361-6560/aabeff.

[188] C. Mougenot, M. O. Köhler, J. Enholm, B. Quesson, and C. Moonen, "Quantification of near-field heating during volumetric MR-HIFU ablation," *Med. Phys.*, vol. 38, no. 1, pp. 272–282, 2011, doi: 10.1118/1.3518083.

[189] J. C. Hindman, "Proton Resonance Shift of Water in the Gas and Liquid States," *J. Chem. Phys.*, vol. 44, no. 12, pp. 4582–4592, 2005, doi: 10.1063/1.1726676.

[190] M. A. Herráez, D. R. Burton, M. J. Lalor, and M. A. Gdeisat, "Fast two-dimensional phase-unwrapping algorithm based on sorting by reliability following a noncontinuous path," *Appl. Opt.*, vol. 41, no. 35, pp. 7437–7444, 2002, doi: 10.1364/AO.41.007437.

[191] L.-Y. Zhao, J.-Z. Zou, Z.-G. Chen, S. Liu, J. Jiao, and F. Wu, "Acoustic Cavitation Enhances Focused Ultrasound Ablation with Phase-Shift Inorganic Perfluorohexane Nanoemulsions: An In Vitro Study Using a Clinical Device," *Biomed Res. Int.*, vol. 2016, p. 7936902, 2016, doi: 10.1155/2016/7936902.

[192] K. Mahoney, T. Fjield, N. McDannold, G. Clement, and K. Hynynen, “Comparison of modelled and observed in vivo temperature elevations induced by focused ultrasound: Implications for treatment planning,” *Phys. Med. Biol.*, vol. 46, no. 7, pp. 1785–1798, 2001, doi: 10.1088/0031-9155/46/7/304.

[193] D. Li, G. Shen, H. Luo, J. Bai, and Y. Chen, “A study of heating duration and scanning path in focused ultrasound surgery,” *J. Med. Syst.*, vol. 35, no. 5, pp. 779–786, 2011, doi: 10.1007/s10916-010-9463-6.

[194] X. Wu and M. Sherar, “Theoretical evaluation of moderately focused spherical transducers and multi-focus acoustic lens/transducer systems for ultrasound thermal therapy,” *Phys. Med. Biol.*, vol. 47, no. 9, pp. 1603–1621, 2002, doi: 10.1088/0031-9155/47/9/313.

[195] T. Fan, Z. Liu, D. Zhang, and M. Tang, “Comparative study of lesions created by high-intensity focused ultrasound using sequential discrete and continuous scanning strategies,” *IEEE Trans. Biomed. Eng.*, vol. 60, no. 3, pp. 763–769, 2013, doi: 10.1109/TBME.2011.2167719.

[196] M. E. Poorman *et al.*, “Open-source, small-animal magnetic resonance-guided focused ultrasound system,” *J. Ther. Ultrasound*, vol. 4, no. 1, pp. 1–16, 2016, doi: 10.1186/s40349-016-0066-7.

[197] M. J. Voogt *et al.*, “Volumetric feedback ablation of uterine fibroids using magnetic resonance-guided high intensity focused ultrasound therapy,” *Eur. Radiol.*, vol. 22, no. 2, pp. 411–417, 2012, doi: 10.1007/s00330-011-2262-8.

[198] A. J. Fenoy and R. K. J. Simpson, “Risks of common complications in deep brain stimulation surgery: management and avoidance.,” *J. Neurosurg.*, vol. 120, no. 1, pp. 132–139, Jan. 2014, doi: 10.3171/2013.10.JNS131225.

[199] D. L. Miller, “Overview of experimental studies of biological effects of medical ultrasound caused by gas body activation and inertial cavitation,” *Progress in Biophysics and Molecular Biology*. 2007, doi: 10.1016/j.pbiomolbio.2006.07.027.

[200] R. D. Airan *et al.*, “Noninvasive Targeted Transcranial Neuromodulation via Focused Ultrasound Gated Drug Release from Nanoemulsions,” *Nano Lett.*, vol. 17, no. 2, pp. 652–659, 2017, doi: 10.1021/acs.nanolett.6b03517.

[201] H. A. Kamimura *et al.*, “Feedback control of microbubble cavitation for ultrasound-mediated blood-brain barrier disruption in non-human primates under magnetic resonance guidance.,” *J. Cereb. blood flow Metab. Off. J. Int. Soc. Cereb. Blood Flow Metab.*, vol. 39, no. 7, pp. 1191–1203, Jul. 2019, doi: 10.1177/0271678X17753514.

[202] A. J. Batts, R. Ji, A. R. Kline-Schoder, R. L. Noel, and E. E. Konofagou, “Transcranial Theranostic Ultrasound for Pre-Planning and Blood-Brain Barrier Opening: A Feasibility Study Using an Imaging Phased Array In Vitro and In Vivo,” *IEEE Trans. Biomed. Eng.*, p. 1, 2021, doi: 10.1109/TBME.2021.3120919.

[203] B. Mead, P. Mastorakos, J. S. Suk, J. Song, J. Hanes, and R. Price, “Localized delivery of non-viral gene-bearing nanoparticles into the rat brain following focused ultrasound-mediated BBB opening,” *J. Ther. Ultrasound*, 2015, doi: 10.1186/2050-5736-3-s1-p29.

[204] J. O. Szablowski, A. Lee-Gosselin, B. Lue, D. Malounda, and M. G. Shapiro, “Acoustically targeted chemogenetics for the non-invasive control of neural circuits,” *Nat. Biomed. Eng.*, 2018, doi: 10.1038/s41551-018-0258-2.

[205] C. Demené *et al.*, “Spatiotemporal Clutter Filtering of Ultrafast Ultrasound Data Highly Increases Doppler and fUltrasound Sensitivity,” *IEEE Trans. Med. Imaging*, vol. 34, no. 11, pp. 2271–2285, 2015, doi: 10.1109/TMI.2015.2428634.

[206] J. Liu, J. Foiret, D. N. Stephens, O. Le Baron, and K. W. Ferrara, “Development of a spherically focused phased array transducer for ultrasonic image-guided hyperthermia,” *Phys. Med. Biol.*, vol. 61, no. 14, pp. 5275–5296, Jul. 2016, doi: 10.1088/0031-9155/61/14/5275.

[207] J. M. Fitzpatrick, “The role of registration in accurate surgical guidance,” *Proc. Inst. Mech. Eng. Part H J. Eng. Med.*, 2010, doi: 10.1243/09544119JEIM589.

[208] M. A. Borden, D. E. Kruse, C. F. Caskey, S. Zhao, P. A. Dayton, and K. W. Ferrara, “Influence of lipid shell physicochemical properties on ultrasound-induced microbubble destruction,” *IEEE Trans. Ultrason. Ferroelectr. Freq. Control*, 2005, doi: 10.1109/TUFFC.2005.1561668.

[209] K. Martin and D. Spinks, “Measurement of the speed of sound in ethanol/water mixtures,” *Ultrasound Med. Biol.*, vol. 27, no. 2, pp. 289–291, 2001, doi: 10.1016/S0301-5629(00)00331-8.

[210] G. Benedetto, R. M. Gavioso, P. A. G. Albo, S. Lago, D. M. Ripa, and R. Spagnolo, “Speed of sound in pure water at temperatures between 274 and 394 K and at pressures up to 90 MPa,” *Int. J. Thermophys.*, vol. 26, no. 6, pp. 1667–1680, 2005, doi: 10.1007/s10765-005-8587-2.

[211] H. Wang, E. Ebbini, and C. A. Cain, “Computationally Efficient Algorithms for Control of Ultrasound Phased-Array Hyperthermia Applicators Based on a Pseudoinverse Method,” *IEEE Trans. Ultrason. Ferroelectr. Freq. Control*, vol. 37, no. 3, pp. 274–277, 1990, doi: 10.1109/58.55318.

[212] A. Singh, A. G. Nyankima, M. A. Phipps, V. Chaplin, P. A. Dayton, and C. F. Caskey, “Improving the heating efficiency of high intensity focused ultrasound ablation through the use of phase change nanodroplets and multifocus sonication,” *Phys. Med. Biol.*, May 2020, doi: 10.1088/1361-6560/ab9559.

[213] M. Gerstenmayer, B. Fellah, R. Magnin, E. Selingue, and B. Larrat, “Acoustic Transmission Factor through the Rat Skull as a Function of Body Mass, Frequency and Position,” *Ultrasound Med. Biol.*, 2018, doi: 10.1016/j.ultrasmedbio.2018.06.005.

[214] P. C. Tsai, H. S. Gougheri, and M. Kiani, “Skull Impact on the Ultrasound Beam Profile of Transcranial Focused Ultrasound Stimulation,” 2019, doi: 10.1109/EMBC.2019.8857269.

[215] X. Kang *et al.*, “Stereoscopic augmented reality for laparoscopic surgery.,” *Surg. Endosc.*, vol. 28, no. 7, pp. 2227–2235, Jul. 2014, doi: 10.1007/s00464-014-3433-x.

[216] J. A. Collins *et al.*, “Improving Registration Robustness for Image-Guided Liver Surgery in a Novel Human-to-Phantom Data Framework.,” *IEEE Trans. Med. Imaging*, vol. 36, no. 7, pp. 1502–1510, Jul. 2017, doi: 10.1109/TMI.2017.2668842.

[217] V. Chaplin *et al.*, “On the accuracy of optically tracked transducers for image-guided transcranial ultrasound,” *Int. J. Comput. Assist. Radiol. Surg.*, vol. 14, no. 8, pp. 1317–1327, 2019, doi: 10.1007/s11548-019-01988-0.

[218] S. Y. Wu *et al.*, “Efficient blood-brain barrier opening in primates with neuronavigation-guided ultrasound and real-time acoustic mapping,” *Sci. Rep.*, 2018, doi: 10.1038/s41598-018-25904-9.

[219] Y.-S. Tung, F. Vlachos, J. A. Feshitan, M. A. Borden, and E. E. Konofagou, “The mechanism of interaction between focused ultrasound and microbubbles in blood-brain barrier opening in mice,” *J. Acoust. Soc. Am.*, vol. 130, no. 5, pp. 3059–3067, Nov. 2011, doi: 10.1121/1.3646905.

[220] Y. Yang, C. P. Pacia, D. Ye, Y. Yue, C. Y. Chien, and H. Chen, “Static magnetic fields dampen focused ultrasound- mediated blood-brain barrier opening,” *Radiology*, 2021, doi: 10.1148/radiol.2021204441.

[221] G. Samiotaki, F. Vlachos, Y. S. Tung, and E. E. Konofagou, “A quantitative pressure and microbubble-size dependence study of focused ultrasound-induced blood-brain barrier opening reversibility in vivo using MRI,” *Magn. Reson. Med.*, 2012, doi: 10.1002/mrm.23063.

[222] M. A. O’Reilly, A. Muller, and K. Hynynen, “Ultrasound insertion loss of rat parietal bone appears to be proportional to animal mass at submegahertz frequencies,” *Ultrasound Med. Biol.*, vol. 37, no. 11, pp. 1930–1937, Nov. 2011, doi: 10.1016/j.ultrasmedbio.2011.08.001.

[223] D. Goerzen *et al.*, “An MRI-Derived Neuroanatomical Atlas of the Fischer 344 Rat Brain,” *Sci. Rep.*, 2020, doi: 10.1038/s41598-020-63965-x.

[224] A. Badea, A. A. Ali-Sharief, and G. A. Johnson, “Morphometric analysis of the C57BL/6J mouse brain,” *Neuroimage*, 2007, doi: 10.1016/j.neuroimage.2007.05.046.

[225] H. A. S. Kamimura *et al.*, “Focused ultrasound neuromodulation of cortical and subcortical brain structures using 1.9 MHz,” *Med. Phys.*, 2016, doi: 10.1118/1.4963208.

[226] E. Mehić, J. M. Xu, C. J. Caler, N. K. Coulson, C. T. Moritz, and P. D. Mourad, “Increased anatomical specificity of neuromodulation via modulated focused ultrasound,” *PLoS One*, 2014, doi: 10.1371/journal.pone.0086939.

[227] M. Welniak-Kaminska *et al.*, “Volumes of brain structures in captive wild-type and laboratory rats: 7T magnetic resonance in vivo automatic atlas-based study,” *PLoS One*, vol. 14, no. 4, pp. 1–18, 2019, doi: 10.1371/journal.pone.0215348.

[228] N. Kovačević *et al.*, “A three-dimensional MRI atlas of the mouse brain with estimates of the average and variability,” *Cereb. Cortex*, 2005, doi: 10.1093/cercor/bhh165.

[229] A. AU - Bertolo *et al.*, “Whole-Brain 3D Activation and Functional Connectivity Mapping in Mice using Transcranial Functional Ultrasound Imaging,” *JoVE*, no. 168, p. e62267, 2021, doi: doi:10.3791/62267.

[230] K. Blaize *et al.*, “Functional ultrasound imaging of deep visual cortex in awake nonhuman primates,” *Proc. Natl. Acad. Sci.*, vol. 117, no. 25, pp. 14453 LP – 14463, Jun. 2020, doi: 10.1073/pnas.1916787117.

[231] X. Yang, F. Hyder, and R. G. Shulman, “Functional MRI BOLD signal coincides with electrical activity in the rat whisker barrels.,” *Magn. Reson. Med.*, vol. 38, no. 6, pp. 874–877, Dec. 1997, doi: 10.1002/mrm.1910380604.

[232] X. Yang, F. Hyder, and R. G. Shulman, “Activation of single whisker barrel in rat brain localized by functional magnetic resonance imaging,” *Proc. Natl. Acad. Sci. U. S. A.*, vol. 93, no. 1, pp. 475–478, Jan. 1996, doi: 10.1073/pnas.93.1.475.

[233] C. Spenger *et al.*, “Functional MRI at 4.7 tesla of the rat brain during electric stimulation of forepaw, hindpaw, or tail in single- and multislice experiments.,” *Exp. Neurol.*, vol. 166, no. 2, pp. 246–253, Dec. 2000, doi: 10.1006/exnr.2000.7524.

[234] S. D. Keilholz, A. C. Silva, M. Raman, H. Merkle, and A. P. Koretsky, “Functional MRI of the rodent somatosensory pathway using multislice echo planar imaging,” *Magn. Reson. Med.*, vol. 52, no. 1, pp. 89–

99, 2004, doi: 10.1002/mrm.20114.

[235] M. Burke, W. Schwindt, U. Ludwig, J. Hennig, and M. Hoehn, “Facilitation of electric forepaw stimulation-induced somatosensory activation in rats by additional acoustic stimulation: an fMRI investigation.,” *Magn. Reson. Med.*, vol. 44, no. 2, pp. 317–321, Aug. 2000, doi: 10.1002/1522-2594(200008)44:2<317::aid-mrm20>3.0.co;2-r.

[236] R. Weber, P. Ramos-Cabrer, D. Wiedermann, N. van Camp, and M. Hoehn, “A fully noninvasive and robust experimental protocol for longitudinal fMRI studies in the rat.,” *Neuroimage*, vol. 29, no. 4, pp. 1303–1310, Feb. 2006, doi: 10.1016/j.neuroimage.2005.08.028.

[237] Z. M. Liu, K. F. Schmidt, K. M. Sicard, and T. Q. Duong, “Imaging oxygen consumption in forepaw somatosensory stimulation in rats under isoflurane anesthesia.,” *Magn. Reson. Med.*, vol. 52, no. 2, pp. 277–285, Aug. 2004, doi: 10.1002/mrm.20148.

[238] F. Schlegel, A. Schroeter, and M. Rudin, “The hemodynamic response to somatosensory stimulation in mice depends on the anesthetic used: Implications on analysis of mouse fMRI data,” *Neuroimage*, vol. 116, pp. 40–49, 2015, doi: https://doi.org/10.1016/j.neuroimage.2015.05.013.

[239] S. Boussida, A. S. Traoré, and F. Durif, “Mapping of the brain hemodynamic responses to sensorimotor stimulation in a rodent model: A BOLD fMRI study,” *PLoS One*, vol. 12, no. 4, pp. 1–15, 2017, doi: 10.1371/journal.pone.0176512.

[240] N. Van Camp, M. Verhoye, and A. Van der Linden, “Stimulation of the rat somatosensory cortex at different frequencies and pulse widths,” *NMR Biomed.*, vol. 19, no. 1, pp. 10–17, 2006, doi: 10.1002/nbm.986.

[241] A. G. Goloshevsky, A. C. Silva, S. J. Dodd, and A. P. Koretsky, “BOLD fMRI and somatosensory evoked potentials are well correlated over a broad range of frequency content of somatosensory stimulation of the rat forepaw,” *Brain Res.*, vol. 1195, pp. 67–76, Feb. 2008, doi: 10.1016/j.brainres.2007.11.036.

[242] T. Kim, K. Masamoto, M. Fukuda, A. Vazquez, and S.-G. Kim, “Frequency-dependent neural activity, CBF, and BOLD fMRI to somatosensory stimuli in isoflurane-anesthetized rats,” *Neuroimage*, vol. 52, no. 1, pp. 224–233, Aug. 2010, doi: 10.1016/j.neuroimage.2010.03.064.

[243] M. L. Gyngell, C. Bock, B. Schmilz, M. Hoehn-Berlage, and K. A. Hossmann, “Variation of functional MRI signal in response to frequency of somatosensory stimulation in α-chloralose anesthetized rats,” *Magn. Reson. Med.*, vol. 36, no. 1, pp. 13–15, 1996, doi: 10.1002/mrm.1910360104.

[244] B. J. Edelman, G. D. Ielacqua, R. W. Chan, M. Asaad, M. Choy, and J. H. Lee, "High-sensitivity detection of optogenetically-induced neural activity with functional ultrasound imaging," *Neuroimage*, vol. 242, p. 118434, 2021, doi: https://doi.org/10.1016/j.neuroimage.2021.118434.

[245] G. Paxinos, "Preface," G. B. T.-T. R. N. S. (Fourth E. Paxinos, Ed. San Diego: Academic Press, 2015, p. xi.

[246] A. C. Silva and A. P. Koretsky, "Laminar specificity of functional MRI onset times during somatosensory stimulation in rat.," *Proc. Natl. Acad. Sci. U. S. A.*, vol. 99, no. 23, pp. 15182–15187, Nov. 2002, doi: 10.1073/pnas.222561899.

[247] C. Bock, H. Krep, G. Brinker, and M. Hoehn-Berlage, "Brainmapping of alpha-chloralose anesthetized rats with T2*-weighted imaging: distinction between the representation of the forepaw and hindpaw in the somatosensory cortex.," *NMR Biomed.*, vol. 11, no. 3, pp. 115–119, May 1998, doi: 10.1002/(sici)1099-1492(199805)11:3<115::aid-nbm526>3.0.co;2-k.

[248] K. Masamoto, T. Kim, M. Fukuda, P. Wang, and S. G. Kim, "Relationship between neural, vascular, and BOLD signals in isoflurane-anesthetized rat somatosensory cortex," *Cereb. Cortex*, vol. 17, no. 4, pp. 942–950, 2007, doi: 10.1093/cercor/bhl005.

[249] J. B. Mandeville, J. J. Marota, C. Ayata, M. A. Moskowitz, R. M. Weisskoff, and B. R. Rosen, "MRI measurement of the temporal evolution of relative CMRO(2) during rat forepaw stimulation.," *Magn. Reson. Med.*, vol. 42, no. 5, pp. 944–951, Nov. 1999, doi: 10.1002/(sici)1522-2594(199911)42:5<944::aid-mrm15>3.0.co;2-w.

[250] M. Grüne, F. Pillekamp, W. Schwindt, and M. Hoehn, "Gradient echo time dependence and quantitative parameter maps for somatosensory activation in rats at 7 T.," *Magn. Reson. Med.*, vol. 42, no. 1, pp. 118–126, Jul. 1999, doi: 10.1002/(sici)1522-2594(199907)42:1<118::aid-mrm16>3.0.co;2-t.

[251] E. Tiran *et al.*, "Transcranial Functional Ultrasound Imaging in Freely Moving Awake Mice and Anesthetized Young Rats without Contrast Agent," *Ultrasound Med. Biol.*, vol. 43, no. 8, pp. 1679–1689, Aug. 2017, doi: 10.1016/j.ultrasmedbio.2017.03.011.